

# CHALMERS



## Ringhals Diagnostics and Monitoring, Annual Research Report 2020-21

I. PÁZSIT  
L. A. TORRES  
C. MONTALVO  
L. NAGY  
G. KLUJBER  
M. SZIEBERTH  
T. MISAWA  
Y. KITAMURA  
V. DYKIN  
H. NYLÉN

*Nuclear Engineering Group*

Division of Subatomic, High Energy and Plasma Physics

CHALMERS UNIVERSITY OF TECHNOLOGY

Gothenburg, Sweden, 2021

CTH-NT-344/RR-24 June 2021



# Ringhals Diagnostics and Monitoring, Annual Research Report 2020-2021

I. Pázsit, L. A. Torres, C. Montalvo, L. Nagy, G. Klujber,  
M. Szieberth, T. Misawa, Y. Kitamura, V. Dykin, H. Nylén





# Ringhals Diagnostics and Monitoring, Annual Research Report 2020-2021

I. Pázsit, L. A. Torres, C. Montalvo, L. Nagy, G. Klujber,  
M. Szieberth, T. Misawa, Y. Kitamura, V. Dykin, H. Nylén

Nuclear Engineering Group  
Division of Subatomic, High Energy and Plasma Physics  
Chalmers University of Technology  
SE-412 96 Göteborg, Sweden

## Abstract

This report gives an account of the work performed by the Division of Subatomic, High Energy and Plasma Physics (formerly, Division of Nuclear Engineering), Chalmers, in the frame of a research collaboration with Ringhals, Vattenfall AB, contract No. 4501737229-003. The contract constitutes a one-year co-operative research work concerning diagnostics and monitoring of the BWR and PWR units. The work in the contract has been performed between 1 July 2020 and 30 June 2021. During this period, we worked with four main items as follows:

1. Further analysis of the vibrations of thimble tubes with axially dependent in-core measurements in various radial positions;
2. Evaluation of new ex-core measurements for beam mode and tilting mode vibrations in R3;
3. Experimental work and simulations in support of the use of fission chambers in the current mode for reactivity measurements, as an alternative of pulse counting methods;
4. Further development of a new method to determine the axial velocity profile of the void in the core of a BWR by using four permanent in-core LPRMs and a TIP detector.

The work was performed by Imre Pázsit (project co-ordinator), Luis Alejandro Torres and Cristina Montalvo (research collaborators from UPM, Madrid), Lajos Nagy (double degree PhD student jointly with BME Budapest), Gergely Klujber and Máté Szieberth (research collaborators from BME), Tsuyoshi Misawa and Yasunori Kitamura (research collaborators from KURNS, Kyoto, Japan), Victor Dykin and Henrik Nylén, the contact person at Ringhals.

## CONTENTS

<b>1</b>	<b>INTRODUCTION</b>	<b>1</b>
<b>2</b>	<b>FURTHER ANALYSIS OF THE VIBRATIONS OF THIMBLE TUBES WITH AXIALLY DEPENDENT IN-CORE MEASUREMENTS IN VARIOUS RADIAL POSITIONS</b>	<b>2</b>
2.1	The layout and details of the measurements . . . . .	5
2.2	Results of the analysis of Measurement 1 . . . . .	7
2.2.1	Power spectra . . . . .	7
2.2.2	Coherences and phases between detector pairs at the same axial elevation . . . . .	11
2.3	Summary . . . . .	16
<b>3</b>	<b>EVALUATION OF NEW EX-CORE MEASUREMENTS FOR BEAM MODE AND TILTING MODE VIBRATIONS IN R3</b>	<b>17</b>
3.1	Introduction and background . . . . .	17
3.2	Details of the measurements in R3 . . . . .	19
3.3	Analysis of the measurements made on 2020-10-29 (Measurement 1) .	19
3.3.1	Individual spectra of all detectors . . . . .	19
3.3.2	Results of the mode separation . . . . .	21
3.3.3	Phase and coherence relationships between the upper and lower detectors . . . . .	23
3.4	Analysis of the measurements made on 2021-04-01 (Measurement 2) .	26
3.4.1	Individual spectra of all detectors . . . . .	26
3.4.2	Results of the mode separation . . . . .	27
3.4.3	Phase and coherence relationships between the upper and lower detectors . . . . .	29
3.5	Trend analysis within the cycle . . . . .	29
3.6	Long term trend analysis . . . . .	31
<b>4</b>	<b>EXPERIMENTAL WORK AND SIMULATIONS IN SUPPORT OF THE USE OF FISSION CHAMBERS IN THE CURRENT</b>	

<b>MODE FOR REACTIVITY MEASUREMENTS, AS AN ALTERNATIVE OF PULSE COUNTING METHODS</b>	<b>35</b>
4.1 Introduction . . . . .	35
4.2 Theory . . . . .	36
4.2.1 Traditional theory . . . . .	36
4.2.2 New theory . . . . .	36
4.3 Simulations . . . . .	38
4.4 Experiments . . . . .	40
4.4.1 Core and measurement configurations . . . . .	40
4.4.2 Instrumentation . . . . .	42
4.4.3 Data analysis . . . . .	44
4.5 Conclusions and further plans . . . . .	50
<b>5 FURTHER DEVELOPMENT OF A NEW METHOD TO DETERMINE THE AXIAL VELOCITY PROFILE OF THE VOID IN THE CORE OF A BWR BY USING FOUR PERMANENT IN-CORE LPRMS AND A TIP DETECTOR</b>	<b>52</b>
5.1 Introduction . . . . .	52
5.2 Summary of previous work . . . . .	54
5.2.1 Qualitative flow profiles . . . . .	54
5.2.2 Possible analytical forms . . . . .	54
5.2.3 The unfolding procedure . . . . .	57
5.3 Improvements and further developments . . . . .	57
5.3.1 Void velocity vs perturbation velocity . . . . .	57
5.3.2 Accuracy and consistency of the determination of the transit times . . . . .	58
5.3.3 Uncertainty investigation . . . . .	63
5.3.4 Test with velocity profiles obtained from RAMONA . . . . .	64
5.4 Conclusions . . . . .	67
<b>6 PROPOSAL FOR 2021-22</b>	<b>68</b>
<b>7 ACKNOWLEDGEMENT</b>	<b>69</b>



## 1. INTRODUCTION

This report gives an account of the work performed by the Nuclear Engineering Group of the Division of Subatomic, High Energy and Plasma Physics (formerly, Division of Nuclear Engineering), Chalmers, in the frame of a research collaboration with Ringhals, Vattenfall AB, contract No. 4501737229-003. The contract constitutes a one-year co-operative research work concerning diagnostics and monitoring of the BWR and PWR units. The work in the contract has been performed between 1 July 2020 and 30 June 2021. During this period, we worked with four main items as follows:

1. Further analysis of the vibrations of thimble tubes with axially dependent in-core measurements in various radial positions;
2. Evaluation of new ex-core measurements for beam mode and tilting mode vibrations in R3;
3. Experimental work and simulations in support of the use of fission chambers in the current mode for reactivity measurements, as an alternative of pulse counting methods;
4. Further development of a new method to determine the axial velocity profile of the void in the core of a BWR by using four permanent in-core LPRMs and a TIP detector.

This work was performed by Imre Pázsit (project co-ordinator in Chalmers), Luis Alejandro Torres and Cristina Montalvo (research collaborators from UPM, Madrid), Lajos Nagy (double degree PhD student jointly with BME Budapest), Gergely Klujber and Máté Szieberth (research collaborators from BME), Tsuyoshi Misawa and Yasunori Kitamura (research collaborators from KURNS, Kyoto, Japan), Victor Dykin, and Henrik Nylén, the contact person at Ringhals.

## 2. FURTHER ANALYSIS OF THE VIBRATIONS OF THIMBLE TUBES WITH AXIALLY DEPENDENT IN-CORE MEASUREMENTS IN VARIOUS RADIAL POSITIONS

The phenomenon of thimble tube vibrations, and the possible consequences of these vibrations and impacting of the thimble tubes on the instrument tubes have long been known. The problem got a wider attention first within the nuclear program of EDF in the late 1980's, when their 1300 MWe PWR plants were introduced [1, 2]. Several cases of thimble tube vibrations and their effects were observed, including fatigue and wear of both the thimble tube and the instrument tube, and in some cases leaks in the thimble tube. This resulted in the fact that EDF launched a dedicated program for the surveillance and monitoring of thimble tube vibrations and impacting [3].

The investigation of possible thimble tube vibrations was taken up withing the Chalmers-Ringhals collaboration in Stage 2018 [4], when also a survey of the literature on the previous experiences was performed. As it was described in Ref. [4], the diagnostic problem is rather complicated. The characteristics of these vibrations is very varied, as they are functions of a number of different factors, such as the fuel assembly type, the contact surface between the fuel assembly bottom nozzle and the thimble tubes, and not the least the radial position in the core.

According to the EDF experience, there are two possibilities to detect and quantify thimble tube vibrations, and possibly detect impacting. The most effective method is to use ex-core accelerometers, attached to the guide tubes below the bottom of the pressure vessel. These accelerometers can detect both the vibrations (from the periodic component of the signal) as well as impacting (from the spikes caused by the impacting). Unfortunately, this possibility is not available in Ringhals, due to the absence of such accelerometer signals, hence the other, less effective method of analysing the in-core neutron noise measurements has to be used.

From the neutron noise diagnostic point of view, detection of thimble tube vibrations shows some resemblance to the detector instrument tube vibrations and impacting in BWRs [5]. BWR instrument tube vibrations can also lead to impacting against the wall(s) of some of the surrounding four fuel boxes. In some cases heavy impacting led to damage of the LPRM detectors in the instrument tube, and even to holes in the fuel box walls, leading to undesired cross-flow. Such instrument tube vibrations and impacting have occurred also in Swedish BRWs [5], and the problem was investigated in several previous Stages, i.e from Stage 8 through Stage 12 [6, 7, 8, 9, 10].

However, detection of BWR instrument tube vibrations is significantly simpler than that of the thimble tube vibrations. In the BWR case, each and every one of the 36 instrument tubes contains not only one, but four LPRM detectors. Hence, in every case of a vibrating instrument tube, the four detectors of the detector string in that tube will all exhibit a peak at the vibration frequency, due to the movement of the detectors in a flux gradient. The frequency of the detector string

vibrations is also known, it is around 2-3 Hz, and it is easily observed and pointed out in the otherwise smooth frequency dependence of the in-core BWR neutron noise spectrum. A final advantage is that one can take the cross-spectrum between two detectors in the same detector string, sitting at different axial positions. In a normal (vibration-free) case, the phase depends linearly on the frequency, which is a characteristic of the “propagation noise” [11], due to the transit of the void between the two detectors. The vibrations, which are in-phase and hence have zero phase delay between two detectors in the same string, will distort this nice linear phase, bringing it closer to zero around the vibration frequency. This gives immediately a hint on the existence of vibrations, but even on their severity, through the severity of the distortion.

In contrast, in the case of the Swedish PWRs (like in all Westinghouse-type PWRs), there are no fixed in-core detectors installed. One can make short measurements with a maximum of 5 movable detectors at a time, and these have to be in different guide tubes, i.e. in different radial core positions. This means that by relying on the same method as with BWR instrument tube vibrations, i.e. detecting thimble tube vibrations from the noise signals induced by the vibrations of the detectors themselves, only a very small fraction of all thimble tubes can be diagnosed. A further complication is that auto power spectra (APDS) of the PWR in-core movable detectors contains a considerably larger number of peaks, not to mention that the eigenfrequency of the thimble tubes is not known. The axial dependence of the amplitude of the possible thimble tube vibrations is not known either. Last, but not least, the possibility of cross-correlating detector signals in the same instrument tube is also missing.

What concerns the vibrations of thimble tubes that do not contain movable detectors, the only possibility of detecting these from in-core measurements performed in other thimble tubes, is to utilize the noise induced by the vibrations of the detector-free thimble tubes. The principle of the detection in this case is different from that of the case of a vibrating thimble tube containing a detector. The principle in this case is that a thimble tube can be interpreted as an absorber, hence its vibrations would lead to a neutron noise with the characteristics of a (laterally) vibrating absorber. In the neighbourhood of such a vibrating absorber, two neutron detectors at opposite sides of the vibrating object would show out-of-phase behaviour, or at least significant deviations from the in-phase behaviour (which is the characteristics of an absorber of variable strength, such as a channel-type two-phase flow instability).

Nevertheless, this method has substantial weaknesses. First, the amplitude of the induced noise will be rather small. Compared to a control assembly containing large volumes of strong neutron absorbers, the thimble tube contains small amounts of weakly absorbing material. Second, the range of the local component of the vibration induced noise (which is the reason of the opposite phase behaviour between two detectors at opposite sides of the vibrating thimble tube) is short. In practice this means that using the maximum of 5 detectors, the possible vibrations of detector-free thimble tubes can only be detected in between the 4 pairs of closest instrumented tubes. Third, the possible vibrations of individual fuel elements and/or control assemblies, will also induce neutron noise, which might exceed the

noise induced by the vibrating thimble tube. Finally, if any of the two instrumented thimble tubes, used to identify the vibrations of non-instrumented thimble tubes, should also vibrate during the measurement, then the noise induced by their own vibration will suppress completely the weak noise induced by the vibrations of the non-instrumented thimble tube.

It is thus seen that the problem to be solved contains a number of unknown parameters and lacking necessary information, with only a few measured data. The only way of having some insight is to progress in a heuristic trial-and-error manner. Therefore we expect that this phenomenon will be investigated during several further Stages, possibly with various analysis methods.

Our previous experience with in-core PWR neutron noise measurement stems from some of the earlier stages, such as Stages 4, 12 and 13 [12, 10, 13], when in-core measurements were performed in five radial positions simultaneously, at four or six different axial positions. However, the purpose of those measurement was different. At that time, the interest was not on the investigation of thimble tube vibrations. Rather, based on the literature and similar studies in the US, we assumed that all measured in-core noise is due to fuel assembly vibrations. Hence in those measurements we attempted to identify the axial vibration modes of the individual fuel assemblies, and also to assist the analysis of the ex-core measurements for the diagnostics of shell mode vibrations. It was assumed that the individual peaks in the in-core detector signals were due to the vibrations corresponding to the various bending modes of the fuel assemblies. In the analysis of those measurements, only the APDSs of the individual detectors were investigated.

The first attempt to diagnose thimble tube vibrations was made during Stage 2018 [4]. In that year, no new in-core measurements were possible to make, hence we decided to use the in-core measurements analysed in Stage 12 for fuel assembly vibrations, taken in 2008, in cycle 25 in R4. Since the peak structure of those measurements was already analysed in Stage 12 and was found rather difficult to interpret, we decided to analyse the hypothetical scenario that none of the instrumented thimble tubes would vibrate, hence a peak of the coherence and out-of-phase between radially close detector pairs at the same axial elevation would indicate the vibration of a thimble tube in between the two radial positions. No clear-cut decision was possible to be drawn from the analysis. A slight possibility of thimble tube vibrations was seen between one of the detectors and other three detectors, around 2 - 6 Hz. An even slighter possibility was seen for vibrations centered around 20 Hz, although too broad in frequency (15 - 25 Hz) to correspond to vibrations. The fact that one of the detectors in a group of four did not share the out-of-phase behaviour with the fifth detector was interpreted as a possibility that particular instrumented thimble tube could have vibrated.

In the present Stage two sets of new measurements were made in R3 which we could analyse. However, for reasons described later on in this Chapter, only Measurement 1 was evaluated. Since these data are new, we investigated both the peaks in the auto-spectra for each detector in all six axial positions, as well as the coherence and phase between two detectors at the same axial position. The layout of the measurements, and the analysis results will be discussed in the following.



## 2.1 The layout and details of the measurements

The layout of the measurement, i.e. the radial and axial detector positions used in the measurements are shown in Figs. 2.1 and 2.2, respectively. Four movable in-core detectors were used, labeled from A to D. The detector notations with their corresponding core positions are shown in Table 2.1.

In-core detector	Core position
A	N12
B	N08
C	N10
D	L04

Table 2.1: The detector designations in the instrumented thimble tubes and their core positions.

As it is seen on the core map of Fig. 2.1, and also from Table 2.1, the in-core detectors are aligned nearly along a line (in column *N* of the core, except detector D). Originally, detector D was intended to be placed into the core position N05, but this position shares the guide tube switch with position N12, which is already used in the measurement, this is why position L04 was chosen for detector D. Due to the placing of the detectors, in the coherence and phase analysis, one expects information on the possible vibrations of thimble tubes in column *N* or its neighbourhood.

Regarding the measurement system, a Westinghouse digital Flux Mapping System was installed in R3 during the outage 2016. The thermal neutron sensitivity of the four in-core flux detectors (fission chambers) ranges up to  $10^{14}$  nv, although noticeable variation of the sensitivity amongst the detectors can be observed.

Two measurement series were made, both on 1 December 2020. Each series was taken in one sequence, without interrupting the data logging, such that all four in-core detectors were moved simultaneously between the measurement positions. In the long measurement record, the change of the axial position of the detectors, and hence the end of a measurement in a given axial position, can be recognised by a spike in the recorded signal time series, and the different sections of the measurement have to be separated manually. In the first measurement series, six 30-minutes measurements were made at six different axial positions. The first measurement was made in the uppermost position (30 cm below the top of the core), and then the detectors were lowered by 60 cm to the next position in five consecutive steps, the last measurement being taken 30 cm above the bottom of the core. In the second series, a one-minute measurement was made in 21 subsequent axial positions, separated by 18 cm from each other. The first 1-minute measurement was taken in level with the core top, and the last at the level of the core bottom. The axial positions of the detectors in the two measurement series are shown in Fig. 2.2.

In this report only Measurement 1 is evaluated. The reason is that Measurement 2 was originally conceived in order to analyse it with wavelet transform methods, in order to follow the evolution of the characteristic peaks in time as the detectors are continuously withdrawn from the top of the core, hence revealing at which positions

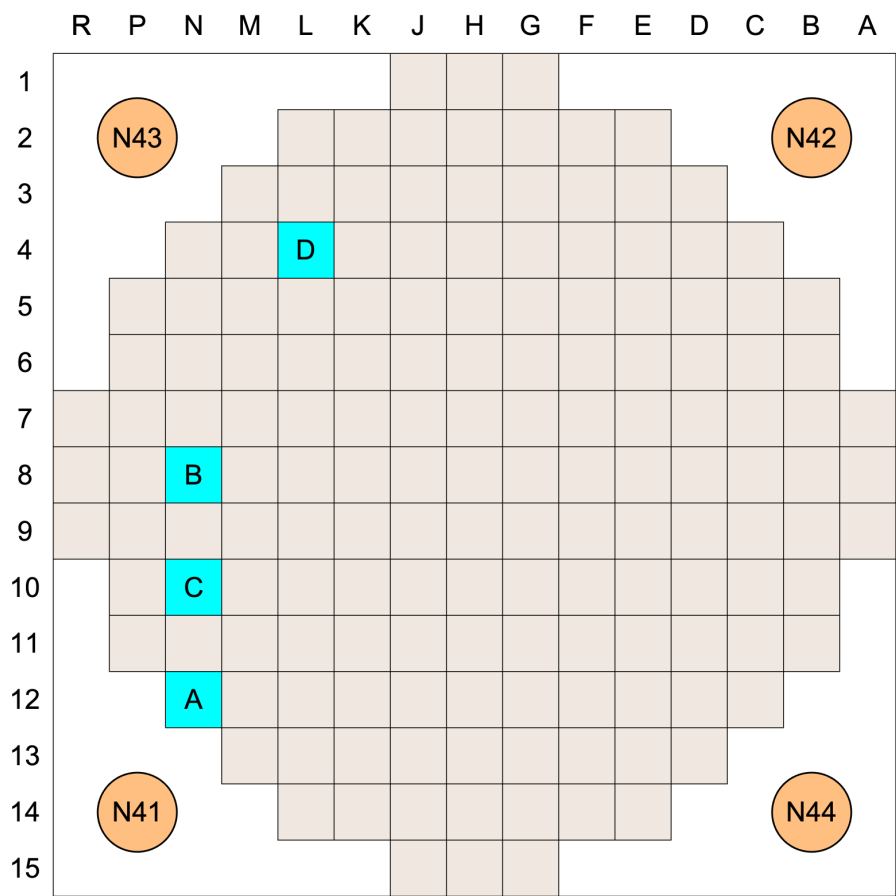


Figure 2.1: The radial positions of the four in-core detectors.

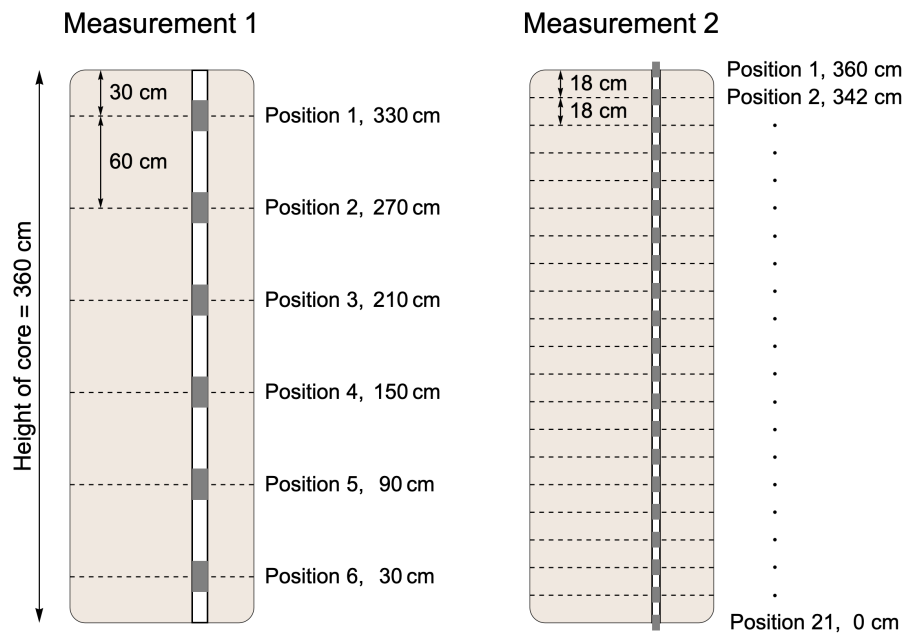


Figure 2.2: The axial positions of the measurement points in the two measurements.

characteristic frequencies occur, and which frequencies are persistent (not depending on the measurement position). This is equivalent with a short-time Fourier transform with a sliding time window.

However, the experience from the evaluation of Measurement 1 showed that the spectral analysis, even with significantly longer measurement times (20 minutes as opposed to 1 minutes per position) gives a limited information on the vibrations, and in particular on the possible impacting. As elaborated in the foregoing, a more promising method is to evaluate the measurement with *wavelet filtering* methods [14, 15, 16]. This means to perform a filtering on the wavelet transformed time series (in analogy with the frequency filtering of Fourier-transformed signals) and then performing an inverse wavelet transform. With this method, spikes in the original time series, which can be an indicator of impacting, can be detected. We have used this method in the past for detecting detector tube impacting in BWRs, including R1, but the software tools have been lost and have to be built up from scratch. The methodology and software framework will be built up again, and such an analysis is planned for the next Stage.

## 2.2 Results of the analysis of Measurement 1

### 2.2.1 Power spectra

As discussed in the previous section, the power spectra (APSDs) are mostly useful to detect and interpret vibrations of the instrumented thimble tubes themselves, and the interpretation of the spectra will be made with this point of view in mind. The APSDs of Measurement series 1 are displayed in two different layouts. In Figs 2.3 and 2.4, the APSDs of all four detectors are shown, taken at the three upper and the three lower axial positions, respectively. In Fig. 2.5 the spectra of the four detectors are shown in separate plots, in each plot the 6 spectra are shown for the six axial positions in which the measurements were made.

These spectra show both similarities and differences compared to those in the measurements taken in R4 in 2008 [10]. This is not surprising, given that the present measurements were made in a different core and with a different measurement equipment. In the 2008 measurements, in practically all measurements, there was a relatively broad peak at around 6-7 Hz, which was most likely the superposition of two peaks with close frequencies (6 and 7 Hz, respectively). For some of the cases it was possible to separate this broad peak to two narrower peaks. In the current measurements, there is one dominating sharp peak around 8 Hz, which is partly higher than the broad one in the R4 measurements in 2008, and the peak is significantly narrower. This frequency is actually the same as the one seen in the APSD of the ex-core detectors, and which in our previous work was identified as the effect of the individual fuel assembly vibrations, induced by the beam mode of the core-barrel motion. This peak is present in all detectors and at all axial levels.

In addition, there are some other peaks, which only occur in certain detectors and/or at certain axial elevations. In the two lowermost positions, nearly all detectors show an additional narrow peak at around 5 - 6 Hz. Further, detector D shows a broad peak with varying width in the upper levels. This is a frequency range, where

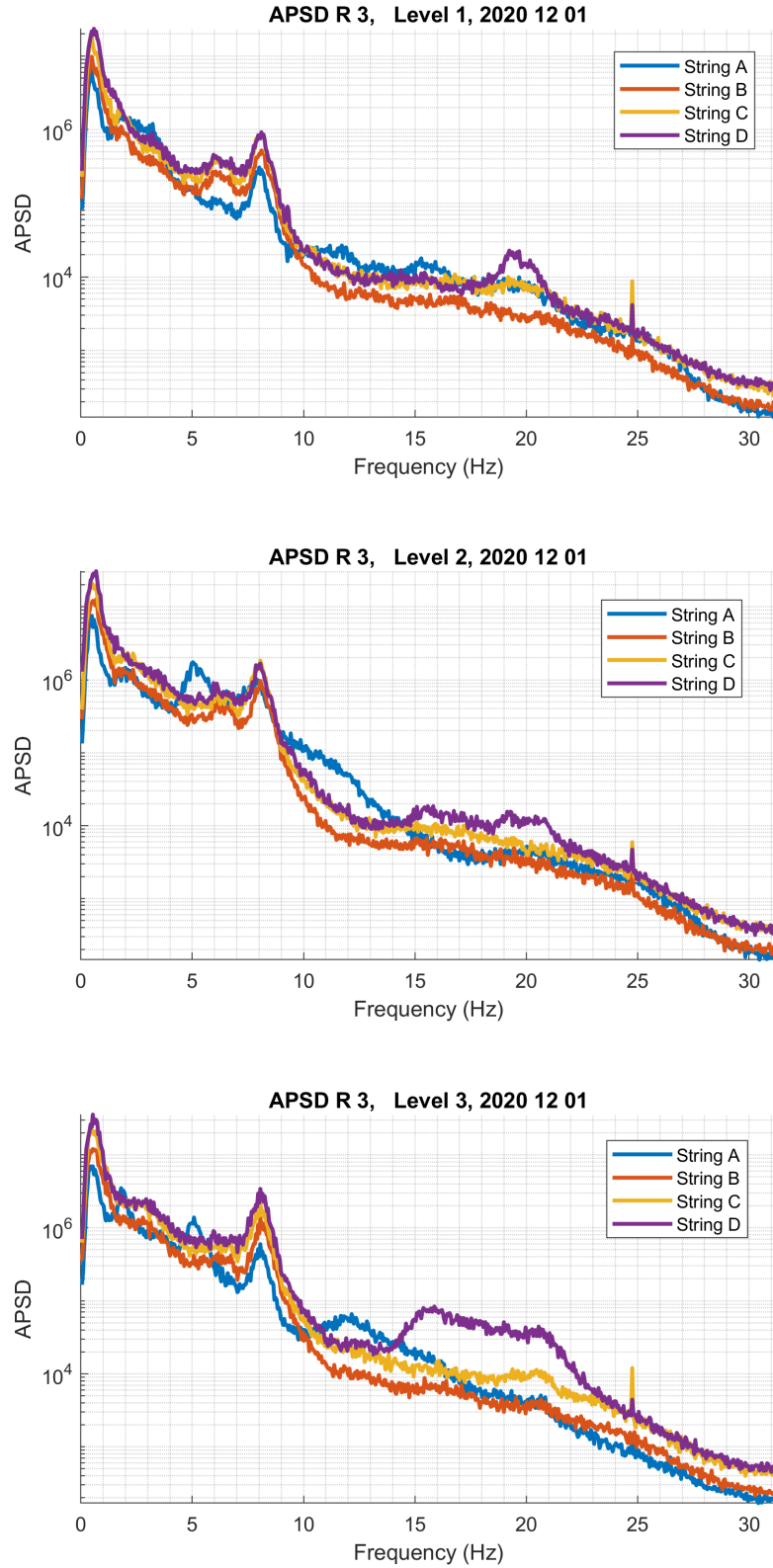


Figure 2.3: APSDs of the four detectors A, B, C and D at the three highest axial positions (levels 1 - 3).

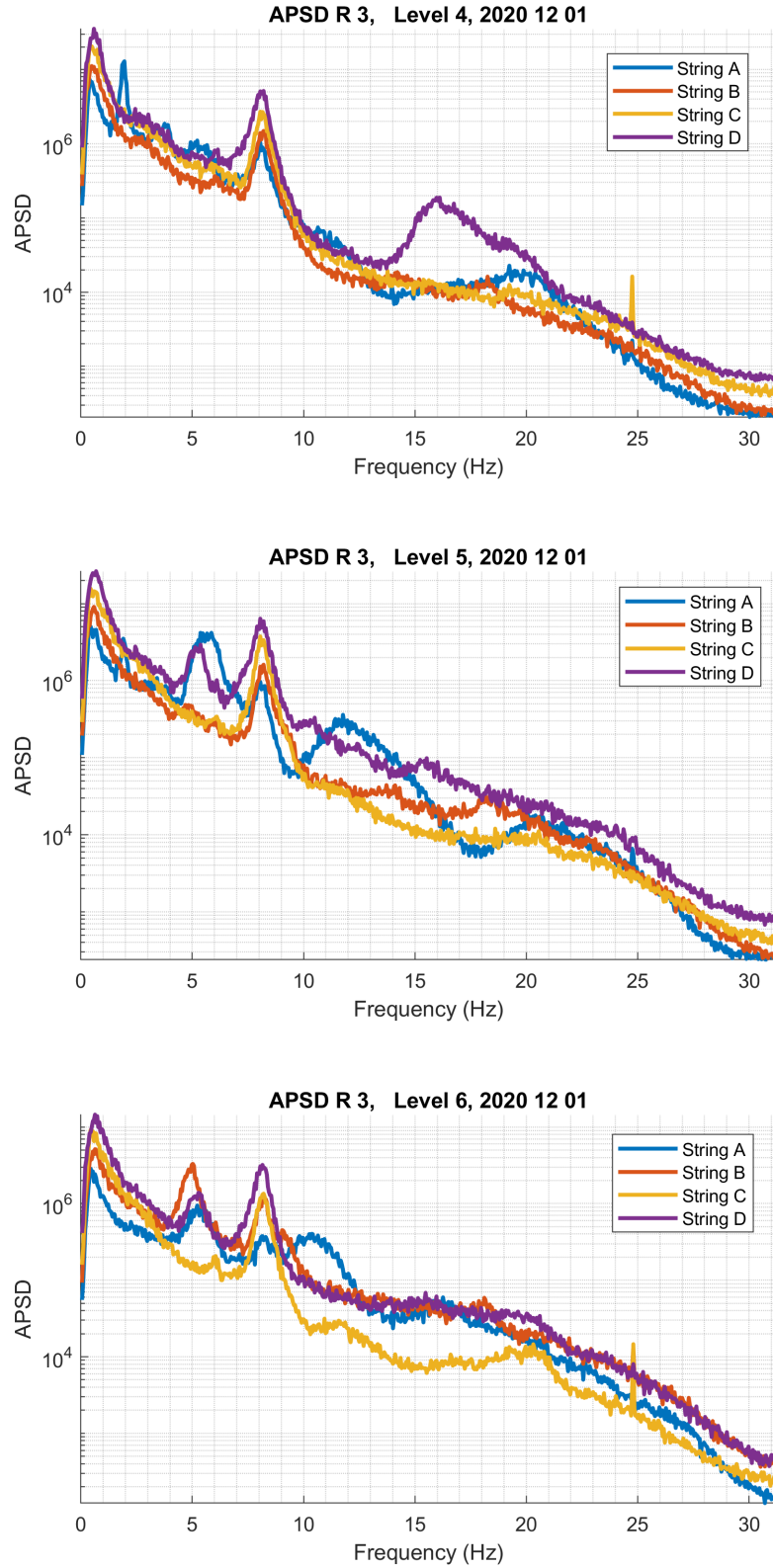


Figure 2.4: APSDs of the four detectors A, B, C and D at the three lowest axial positions (levels 4 - 6).

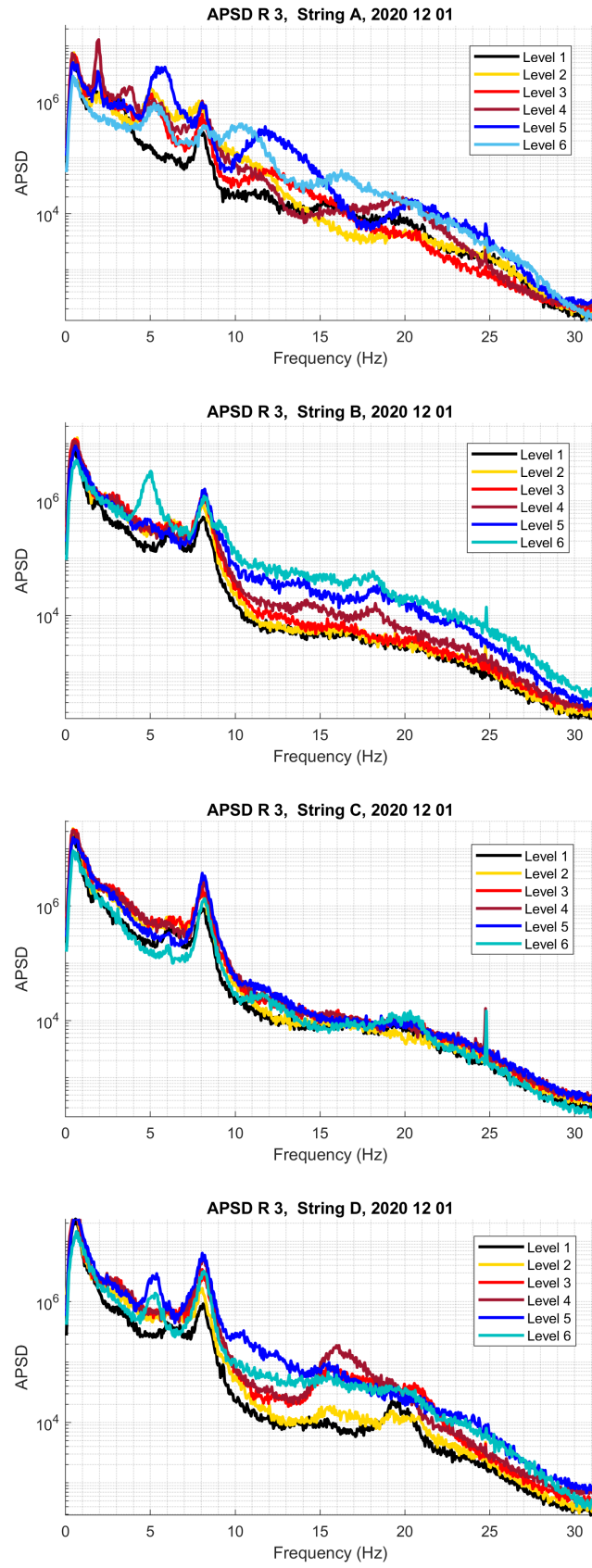


Figure 2.5: Individual APSDs of the four detectors at all 6 axial positions in one plot

in Stage 2018 opposite phase behaviour was found between detector E and the other four detectors, and hence a possible thimble tube vibration of a non-instrumented thimble tube (or that of a fuel assembly) was suspected. The interesting point is that, as the core map in Fig. 3.1 in [4] shows, similarly to detector D in the present measurements, detector E in those measurements lay somewhat separated from the rest of the detectors. Finally, string A shows peaks at most levels in the range 10 -14 Hz, with varying peak frequency and breadth.

The final conclusion is that thimble tube vibrations may be suspected of the thimble tube of detector D, at 15-20 Hz and possibly at 6 Hz, and to a lesser degree at 6 Hz in detectors A and D. A 6 Hz peak is also seen for detector B at level 6, which is close to the contact point between the fuel assembly bottom nozzle and the thimble tube, where previous wear has been observed. However, it has to be added that these frequencies correspond, or are close to, the beam mode and shell mode vibrations of the core barrel, hence it cannot be taken as granted that the mentioned peaks belong to thimble tube vibrations.

### 2.2.2 Coherences and phases between detector pairs at the same axial elevation

As mentioned earlier, the coherence and phase data may be suitable to detect thimble tube vibrations (or vibrations of other components) in between the line of the detectors, which are aligned in columns  $N$  and  $L$ . Similarly to the analysis in [4], since 4 detectors can be paired in 6 different ways, together with the 6 axial positions this gives a large data volume which is difficult to display. Hence the results are shown such that several configurations are grouped together, for a more condensed representation. In Figs 2.6 and 2.7 the coherence and phase between the pairs A-B, A-C and A-D are shown for the three upper and three lower axial positions, respectively; in Figs 2.8 and 2.9 the pairs B-C, B-D and C-D, are shown for the same axial positions.

Similarly to the measurements taken in 2008 and analysed in Stage 2018 [4], the coherence is only high at the low frequency region, up to 8 - 10 Hz. However, whereas in the previous measurements in R4 there was a broad peak centered around 6 - 8 Hz, here there is a peak at around 1 Hz and another one around 8 Hz. In the coherence between detector A and the other three, there is a marked difference between the upper and the lower axial positions; in the upper three positions, there are two separate peaks, in the lower three positions there is one broad peak. This peak is however narrower at the bottom (position 6). In the pairwise coherences between detectors B - D, only the broad peak is seen.

The phase between all detector combinations for all axial elevations is zero up to about 15 Hz. This is a difference from the 2008 measurements where out-of-phase behaviour was found between detector E, lying somewhat apart from the other four detectors, and three of the others, hence one could suspect presence of vibrations between the “outlying” detector and the others, whereas the detector itself in the group of four not showing opposite phase was suspected to execute vibrations. From the current measurements one can draw the conclusion that no thimble tube vibrations (or vibrations of other components) can be detected between the “line of

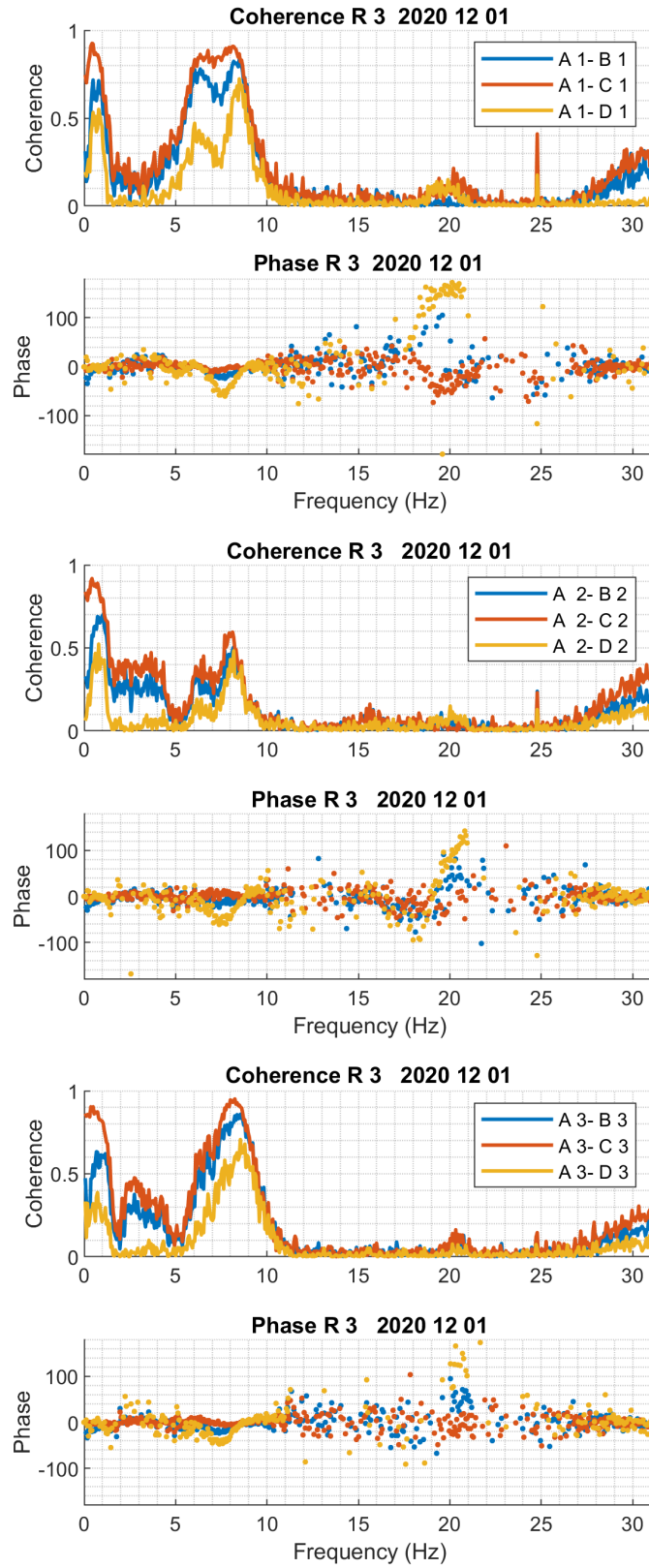


Figure 2.6: Coherence and phase between the pairs A-B, A-C and A-D for the three upper axial positions.



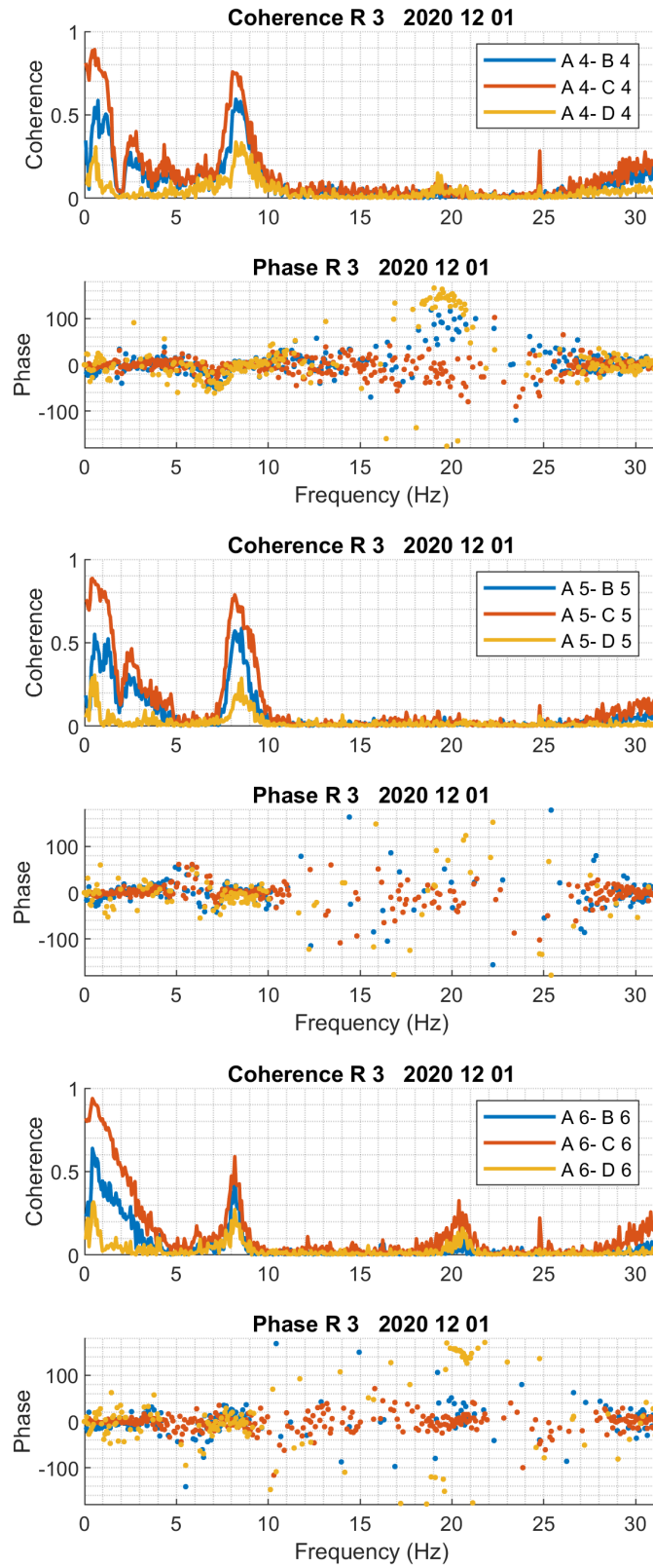


Figure 2.7: Coherence and phase between the pairs A-B, A-C and A-D for the three lower axial positions.

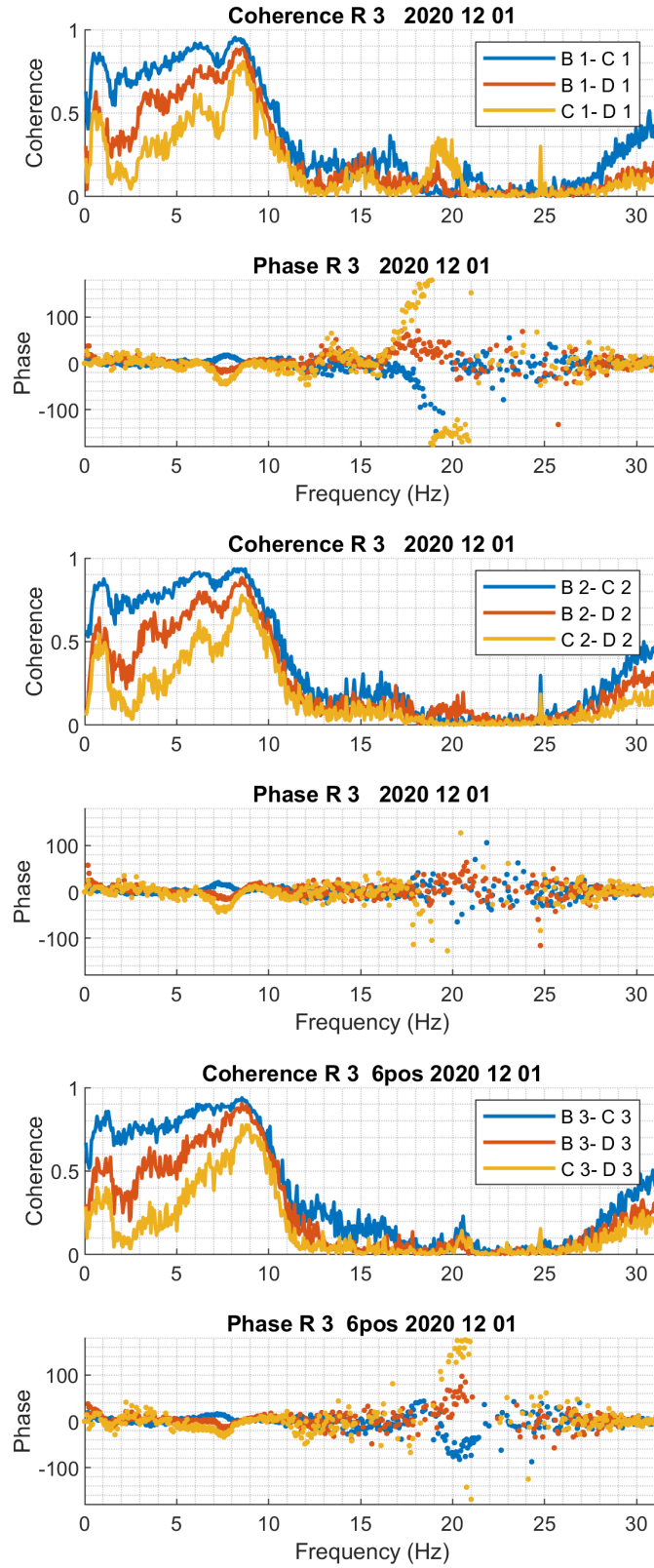


Figure 2.8: Coherence and phase between the pairs B-C, B-D and C-D for the three lower axial positions.

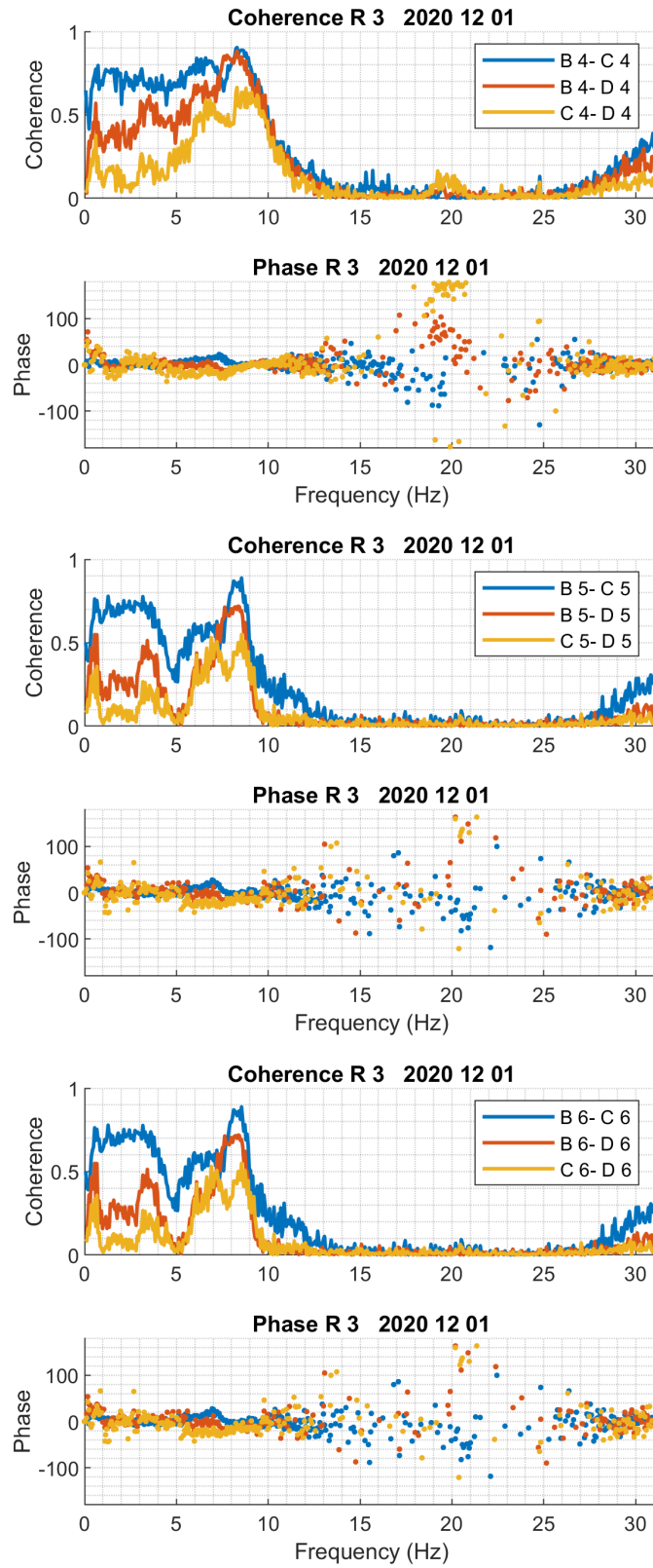


Figure 2.9: Coherence and phase between the pairs B-C, B-D and C-D for the three lower axial positions.

sight” of the four detectors.

Similarly to the results in Stage 2018, out-of-phase behaviour can be seen around 20 Hz between several detector pairs, mainly between A-D, and to a lesser extent between A-B and C-D. Out-of-phase behaviour is seen in some cases even around 15 Hz. It is interesting to note that opposite phase occurs mostly between detectors which are not neighbours; this was the case also in the 2008 measurements. This suggests that the opposite phase is not due to thimble tube vibrations, rather to the shell mode vibrations of the core barrel, which are also sensed by the inc-core detectors. In such a case detectors in different quadrants of the core should exhibit out-of-phase relationships. Nevertheless, the coherence is practically zero in this frequency region, and the phase values also show a large scatter, so no concrete conclusion can be drawn from the out-of-phase behaviour around 20 Hz.

### 2.3 Summary

From the above one can draw the conclusion that no thimble tube vibrations in the non-instrumented (i.e. detector-free) positions can be suspected. From the APSDs one might suspect vibrations of detector D, and possibly detector A and B. Hence it would be worth inspecting the thimble tubes in positions L04, N12 and N08, respectively. Results from EC-measurements of thimble tube thickness during the 2021-outage at Ringhals 3 show noticeable wear (at the height corresponding to the contact surface between the fuel assembly bottom nozzle and the thimble tube) at positions L04, and slightly less and similar for positions N08 and N12 for the most recent cycle. No wear could be detected in position N10. These inspection results are consistent with the initial findings in the analysis.

The analysis and the discussion above suggests that one has a larger chance to detect vibrations in the thimble tube positions which contain a detector. Therefore one might consider making a bigger campaign and making measurements in all thimble tube positions. The use of accelerometers, as is described in [3], could also be considered.

A completely different approach could be to try to extract the same information from neutron noise measurements that the EDF work did with accelerometers. In this latter case, one is looking for spikes in the recorded signal, indicating impacting. This again reminds to the analysis of BWR instrument tube impacting. There we tried to attempt detecting impacting from the measured neutron noise. Since, unlike in the case of accelerators where spikes are rather visible directly on the time series recording, in the neutron noise such spikes (which have a much smaller amplitude) are buried in a huge background signal. Hence we used advanced wavelet *filtering* techniques for the detection of such spikes [14, 15, 16]. Although the tools for this are not available to us any longer, they could be elaborated again and used in the next Stage to try to find impacting from the in-core neutron noise.

### 3. EVALUATION OF NEW EX-CORE MEASUREMENTS FOR BEAM MODE AND TILTING MODE VIBRATIONS IN R3

#### 3.1 Introduction and background

The analysis of core-barrel vibration properties (often abbreviated to CBM, core barrel motion) have been the subject of study both in Sweden and internationally. It has also been the subject of the collaboration between Chalmers and Ringhals from the beginning, as it was reported in several previous Stages in the Ringhals diagnostic project [17, 18, 19, 20, 9, 10, 13, 21, 22, 23, 24, 4, 25].

Within the last decade, a series of studies dedicated to core barrel vibrations have been performed in order to analyse and find a suitable explanation for the recent observations of wear at both the lower and upper core-barrel-support structures, i.e. the lower radial key and the reactor vessel alignment pins in the Ringhals PWRs. In the last few years the main focus in this area was put on the investigation of a double peak observed in the Auto Power Spectral Density (APSD) in the frequency region of the beam mode component, mostly in measurements made in R4. A hypothesis was formulated about the nature of this peak, where it was suggested that the lower frequency peak is due to the beam mode vibrations and the upper peak is due to fuel assembly vibrations. A test of this hypothesis was one of the main targets of the analysis. A key factor of the analysis was to assume that the lower frequency peak is due to the (coherent) vibrations of the whole core barrel, hence the symmetries between the ex-core detectors could be used to enhance the effect, as well as to condense the quantification to one single parameter by taking combinations of the detector signals. However, since the higher frequency mode was assumed to be due to the effect of the independent (incoherent) vibrations of the individual fuel assemblies, no symmetries could be utilised, and the results could not be condensed into one single parameter.

In 2014 a further, new assumption was made, in that the main effect of the individual vibrations manifests itself through the combined reactivity effect of all the individually vibrating fuel assemblies. This assumption, through the associated symmetries of the reactivity component, allowed to condense the analysis of the different detector signals into one single parameter even for the higher frequency peak. This hypothesis was tested with a positive outcome on the measurements taken at Ringhals-4. In addition, although no double peak was visible in the APSDs of the R3 measurements, with the peak separation and curve fitting technique, the two peaks could be separated even in the R3 measurements. Thus, finally, it became possible to distinguish between the beam mode component due to core barrel vibrations and the reactivity component associated to the single fuel assembly vibrations. In addition, through numerical simulations, it was also possible to confirm the constant amplitude within one fuel cycle for the beam mode component, and the varying amplitude (within one cycle) of the reactivity component (individual fuel assembly vibrations), which were in good agreement with the original hypothesis.

The work in the continuation was therefore not concentrated any longer to the test and proof of the hypothesis, and the associated trend analysis of the evolution of the peak amplitudes during the cycle, rather on checking whether there is any major change in the amplitude and frequency of the beam mode peaks, as compared to the previous measurements, which could indicate an increased play in the lower radial key support. A special circumstance in this aspect is that in 2015, the total power of Ringhals-4 was increased by 18.6 %. Another aspect is that some structural changes took place in R4. The hold-down springs were replaced during the outage in 2013, and the interior parts were lifted out during the outage in 2014 for an inspection. As it was seen and reported in the previous Stages [24, 4], this has changed the shape of the spectra around the beam mode frequency such that the visibility of the former double peak has ceased and only one peak could be observed visually. As the results of the previous Stage showed, by this change, the ex-core neutron spectra became very similar between R3 and R4.

Lastly, as it was described in the previous Stages [23, 24, 4, 25], a new type of pivotal vibration mode, which we named as “tilting” or “wobbling” mode, was discovered. The separation of the tilting mode from the other components is made with methods similar to the other mode separation methods with adding and subtracting the signals in various combinations. The only difference is that for the separation of the tilting mode from the other components, all 8 detectors (the four ex-core detectors at two axial elevations) need to be used. Hence in the routine analysis, the separation of all four components (beam, shell, reactivity and tilting modes) has been made in the continuation.

In the previous two Stages (2018-19 and 2019-20), the ex-core measurements were made in R3. Since in the years preceding the year 2018, the ex-core measurements were performed in R4, in Stage 2018 there was no possibility to compare the new measurements with immediately previous ones taken in R3. It has to be added that there were measurements made in the first half of 2018, but a detailed evaluation and analysis of those measurements was not included either in Stage 2016-2017 or in Stage 2018-19 (there was a gap between Stages 2016 and 2018). Hence in Stage 2018, the structure of the spectra could not be compared with immediate past measurements, and no long-term trend analysis was presented. One could only note that unlike in the previous R4 measurements, the double peak at 8 Hz could not be seen in the spectra, they could only be separated by a refined curve fitting procedure. The within-cycle trend analysis showed that the two modes around 8 Hz behaved practically the same way within the cycle, which was another difference compared to the previous R4 measurements.

In Stage 2019, the ex-core measurements were made again in R3, which gave a possibility to compare the measurements with those of Stage 2018. It was found that both the structure of the peaks in the APSDs, the coherences and phases, as well as the within-cycle trend analysis, showed a considerable resemblance between those two stages, i.e. both Modes around 7-8 Hz, which cannot be separated by visual inspection in the spectra, only by the mode separation technique, change similarly during the cycle. One difference between Stages 2018 and 2019 is that in the latter, a long term trend analysis was also performed. Namely, the two measurements

taken in the first half of 2018 (23 January and 24 April), were included into a trend analysis presented in Stage 2019, with only the amplitudes of the beam mode and reactivity mode being taken into account. This way, the long term trend analysis could stretch over 3 calendar years.

In the present Stage the ex-core measurements were made yet again in R3, which now lends the possibility to an even longer long term trend analysis. Both the trend analysis, as well as the detailed analysis of the structure of the spectra and the coherences and phases is interesting to compare with the two previous Stages, in that during the outage/refuelling preceding the present Stage, and upflow conversion was performed, in order to decrease the possibility of baffle jetting. This is also the reason why no analysis of the in-core measurements concerning baffle jetting was performed. One drawback of the measurements in the present Stage is that due to the Covid-19 situation, only 2 ex-core measurements could be performed, which makes primarily the in-cycle trend analysis, but to some extent even the long-term trend analysis, less accurate.

Summarising the results of the analysis described in the continuation, one can say that the structure of the spectra, and the character of the in-cycle trend analysis, is extremely similar to that of the two preceding Stages. The long-term trend, however, shows that the long-term increase of the vibration components, i.e. that of the beam mode and the reactivity component, is stopped, and the amplitudes in this year are lower than for the preceding Stage for the beam mode, and even lower than the preceding two Stages for the reactivity component. The long-term trend indicates that the upflow conversion might have had a beneficial effect on the magnitude of the vibrations, whereas the structure of the spectra shows that no significant qualitative change of the vibration properties can be noted.

### **3.2 Details of the measurements in R3**

Two sets of measurements were analysed. The measurements were performed in R3 in cycle 38, on 29 October 2020, and 21 April 2021. For simplicity they will be referred to as Measurement 1 and 2, respectively. The sampling frequency was 62.5 Hz for all three sets of measurements. The detectors used and the registered quantities (static and fluctuating parts, i.e. DC and AC, respectively) are shown in Table 3.1. More detailed data regarding settings and general parameters can be found in the measurement protocols from previous measurements, which were performed in an identical manner [26, 27, 28].

### **3.3 Analysis of the measurements made on 2020-10-29 (Measurement 1)**

#### **3.3.1 Individual spectra of all detectors**

In summary, it can be stated that what regards the peak structure of the spectra, the results of the present Stage are in a rather good agreement with those in the two previous Stages. There are certain smaller deviations, but they do not bear much significance. However, several of the amplitudes of the known peaks changed as compared to the previous Stages. This concerns the amplitudes of the beam mode and the tilting mode, as well as the long-term trend, as it will be shown and

Table 3.1: The measurement data structure of the three measurements in Ringhals 3 during 2019-20.

Channel	Measurement point
0	Time
1	N41U DC
2	N42U DC
3	N43U DC
4	N44U DC
5	N41L DC
6	N42L DC
7	N43L DC
8	N44L DC
9	N41U AC
10	N42U AC
11	N43U AC
12	N44U AC
13	N41L AC
14	N42L AC
15	N43L AC
16	N44L AC



discussed later. These changes are consistent with each other, and they may be attributed to the upflow conversion.

The APSDs of all eight individual detector signals are shown in Fig. 3.1. They are very similar to those from the previous two Stages. All signals show the two familiar peaks around 8 and 20 Hz for the beam and shell modes, respectively. Similarly to the previous measurements made in R3, as well as in the latest measurements in R4, no double peak is visible at 8 Hz. Rather, similarly to the immediate two previous measurements, a small peak is visible around 6 Hz in most, but not all detector spectra, i.e. it is more separated from the 8 Hz peak in frequency. Another similarity is that the peak at 20 Hz seems to have a small second hump in all signals.

Similarly to the previous two Stages, the two peaks that we earlier identified with the beam mode and the reactivity mode (the latter corresponding to the noise induced by the individual fuel assembly vibrations) and which were seen in older measurements, cannot now be visibly separated. As also mentioned in the previous Stages, after the replacement of the hold-down springs in R4 during the outage in 2013, and lifting out the interior parts during the outage in 2014 for an inspection, the ex-core detector spectra in R4 and R3 look now rather similar.

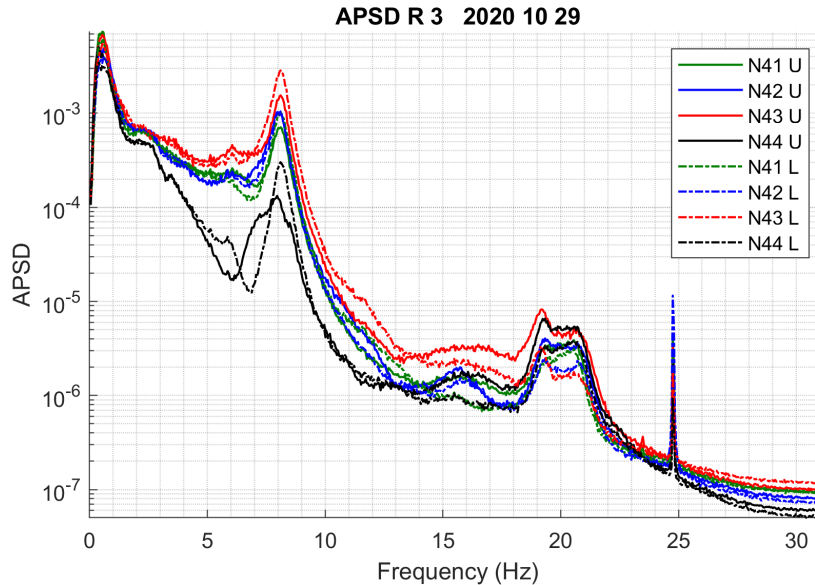


Figure 3.1: APSDs of all 8 ex-core detector signals from Measurement 1

### 3.3.2 Results of the mode separation

The beam mode, shell mode, reactivity component and the tilting modes were separated according to the detector signal combination principles as in the previous work. In order to have compatibility between the measurements for different cycles, in the evaluations the fluctuating part of the signals is normalised to the their mean values. This means that e.g. the autospectra, calculated from the AC components are divided by the square of the corresponding DC signal. This makes the measurements independent of the local static power levels for the different measurements, and guarantees the validity of the long term trend analysis, where measurement

data from the different cycles are compared.

The results are shown for both the upper and the lower detectors in Fig. 3.2. The results of the separation are rather similar for the two cases, as well as to those

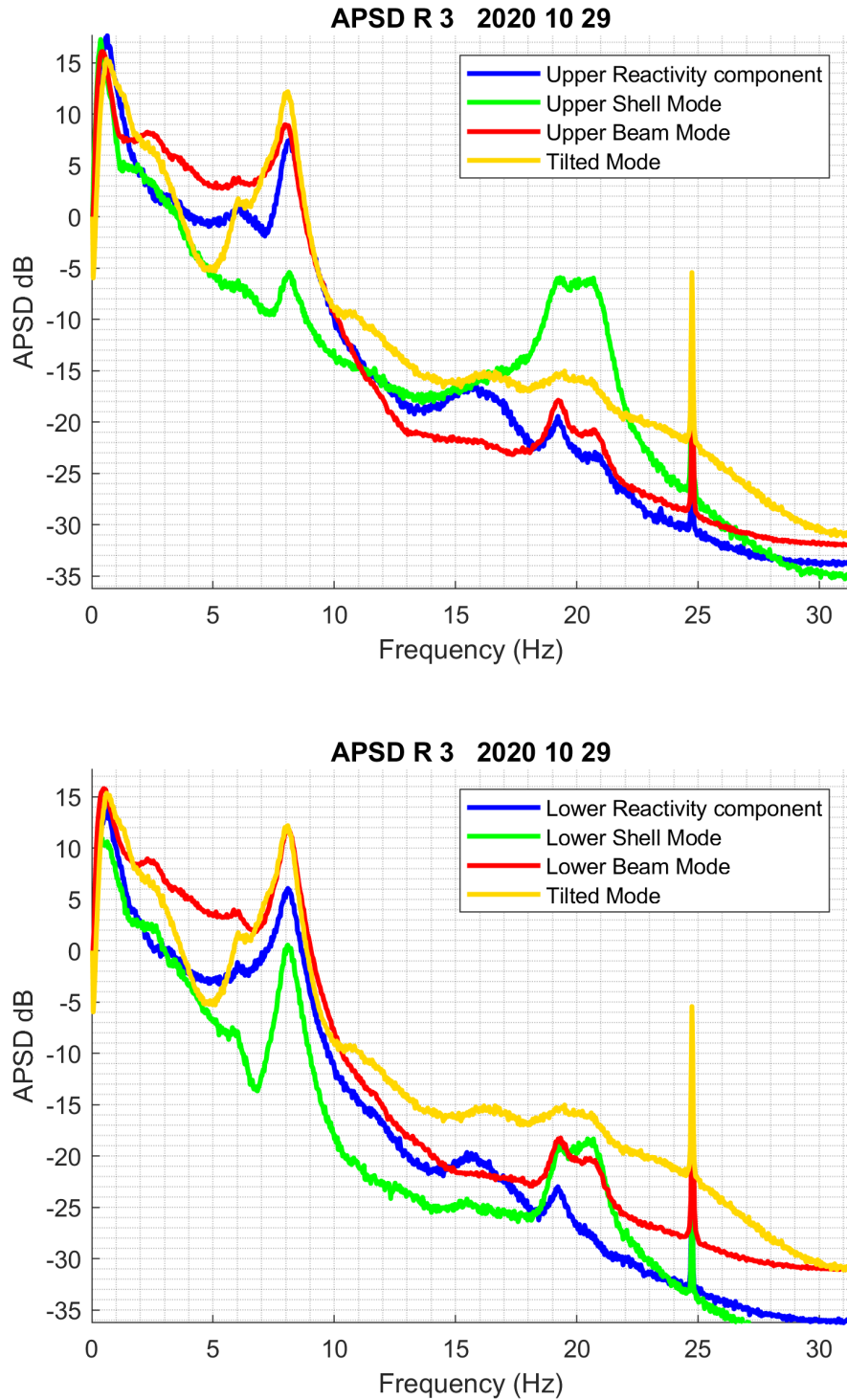


Figure 3.2: APSDs of the beam mode, shell mode, reactivity component and the tilting mode for the upper detectors (upper figure) and the lower detectors (lower figure), extracted from Measurement 1.

of the previous two Stages. For instance, the peculiarity, observed in the previous two Stages still exists, namely that the shell mode, which shows only a small peak at 8 Hz in the upper detectors signals (which is expected) has a quite distinct peak at 8 Hz in the lower detector signals (not expected). Like in the previous two stages, we have no explanation of this fact, but it seems to be consistently present in the last three Stages (including the present one).

It is also seen that the amplitude of the beam mode is still larger for the lower detectors, as has been the case in all previous measurements and which is expected, whereas the amplitude of the other components is very similar for the upper and lower detectors. However, compared with the previous two Stages, the difference between the upper and lower beam mode peak amplitudes is smaller in the present measurements. This can most likely be attributed to the effect of the upflow conversion.

Yet another new observation is that the amplitude of the tilted mode has increased as compared to its value in the previous two Stages. Actually it is larger than any of the other modes in both the upper and in the lower detector signals. This again might be the effect of the upflow conversion.

Similarly to the results of Stage 2016 [24], reporting on measurements made in R4, as well as Stages 2018 [4] and 2019 [25], (both in R3), one notes a small peak around 15.5 Hz in both the upper and the lower detector signals in the reactivity component. In Stage 2016 our interpretation was that since this frequency is about twice that of the pendular fuel vibration frequency at 8 Hz, which is also identified as a reactivity effect, the peak at 16 Hz can be attributed to the higher harmonics of the fuel assembly vibrations at the fundamental frequency 8 Hz. However, based on the analysis of the baffle jet effect in Stage 2018, it is more likely that this peak is due to the “core flowering” effect, i.e. the zeroth azimuthal mode of the core barrel.

A rocking mode of the reactor pressure vessel (RPV) may also be expected in, or slightly above, frequencies around 16 Hz. For symmetry reasons, it is more reasonable that any contribution from the rocking mode is enhanced in the beam-mode components displayed in Figs. 3.2 and 3.7. In these figures, contributions from the beam-mode component are also seen in the broader frequency range associated with shell-mode vibrations, which could be an indication of the RPV-rocking mode. This could be further investigated in the coming stages.

### 3.3.3 Phase and coherence relationships between the upper and lower detectors

An analysis of the coherence and the phase relationships between detectors at the same and different axial levels was performed, similarly to that in the previous stages. The coherence and phase between the diagonally opposite detectors N41 and N42, for both the same and different axial levels, is shown in Fig. 3.3, and the same for detectors N43 and N44 in Fig. 3.4. The coherence and phase between the upper and lower detectors at the same radial position, for all four detectors, is shown in Fig. 3.5.

These results are again similar to those of the previous two Stages, but some

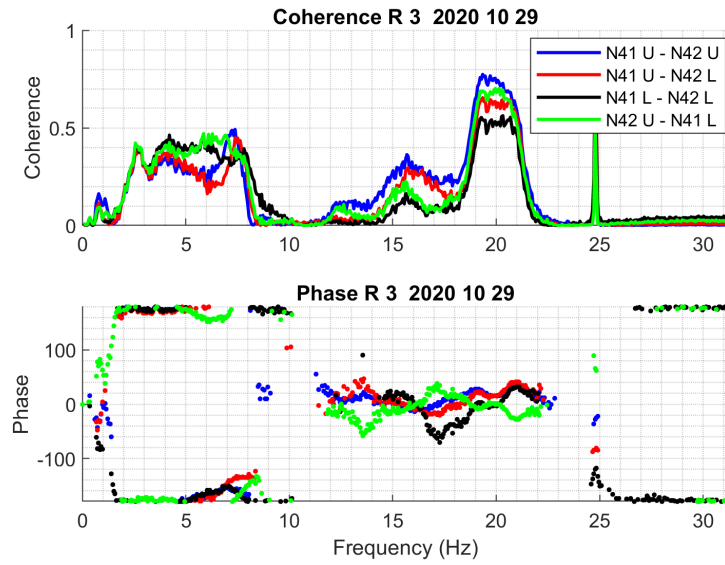


Figure 3.3: The coherence and the phase of the CPSD calculated for the N41U-N42U, N41U-N42L, N41L-N42L and N42U-N41L detector pairs in Measurement 1.

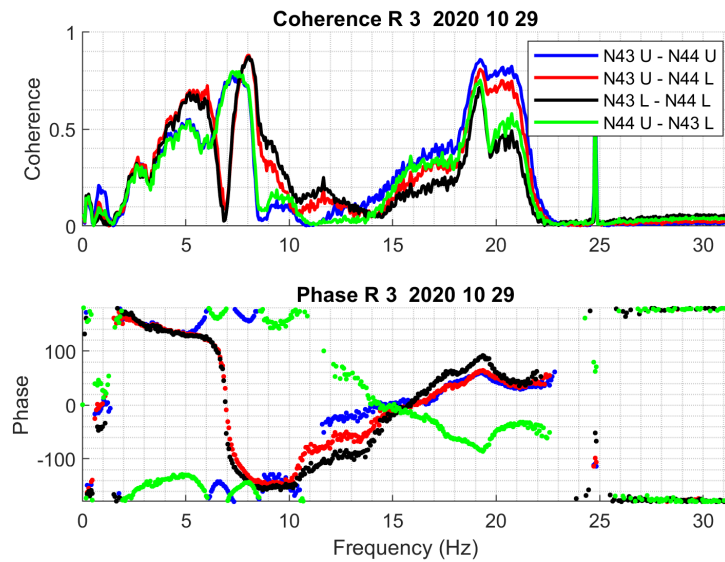


Figure 3.4: The coherence and the phase of the CPSD calculated for the N43U-N44U, N43U-N44L, N43L-N44L and N44U-N43L detector pairs in Measurement 1.

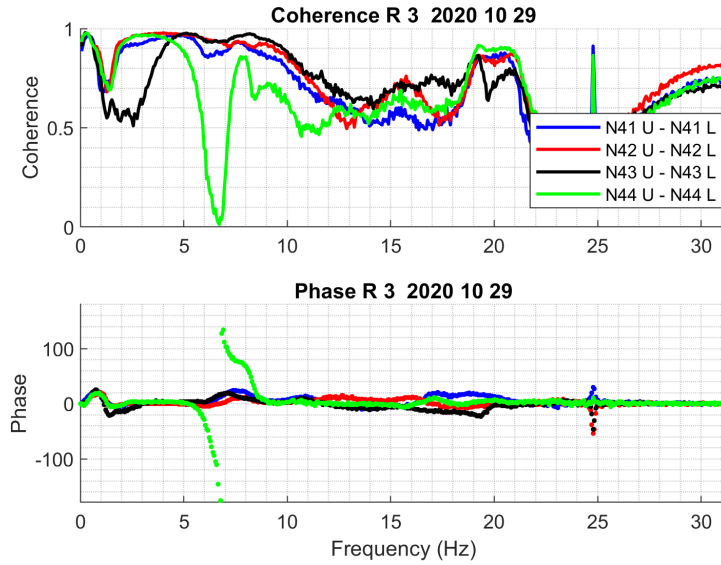


Figure 3.5: The coherence and the phase of the CPSD calculated for the N41U-N41L, N42U-N42L, N43U-N43L and N44U-N44L detector pairs in Measurement 1.

differences can be noticed. In Stages 2018 and 2019, for the detector pair N41 - N42, (Fig. 3.3 in the present report), the coherence differed from the previous R4 patterns. Unlike in the R4 measurements, the coherence around 8 Hz was very low, which is surprising, given the fact that the APSD peaks are the highest in this frequency region, and the phase is rather solidly  $180^\circ$  (as expected for the beam mode vibrations), without much scatter, up to about 8 Hz, where it shifts to zero. The coherence had a medium large peak at around 4 Hz, which is somewhat more resembling to the former measurements in R4.

In the present Stage, the behaviour of the phase is still similar. The phase behaviour is in line with the previous R4 measurements, and also with the expectation that just below 8 Hz the beam mode vibrations dominate, which is the cause of the out-of-phase behaviour, after which, at a slightly higher frequency, the reactivity effect of the fuel assembly vibrations take over, which is the cause of the zero phase above 8 Hz.

However, the coherence looks different around and below 8 Hz. Although it is still not as high as at 20 Hz, the coherence has increased between 3 - 8 Hz, and it is noticeably higher around 8 Hz than in the previous two Stages. In the previous two Stages it was surmised that a possible explanation of the low coherence at 8 Hz was that the beam mode vibrations were highly anisotropic, and are perpendicular to the line connecting the detectors N41 - N42, or if there was an interference between the beam mode, the reactivity mode and the tilting mode. Since now the coherence is higher, one does not need to look for an explanation, but if the previous arguments were valid, then it means that the beam mode vibrations are more isotropic, and there is less interference between the various components. As it is seen in Fig. 3.2, all these components have comparable amplitudes at 8 Hz, but they are not correlated to each other. As it was also mentioned, the amplitude of the tilted mode has increased, which might have a reason which is in common with the increase of

the coherence.

As in the preceding two Stages, the picture is rather different for the detector pairs N43 - N44, Fig. 3.4, compared to the pairs N41 - N42. The picture is similar both to the previous two Stages and to the former R4 measurements, in that the coherence is much larger at 8 Hz, more corresponding to the expectations, than for N42 - N42. The coherence is high for all four pair combinations, similarly to Stage 2019, whereas in Stage 2018, it was only high for two of the four possible detector combinations. One difference against the previous Stage is that the dip in the coherence around 7 Hz for N43U - N44L and N43L - N44L is now deeper. The origin of this dip, which is also seen in the coherence between N44U - N44L, is still not known.

The phase behaviour also resembles to that in the previous Stage, in that for the combinations N43U-N44U and N44U-N43L, it shows the same out-of-phase behaviour as for the detectors N41 and N42, whereas the other two pairs it changes continuously from  $180^\circ$  to  $-180^\circ$ .

As discussed in the previous report, this type of shifting (not constant) phase behaviour is unknown from previous measurements, and it is rather difficult to interpret in the context of core barrel vibrations. A linear phase between two detectors is an indicator of a (deterministic) time delay between the two signals, which is hardly conceivable for the ex-core detector signals induced by vibrations. One cannot exclude though the possibility that the vibrations are periodic and not random, in which case the conclusions drawn from the coherence and phase are not valid, since these are only defined for random processes. However, the large qualitative difference between the phase and coherence between the pairs N41 - N42 on the one hand and N43 - N44 on the other, supports the assumption that the CBM may be relatively strongly anisotropic.

Regarding the axial coherence and phase between detectors at the same radial position, Fig. 3.5, these are very similar to those of the previous two Stages. There is a quite deep dip in the coherence and a deviation from zero phase at 6 Hz only for the detectors N44 upper and lower. All other three radial pairs have high coherence and zero phase throughout this region. Similar deviation between one detector and the other three has also been observed in other measurements, both in R3 and R4.

### 3.4 Analysis of the measurements made on 2021-04-01 (Measurement 2)

#### 3.4.1 Individual spectra of all detectors

The APSDs of all eight individual detector signals are shown in Fig. 3.6. These look very similar to those in Measurement 1. Similarly to the previous Stages, a moderate increase of the amplitude of the 8Hz peak is seen. This is basically the expression of the known within-cycle term, which is manifested by the increase of the amplitude of the beam mode vibrations.

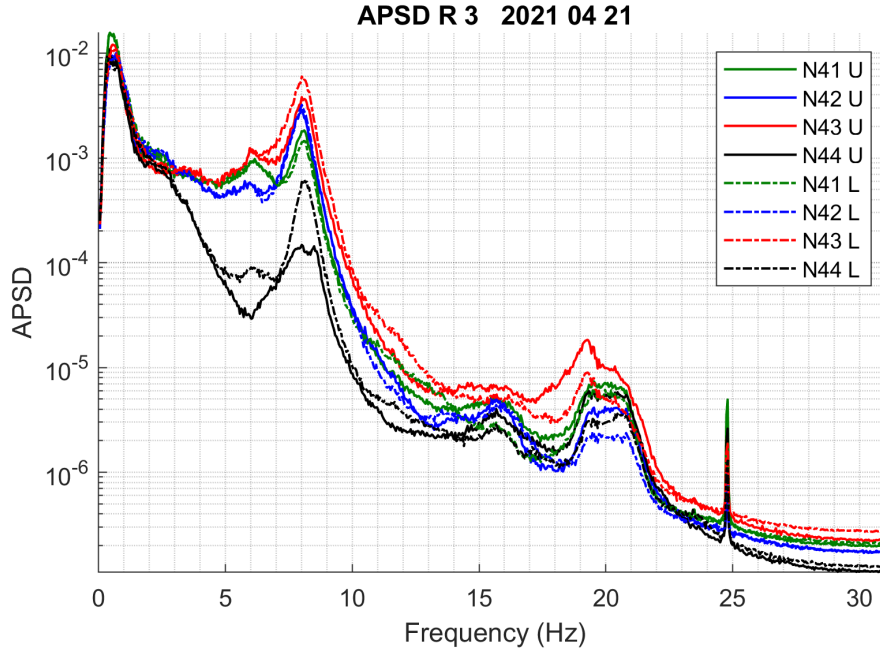


Figure 3.6: APSDs of all 8 ex-core detector signals from Measurement 2

### 3.4.2 Results of the mode separation

The results for the separation of the beam mode, shell mode, reactivity component and the tilting modes are shown for the upper and the lower detectors in Fig. 3.7. These results are very similar to those of Measurement 1, which include the apparent deviations from the previous two Stages. One is the fact that the difference in the beam mode amplitude between the upper and the lower detectors has nearly disappeared, or at any rate decreased significantly. As with Measurement 1, the most likely reason for this is the compensating effect of the upflow conversion.

The increase of the amplitude of the tilting mode as compared to the previous two Stages is observed too, similarly as in Measurement 1. This change can also be attributed to the upflow conversion. In summary one might suspect that the upflow conversion primarily decreased the vibration amplitudes in the lower part of the core and possible increased them in the upper part. This is consistent with both the increased similarity of the pendular mode between the upper and lower levels, as well as the increase of the amplitude of the tilted mode vibrations. One might conclude that the upflow conversion had a beneficial effect by decreasing differences at the upper and lower levels.

Another difference to Measurement 1, but showing a similarity with the previous Stage, is that the amplitude of shell mode at 8 Hz has decreased somewhat in the lower detectors.



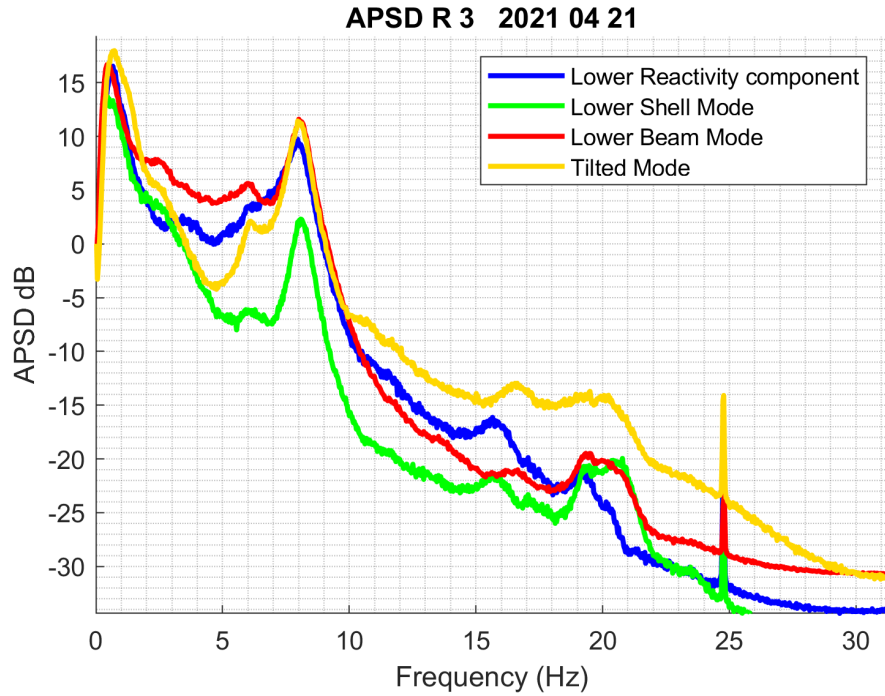
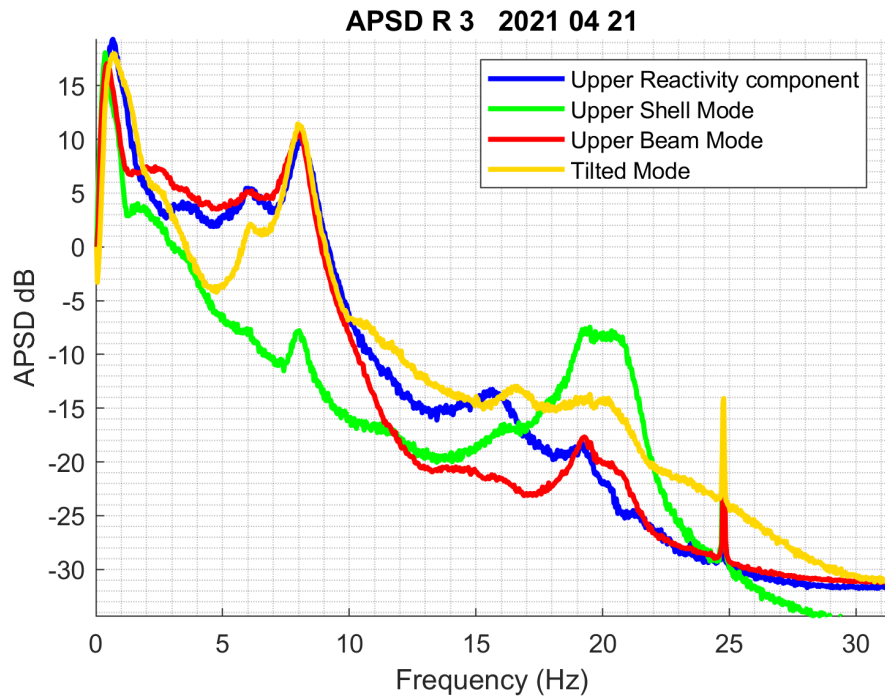


Figure 3.7: APSDs of the beam mode, shell mode, reactivity component and the tilting mode for the upper detectors (top figure) and the lower detectors (bottom figure), extracted from Measurement 2



### 3.4.3 Phase and coherence relationships between the upper and lower detectors

The coherences and phases between the diagonally opposite detectors N41 and N42, for both the same and different axial levels, are shown in Fig. 3.8, and the same for detectors N43 and N44 in Fig. 3.9. The coherences and phases between the upper and lower detectors at the same radial positions, for all four detectors, are shown in Fig. 3.10.

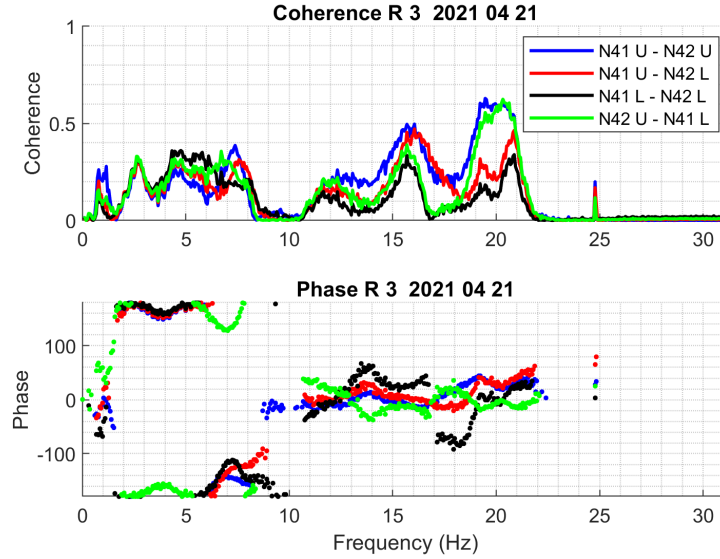


Figure 3.8: The coherence and the phase of the CPSD calculated for the N41U-N42U, N41U-N42L, N41L-N42L and N42U-N41L detector pairs in Measurement 2.

These coherence and phase plots show mostly strong resemblance to those in Measurement 1, and to the results of the previous Stage, but there are also some visible deviations. One is that in the pair N41 - N42, the coherence decreased somewhat in the range 3 - 8 Hz, although it is still larger than in the previous Stage. In the pair N43 - N44, the coherence is still high at 8 Hz, but it decreased noticeably below 6 Hz. In the phase of the same pair, the transition from  $180^\circ$  to  $-180^\circ$  takes place over a larger frequency region, i.e. the transition is even slower than in Measurement 1. In the phase of the axial detector pair N44U - N44L, which behaves differently from the other three pairs, the deviation of the phase from zero at around 6-7 Hz has very different structure to that in Measurement 1 and Stage 2019. Apart from these differences, the rest of the interpretations and remarks are the same as for Measurement 1.

### 3.5 Trend analysis within the cycle

Whenever there are three measurements available in a cycle, a trend analysis, showing the development of the amplitudes of the beam and reactivity modes, also called Mode 1 and Mode 2, is of interest. As noted in the previous reports, this analysis has been relatively difficult in the last measurements both in R3 and R4, due to the difficulties in separating two peaks very close to each other in frequency.

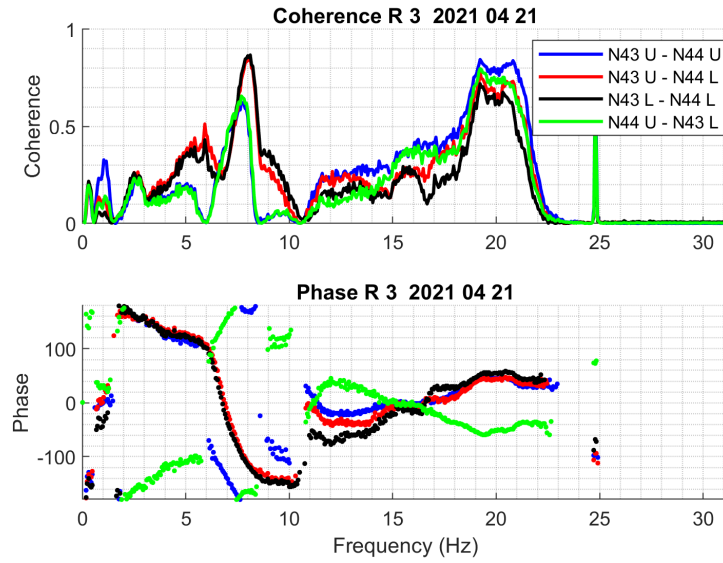


Figure 3.9: The coherence and the phase of the CPSD calculated for the N43U-N44U, N43U-N44L, N43L-N44L and N44U-N43L detector pairs in Measurement 2.

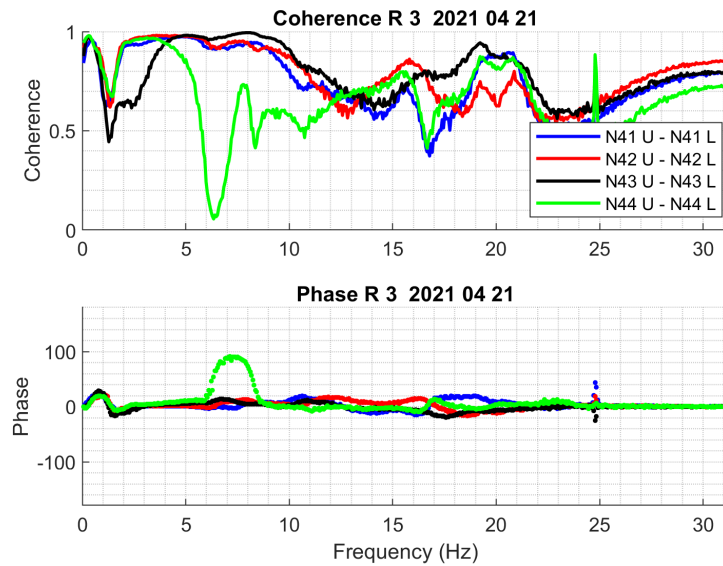


Figure 3.10: The coherence and the phase of the CPSD calculated for the N41U-N41L, N42U-N42L, N43U-N43L and N44U-N44L detector pairs in Measurement 2.

Therefore some further refinement of the curve fitting and mode separation method was made by our collaborators at UPM when evaluating the measurements in Stage 2019. The algorithm itself was not changed, but the way it is applied was improved based on the accumulated user experience. The fitted parameters are found in an iteration process, and the accuracy of the parameter fitting can be improved by refining the criteria for the termination of the iterations, which leads to performing more iterations. This improved iteration process was used the first time in the previous Stage, and also in the analysis of the results this year.

However, due to the known circumstances, in the present Stage only two ex-core measurements were possible to make. A third, reduced measurement was made at the time of the in-core measurements, but since the number of signals that can be registered simultaneously is 16, the in-core signals took the place of some ex-core registrations, hence the ex-core measurements could not be evaluated. Nevertheless, a two-point trend analysis was still performed and is presented below.

The results of the curve fitting are illustrated in Fig. 3.11 for both the upper and the lower detectors from Measurement 1 and Measurement 2. These show a similarity to the results from the previous Stage, although there are some deviations both in the shape and the amplitude of the peaks.

The results of the trend analysis for both Modes are shown in Fig. 3.12. Since only two measurements are involved, one cannot draw conclusions whether the evolution was monotonic during the cycle or not. At any rate, one can note a similar increasing trend for both modes and both for the upper and the lower detectors. This behaviour is similar to the previous Stages, but it also deviates from the previous measurements in R4, where only one of the modes (Mode 2) did increase during the cycle.

As also mentioned in the previous Stage, this contradicts our previous hypothesis on the character and expected behaviour for the two Modes, according to which Mode 1 (the beam mode) is practically constant during the cycle and only Mode two (individual fuel vibrations) increase in amplitude. It is worth noting that the appearance of this behaviour, which deviates from the previous hypothesis, coincides with the time when the formerly visible two peaks became indistinguishable. Even if with rather refined methods we achieved a separation of the two peaks, since we find a similar behaviour for both modes, one might consider to give up the mode separation process, and only treat one peak in the continuation. On the other hand, the amplitude of the two components is different, which may serve some information to the long-term trend analysis, as will be seen below.

### 3.6 Long term trend analysis

Besides the trend analysis within the cycle, whenever sufficient data are available, it is also worth to perform a trend analysis over a longer period of time. This was the case already in the previous Stage, where such data for R3 from the three cycles 35, 36 and 37 could be used. With the data from the present Stage, with data from cycle 38, the long-term trend analysis can be made even more complete.

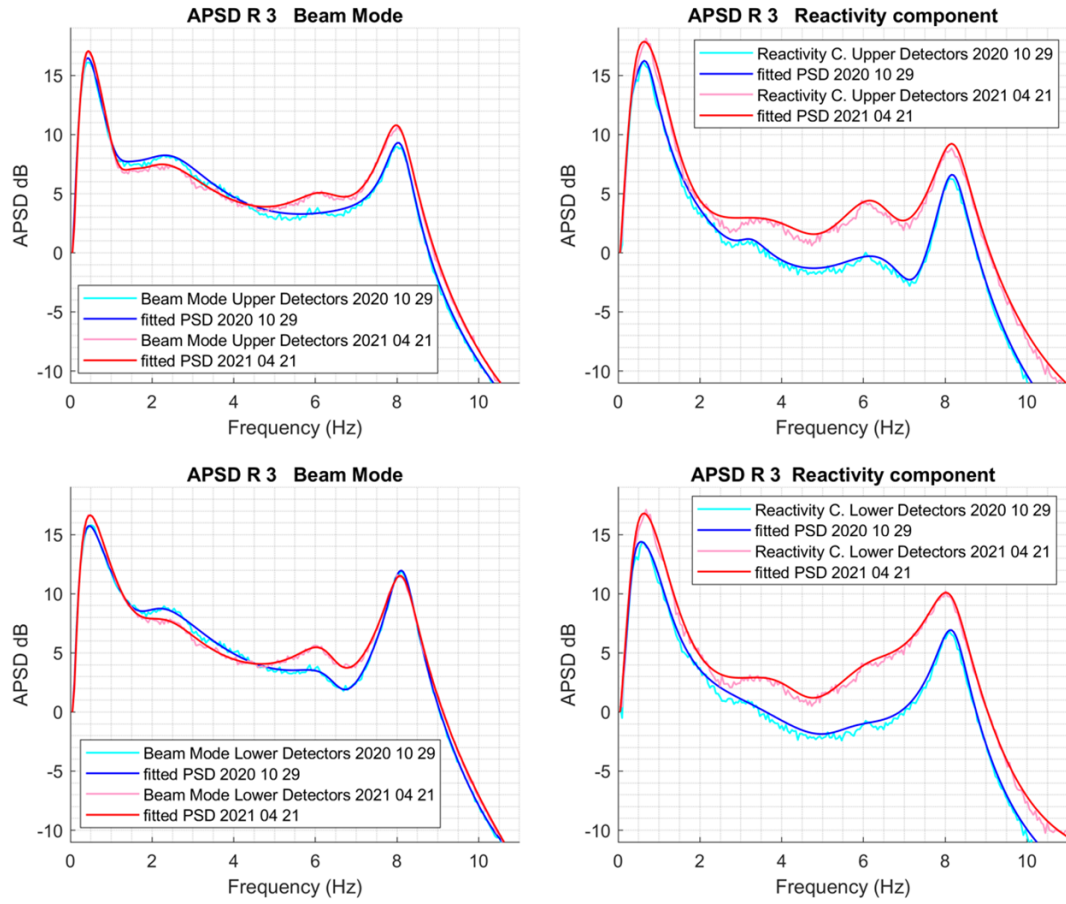


Figure 3.11: Results of the curve fitting for Measurements 1 and 2 to the peak around 8 Hz for the beam mode (left side), and the reactivity component (right side), both for the upper detectors (upper figures) and the lower detectors (lower figures).

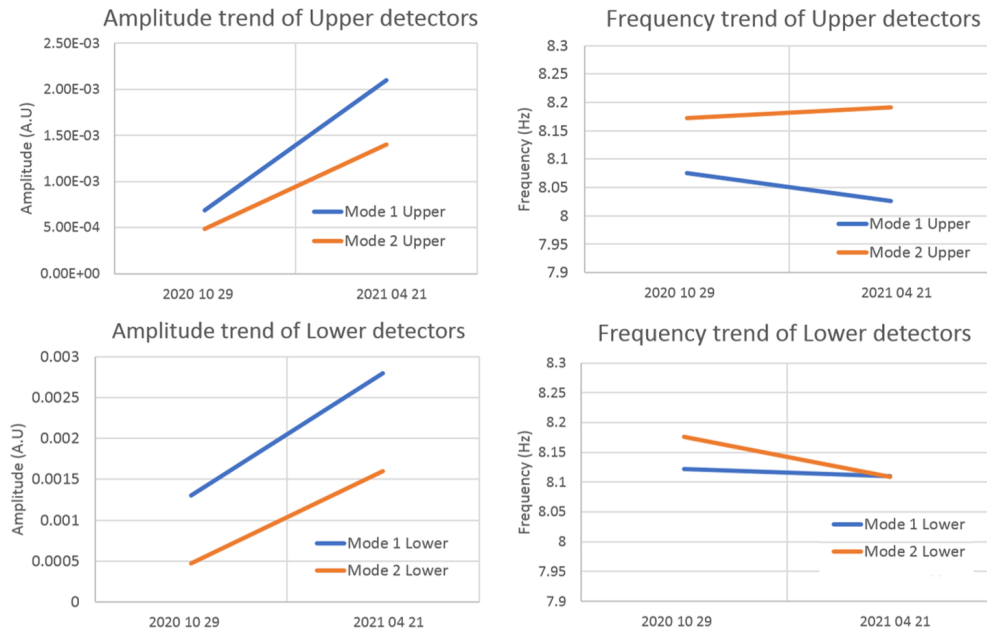


Figure 3.12: Trend analysis of the amplitude and frequency of the beam mode (Mode 1) and the reactivity component (Mode 2) at 8 Hz for the three measurements made during the cycle.

The results of the 4-year trend analysis for the beam mode are shown in Fig. 3.13 (in 2018, only two measurements were evaluated, as described in the previous report). In this figure both the within-cycle trend, as well as the long term trend is visible. From 2018 until the last Stage, one could note a slow long-term increase of the amplitude of the beam mode. In particular the amplitude values for the lower detectors increased by about 50% from the end of the cycles 36 (Stage 2018) to cycle 37 (Stage 2019). It was surmised that this can be an indication of the fact that the play of the Lower Radial Key has increased.

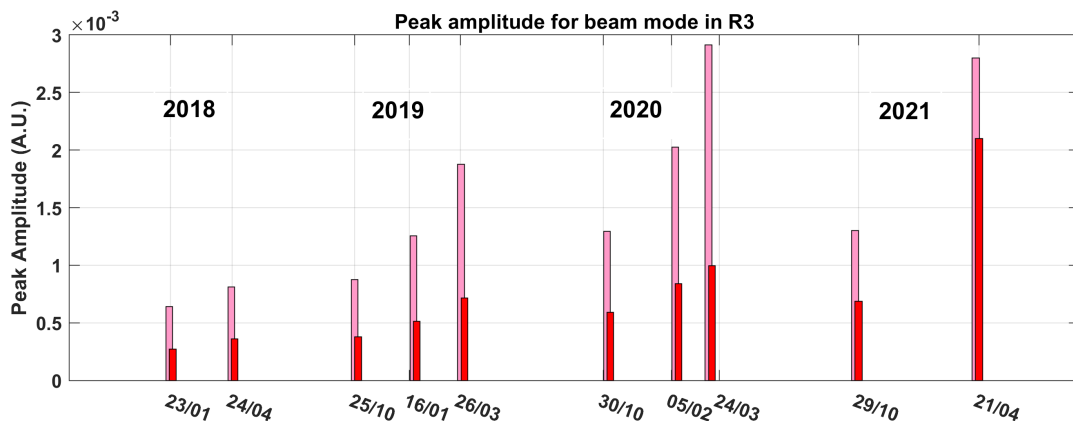


Figure 3.13: Four-year trend analysis of the amplitude of the beam mode (Mode 1). Red: upper detectors; pink: lower detectors.

However, as is seen on Fig. 3.13, in the last cycle the trend has reversed at least for the lower detectors. At the end of the cycle, the lower detectors show a

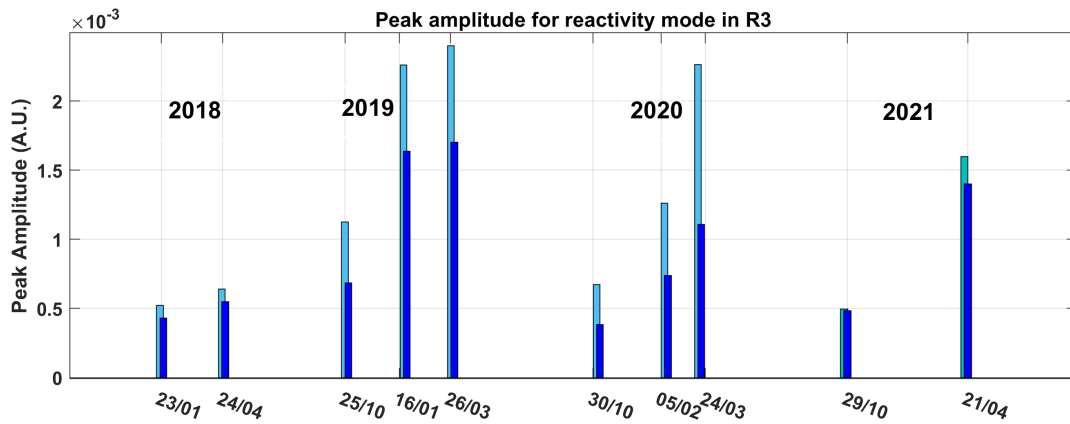


Figure 3.14: Four-year trend analysis of the amplitude of the reactivity mode (Mode 2). Dark blue: upper detectors; light blue: lower detectors.

definitely lower value than in the preceding cycle, whereas the amplitude of the upper detectors are larger than at the end of the previous cycle. As it was already noticed in the preceding chapters, the difference between the upper and lower detectors has definitely decreased. Again, this change is very likely due to the flow conversion. Because of this new characteristics, it will be interesting to follow up the evolution of the amplitudes in the next cycle.

The same analysis for the reactivity mode, associated with the individual fuel assembly vibrations, is shown on Fig. 3.14. Here the behaviour was different already in the previous Stage. There was an increase between 2018 and 2019, whereas there was no increase after 2019, rather the amplitudes were even slightly lower. It was noted that since the reactivity mode is associated with the fuel vibration properties, which may change after each new core loading, a somewhat irregular trend is not completely unexpected. In the last cycle, i.e. in the present Stage, the amplitudes have further decreased. The character of the change is very similar to that of the beam mode, namely that the decrease concerns the lower detector signals (which give the higher amplitude), and that the difference between the upper and lower detectors has decreased. Similarly to the beam mode, it will be interesting to see in the further cycles whether this change is stable.

## 4. EXPERIMENTAL WORK AND SIMULATIONS IN SUPPORT OF THE USE OF FISSION CHAMBERS IN THE CURRENT MODE FOR REACTIVITY MEASUREMENTS, AS AN ALTERNATIVE OF PULSE COUNTING METHODS

### 4.1 Introduction

In Stage 2016 [24] we suggested the possibility of using the continuous current of fission chambers to extract the same statistical information from a measurement as from the discrete events of pulse counting. Stochastic methods based on the statistics of pulse counting (variance to mean or Feynman-alpha and correlations, or Rossi-alpha) have traditionally been used for the determination of subcritical reactivity in low power systems, or in power plants during start-up. We suggested that the prompt neutron decay constant  $\alpha$ , from which the subcritical reactivity can be extracted, can also be unfolded from the continuous signals of fission chambers, based on a newly developed theory of the statistical properties of fission chamber signals [29]. The advantage of the method would be that it is free from the so-called dead time problem, which prevents the application of pulse counting methods at high count rates, and therefore the application domain of the methods would be extended.

In Stage 2016 the basics of the theory were presented, and formulae were derived for the correlation method (Rossi-alpha) in a model without delayed neutrons [24]. In Stage 2018 this theory was extended to be applicable also to the Feynman-alpha method [4]. In both cases it was shown that, under certain conditions, the prompt neutron decay constant can be extracted from the statistics of the fission chamber signals.

To test the applicability of the theory, and to have a proof-of-principle of the method, one needs experimental verification. This was achieved by our collaborating partners at the Budapest University of Technology and Economics (BME, Hungary) and the Kyoto University Institute for Integrated Radiation and Nuclear Science (KURNS, Japan). Hence, in September 2019 a set of measurements has been performed on the Kyoto University Critical Assembly (KUCA) A-core in cooperation with the Institute of Nuclear Techniques of BME (BME NTI). One of the objectives of these measurements was the validation of the current mode noise analysis method for the determination of the subcritical reactivity. For this purpose, the voltage signals as well as time stamp data of detections in multiple detectors were recorded in different critical and subcritical configurations.

This Chapter provides an overview of the measurement configurations and instrumentation, as well as some preliminary results.

## 4.2 Theory

### 4.2.1 Traditional theory

In their traditional forms, the Rossi-alpha and Feynman-alpha methods rely on analysing the counting statistics of neutrons detectors Ref. [30]. Specifically, when applying the Rossi-alpha method, the auto-covariance function  $\text{Cov}(\theta)$  of the number of counts, observed around two time instants  $t_1$  and  $t_2 = t_1 + \theta$ , is determined; in the Feynman-alpha method, the ratio of the variance to the mean of the number of counts, often denoted as  $\text{vtm}(T)$ , observed during a time  $T$ , is obtained.

The theoretical formulae of  $\text{Cov}(\theta)$  and  $\text{vtm}(T)$  are based on a point reactor model Ref. [30]. In this model, the reactor is represented as an infinite homogeneous material, with an extraneous neutron source also distributed in a homogeneous manner within the infinite medium. Neutrons from the source are produced per unit volume with an intensity  $s_0$  and number distribution  $h(k)$ . Each neutron in the system can either be detected with intensity  $\lambda_d$  or lead to a reaction; the reaction might be capture with intensity  $\lambda_c$  or fission with intensity  $\lambda_f$  and with a number distribution of secondary neutrons  $f(k)$ . A detailed calculation of the formulae can be found in e.g. Ref. [30]. Here only the final results are provided the case when the effect of delayed neutrons is neglected:

$$\text{Cov}(\theta) = a e^{-\alpha\theta} + b \quad (4.1)$$

and

$$\text{vtm}(T) = c \left( 1 + \frac{1 - e^{-\alpha T}}{\alpha T} \right). \quad (4.2)$$

Here  $\alpha$  denotes the prompt neutron decay constant, whereas  $a$ ,  $b$  and  $c$  are constant parameters (whose definitions can be found in Ref. [30]).

### 4.2.2 New theory

Starting in 2015, alternative forms of the Rossi- $\alpha$  as well as the Feynman- $\alpha$  methods, based on analysing the continuous voltage signals of a neutron detectors, primarily fission chambers, have been developed. More concretely, in Stage 2016, the new theory of the Rossi- $\alpha$  method has been presented by assuming a simple Poisson external source, i.e.  $h(k) = \delta_{k,1}$  [31, 24]. Recently the model has been extended to compound Poisson sources, and besides updating the theory of the Rossi- $\alpha$  method, the new form of the Feynman- $\alpha$  method based on the analysis of continuous detector signals has been elaborated as well [32]. In each case, the theories are based on a stochastic mathematical model describing the signal  $y(t)$  of the fission chamber [29]. In the model it is assumed that each detection induces a voltage pulse in the detector with some shape  $f(t)$  and a random amplitude  $p$ . The general theory is developed for an arbitrary function, but in the concrete calculations it is assumed that it has the form

$$f(t) = Q \alpha_e^2 t e^{-\alpha_e t}, \quad (4.3)$$

where  $\alpha_e$  is the decay constant of the pulse and  $Q$  is parameter controlling the magnitude of the pulse.



In the new version of the Rossi- $\alpha$  method, the covariance-function of the signal  $y(t)$ , defined as

$$\text{Cov}(\theta) = \lim_{t \rightarrow \infty} \langle y(t) y(t + \theta) \rangle - \langle y(t) \rangle \langle y(t + \theta) \rangle, \quad (4.4)$$

is determined. Assuming a simple Poisson source, and omitting the details of the lengthy theoretical calculations which are found in [24],  $\text{Cov}(\theta)$  can be written as

$$\text{Cov}(\theta) = c e^{-\alpha \theta} + f(\theta) e^{-\alpha_e \theta} \quad \text{for } \theta \geq 0. \quad (4.5)$$

Here the coefficients  $c$  and  $f(\theta)$  are algebraic combinations of the detector parameters as well as parameters of the multiplying medium and the source; their definitions can be found in Ref. [24]. Alternatively, when a compound Poisson source is assumed,  $\text{Cov}(\theta)$  takes the form [32]:

$$\text{Cov}(\theta) = \frac{1}{2} \alpha \langle y \rangle \Phi e^{-\alpha |\theta|} + \frac{1}{2} \alpha_e \langle y \rangle \Psi_1 e^{-\alpha_e |\theta|} + \frac{1}{2} \alpha_e \langle y \rangle \Psi_2 \alpha_e |\theta| e^{-\alpha_e |\theta|}, \quad (4.6)$$

where the coefficients  $\Phi$ ,  $\Psi_1$  and  $\Psi_2$  are again functions of the detector and system parameters and are defined in Ref. [32].

In the continuous signal based equivalent of the Feynman-alpha formula, the quantity

$$\text{vtm}(T) = \frac{\langle [A(T) - \langle A(T) \rangle]^2 \rangle}{\langle A(T) \rangle} \quad (4.7)$$

is determined, which gives the variance-to-mean ratio of  $A(T) = \int_0^T y(t) dt$ , the (random) integral of the detector signal on the interval  $[0, T]$ . After a considerable amount of algebra, one obtains the following expression for  $\text{vtm}(T)$  [32]:

$$\begin{aligned} \text{vtm}(T) = & \Phi \left( 1 - \frac{1 - e^{-\alpha T}}{\alpha T} \right) + \Psi_1 \left( 1 - \frac{1 - e^{-\alpha_e T}}{\alpha_e T} \right) \\ & + \Psi_2 \left( 1 + e^{-\alpha_e T} - 2 \frac{1 - e^{-\alpha_e T}}{\alpha_e T} \right), \end{aligned} \quad (4.8)$$

where the coefficients  $\Phi$ ,  $\Psi_1$  and  $\Psi_2$  are the same as in (4.6).

Clearly, the continuous signal based formulae (4.5), (4.6) and (4.8) show a resemblance to their traditional versions, (4.1) and (4.2), since they contain similar expressions of the prompt neutron decay constant  $\alpha$ . Nevertheless, the new formulae are much more complex since additional terms with the pulse decay constant  $\alpha_e$  also appear. However, from a practical aspect, it must be noted that in thermal reactors  $\alpha \ll \alpha_e$  for every relevant level of subcriticality. As a result, the terms containing  $\alpha_e$  in Equations (4.5), (4.6) and (4.8) decay much faster than those containing  $\alpha$ . Therefore, for sufficiently large value of their arguments,  $\text{Cov}(\theta)$  and  $\text{vtm}(T)$  can be approximated as

$$\text{Cov}(\theta) \approx c e^{-\alpha \theta} \quad (4.9)$$

and

$$\text{vtm}(T) \approx \Phi \left( 1 - \frac{1 - e^{-\alpha T}}{\alpha T} \right). \quad (4.10)$$

This observation allows us to determine the prompt neutron decay constant  $\alpha$  from the measurement by fitting functions of the forms (4.9) and (4.10) to the measured data.

In order to better understand the behaviour of the Rossi- and Feynman- $\alpha$  functions given by Equations (4.6) and (4.8), Fig. 4.1 shows their respective terms along the entire function. The functions were calculated using the same parameters as given in Section 4.3, and correspond to a subcriticality level of  $k_{\text{eff}} = 0.972$ .

One can see, especially for the variance-to-mean, that these curves look rather similar to the case of the traditional formulae with the inclusion of delayed neutrons. There are two plateaus in both cases. In the traditional case, the first plateau corresponds to the searched prompt neutron time constant, hence the fit of the measurements is only made for this first part of the curve. The second plateau, which occurs at much longer measurement times, corresponds to the delayed neutrons. Since the two time constants differ significantly, the effect of the prompt and the delayed neutrons can be separated.

In the present case, which does not include delayed neutrons, it is the second plateau which corresponds to the prompt neutron time constant. The first plateau, at very short times, corresponds to the detector time constant. As the figure illustrates, with realistic data, even here the two plateaus are separated, due to the large difference in the detector time constant and the prompt neutron time constant. Hence, again, a fit to the second part of the curve can be made, without the knowledge of the detector time constant. This is a significant advantage in practical cases.

### 4.3 Simulations

A computational investigation has been performed in order to verify the correctness of formulae presented in Section 4.2 for the alternative versions of the Rossi-alpha and Feynman-alpha methods. For this purpose simulated voltage signals has been produced and analyzed and the results were compared with the theoretical predictions.

The simulated signals were created in two steps. In the first step, the times of neutron detections have been determined in the point reactor model described at the beginning of Section 4.2. Then a pulse with the shape (4.3) has been assigned to each detection and the resulting signal has been sampled with an appropriate time resolution  $\Delta t$ . The parameters of the point reactor model were taken from Ref. [33] and represent a light water reactor. The source- and fission neutron distributions,  $h(k)$  and  $f(k)$ , are shown in Table 4.1; the other parameters are  $s_0 = 10^6 \text{ s}^{-1}$ ,  $\lambda_c = 33196 \text{ s}^{-1}$ ,  $\lambda_d = 335 \text{ s}^{-1}$ . Two signals were simulated using two different values of  $\lambda_f$  in order to represent two different levels of subcriticality. The value of  $\lambda_f$  in these two cases along with the corresponding values of the prompt neutron decay constant  $\alpha$ , the reactivity  $\rho$  and the effective multiplication factor  $k_{\text{eff}}$  are listed in Table 4.2. The parameters of the pulses had values  $Q = 1 \text{ V}$  and  $\alpha_e = 10^6 \text{ s}^{-1}$ ; the corresponding shape is illustrated on Figure 4.2. One can observe that the characteristic length of the pulse is  $10 \mu\text{s}$  which is typical in neutron measurements.

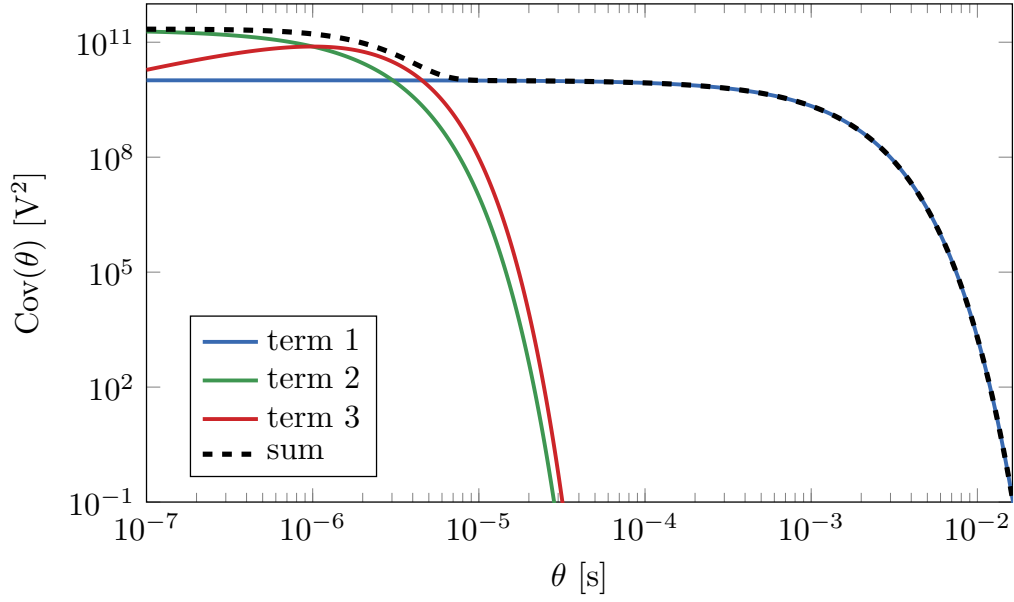
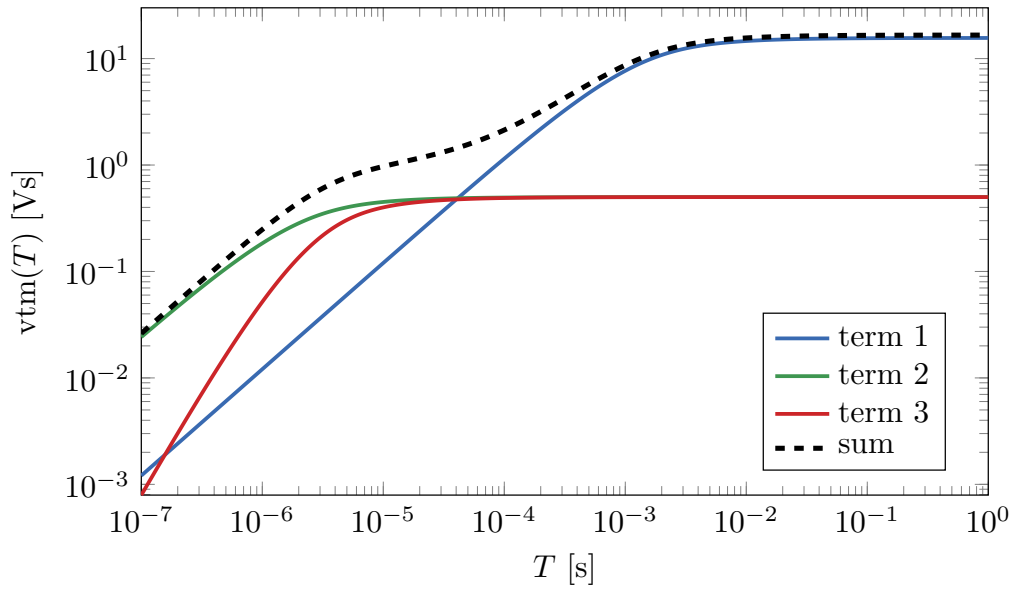
(a) Feynman- $\alpha$  function.(b) Rossi- $\alpha$  function.

Figure 4.1: The respective terms of the Rossi- $\alpha$  function (upper figure) and Feynman- $\alpha$  function (lower figure) given by Equations (4.6) and (4.8).

In order to resolve the pulses properly, a time resolution  $\Delta t = 0.1 \mu\text{s}$  was used to sample the simulated signals.

Table 4.1: The value of the source neutron distribution  $h(k)$  and the fission neutron distribution  $f(k)$ .

#	$h(k)$	$f(k)$
0	0	0
1	0.0378752221	0.1609684328
2	0.2483114582	0.6311237562
3	0.6976884762	0.9279393843
4	1.0890650832	0.6063762312
5	1.019993417	0.1485921955
6	0.5731814862	
7	0.1789428844	
8	0.0239419728	

Table 4.2: The value of the fission reaction intensity  $\lambda_f$  in the two simulation cases and the corresponding values of the prompt neutron decay constant  $\alpha$ , the reactivity  $\rho$  and the effective multiplication factor  $k$ .

case #	$\lambda_f [\text{s}^{-1}]$	$\alpha [\text{s}^{-1}]$	$\rho [-]$	$k_{\text{eff}} [-]$
1	21685	1545.63	-0.029	0.972
2	20713	2979.33	-0.058	0.945

Using the above parameters, two 1000 s long signals have been simulated corresponding to the two levels of subcriticality given in Table 4.2 and a Feynman-alpha as well as a Rossi-alpha analysis has been performed on both. The results are shown in Figure 4.4 along with the theoretical expectations given by Equations (4.6) and (4.8). One can see that most simulated points fit well to the theoretical curve, but a few ones deviate; both are caused by numerical reasons. For the Feynman-alfa case, the deviating point corresponds to a small gate; in such a small gate the numerical estimation of the variance to mean is inaccurate. What regards the the Rossi alpha plot, the deviating points correspond to the largest time lag, which is probably subject to the aliasing effect in the Fast Fourier Transform.

## 4.4 Experiments

### 4.4.1 Core and measurement configurations

The KUCA is a critical assembly, consisting of three different cores, designated as cores A, B and C. These cores are next to each other in the same reactor room, and only one of them can be operated at any time. The core A, on which the present measurements were made, is a modular, solid moderated and reflected type core. The fuel is 93.2% enriched  $^{235}\text{U}$ , embedded in aluminium alloy, in the form of  $5.08 \text{ cm} \times 5.08 \text{ cm} \times 0.1587 \text{ cm}$  metal plates. Assemblies are composed by placing fuel plates horizontally in rectangular aluminium tubes, alongside with polyethylene

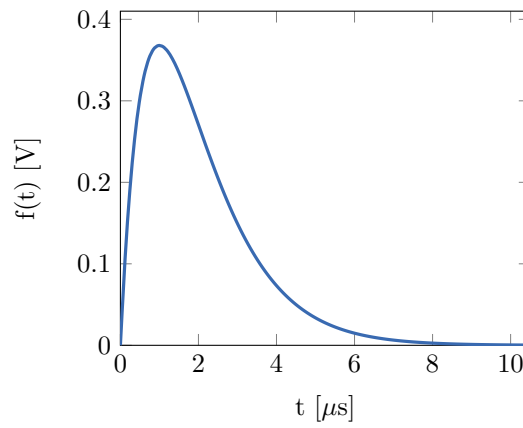


Figure 4.2: The pulse shape used in the simulations.

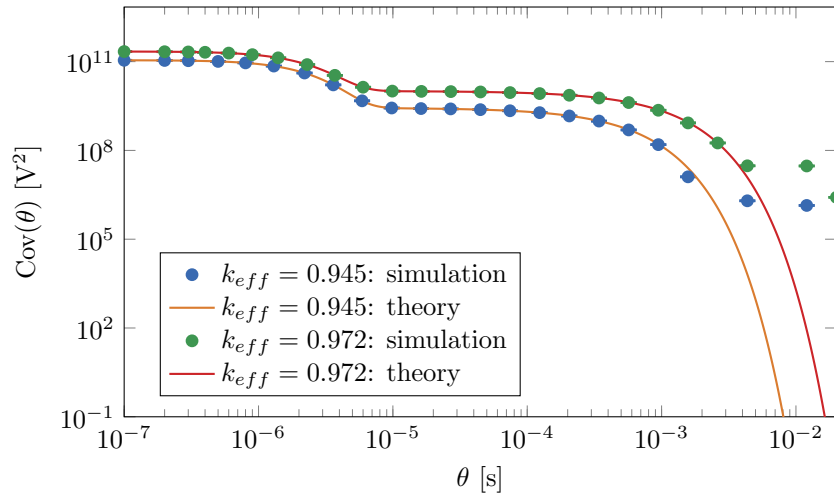


Figure 4.3: The result of a simulated Rossi-alpha measurement at two subcriticality levels.

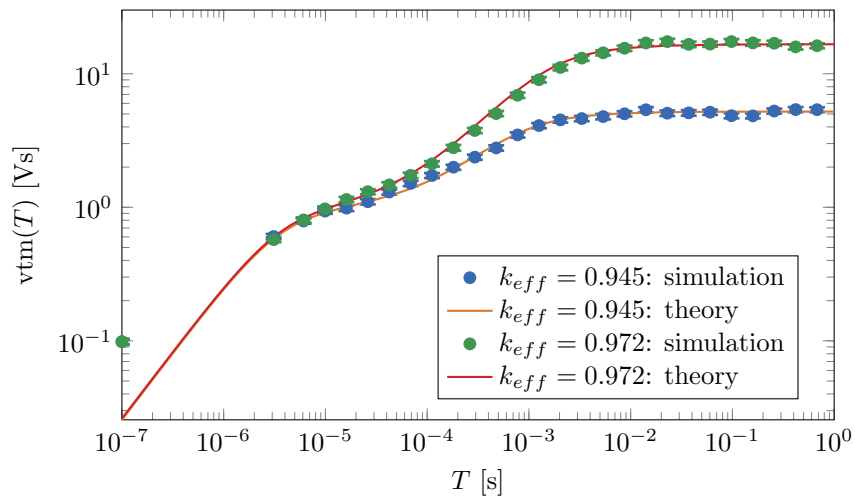


Figure 4.4: The result of a simulated Feynman-alpha measurement at two subcriticality levels.

moderator blocks of similar dimensions. Due to their modular nature, assemblies can be arranged in a great variety of ways to fit the purpose of different experiments. Further details and parameters of the KUCA fuel-, moderator-, etc. assemblies, as well as the facility itself can be found in Ref. [34].

The configuration of the KUCA A-core, as used during the measurements, can be seen on Fig. 4.5, including the positions of four fission chambers (marked as “A”, “B”, “C” and “D”). This core has an excess reactivity of 0.170 %. Measurements were performed at critical state at three different power levels (Tab. 4.3), as well as two different sub-criticality levels (Tab. 4.4). Subcritical configurations were realized by different positioning of the three control rods. The reactivity-worth of each rod, related to this core configuration, is listed in Tab. 4.5.

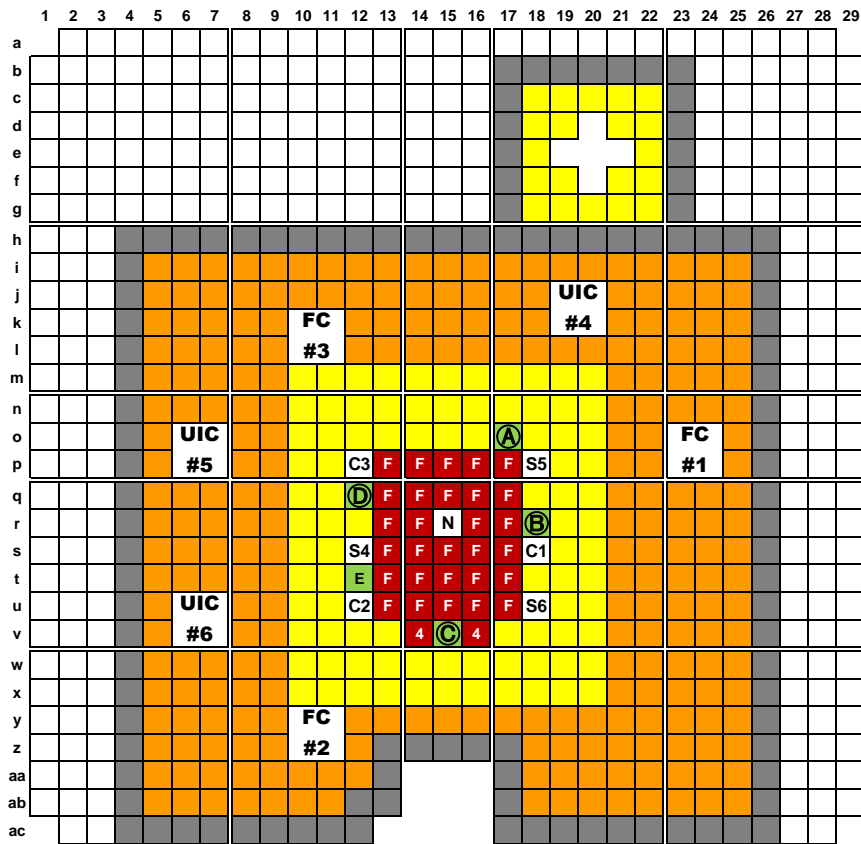


Figure 4.5: Layout of the KUCA A-core during reactivity measurements between 25-27 September 2019. Red squares refer to fuel assemblies; yellow squares refer to polyethylene moderator assemblies; white squares refer to polyethylene reflector assemblies; black squares refer to graphite assemblies. C1, C2 and C3 denote the control rods; S3, S4, and S5 refer to safety rods. N denotes the neutron source. Relevant detector positions are marked by A, B, C and D in green circles.

#### 4.4.2 Instrumentation

During the measurements, two to four Westinghouse WL-8073 type dual-range fission chambers were used in the positions marked on Fig. 4.5, with  $\approx 93\%$  enriched

Table 4.3: Power level of the KUCA A-core during the different critical measurements. Detector labels refer to the fission chambers where voltage signal data was recorded.

measurement name	power [W]	detector labels
CR-1	1.8414e-2	A, D
CR-2	1.8414e-3	A, D
CR-3	5.4648e-1	A, C

Table 4.4: Effective multiplication factor of the KUCA A-core during the different sub-critical measurements, as well as the position of the control rods C1, C2 and C3. Detector labels refer to the fission chambers whose voltage signal data was recorded in a particular measurement.

measurement name	$k_{eff}$	detector labels	C1 position	C2 position	C3 position
SCR-1	0.9906	A, D	inserted	withdrawn	withdrawn
SCR-2	0.978	A, B, C, D	inserted	inserted	inserted

Table 4.5: Reactivity worth of the control rods 'C1', 'C2' and 'C3' in the core configuration used during current set of measurements.

rod	reactivity worth [%]
C1	1.117
C2	0.683
C3	0.588

$^{235}\text{U}$  as fissile material in the form of  $\text{U}_3\text{O}_8$  compound. Individual detectors were placed in the same type of assembly-frame as other components of the KUCA core, with polyethylene padding at the top and bottom of the assemblies.

The signal of each detector was sent to a separate, in-house-built high-frequency pre-amplifier which produced a voltage signal ranging between  $-1$  and  $1$  V (Ref. [35]). The pre-amplifier circuit has a small time constant (compared to the charge collection time of the detector), hence the shapes of the amplified voltage pulses reflect the shapes of the current pulses in the detector. The voltage signals of the four detectors were then digitized by a pair of Red Pitaya STEMLab 125-14 type FPGA-based A/D converters ([36],[37]). Each converter has two analogue inputs and provides a 14 bit vertical resolution as well as 125 MHz maximal sampling frequency (corresponding to a 8 ns maximal resolution in time). The digitized amplitude values were then recorded to binary files on a computer. Fig. 4.6 displays a schematic layout of the instrumentation used in the measurements.

During the measurements, time stamp data were recorded using a NI-myRIO device, employing a software developed in BME NTI Ref. [38]. Data analysis related to this recording method is not included in this report.

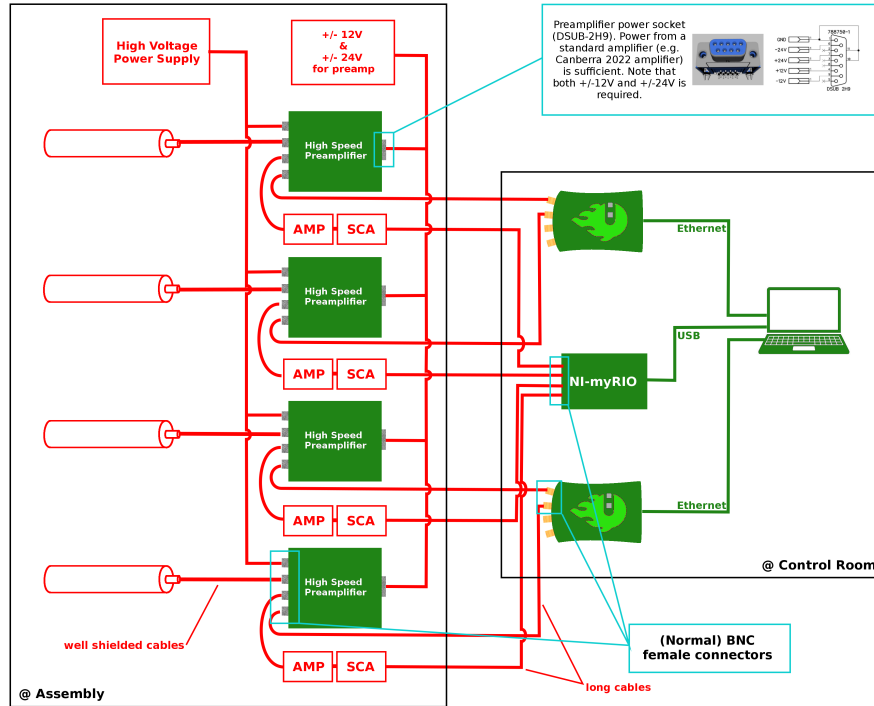


Figure 4.6: Schematic layout of the instrumentation used in the measurements between 25-27. September 2019. Pre-amplifiers were located close to the detectors near the KUCA A-core, while data-recording devices were located in the control room of the facility.

#### 4.4.3 Data analysis

As mentioned previously, our goal was to demonstrate the estimation of the prompt neutron decay constant from the time resolved signals of the detectors. In



order to validate the method, a direct comparison with the pulse counting technique was needed. The only way of doing this was to perform an experiment, in which both methods are applicable. With overlapping pulses, the pulse counting technique fails, due to the presence of the dead time. On the other hand, the analysis of the time-resolved current (voltage) of the fission chambers is valid both for individual (non-overlapping) as well as overlapping pulses.

Therefore, the measurements were performed on configurations where the detection rate was so low that the overlapping of pulses was expected to be insignificant. This condition is fulfilled in subcritical configurations not too close to criticality, considering the intensity of the available neutron source. On the other hand, measurements have also been performed in the critical configuration at several power levels (see in Table 4.3) in order to do the comparison with pulse counting at low count rates and test also the method at higher count rates. Evaluation of these latter measurements is still in progress.

This, in turn, made it possible to calculate the autocovariance function both with the traditional pulse counting approach as well as with the newly proposed method of analyzing the continuous detector signals, in order to assess the performance of the new method. Nevertheless, one trick was necessary to employ in order to make the decay constant values more comparable. Namely, the traditional Rossi- $\alpha$  method was not applied to the time stamp data collected on-line with the use of multi channel analysers; rather, the continuous signals were analyzed off-line by a computer program, and the pulses were counted at an appropriate threshold level. Naturally, one would not use such a laborious method in practical applications; however, our goal here was the validation of the fission chamber signal-based method, for which we wanted to ensure a complete equivalence of the data to be analysed. Measurements have also been carried out in configurations with high detection rates, where the dead-time effect is expected to be more significant in case of the traditional Rossi- $\alpha$  method, but there the purpose was to see the expected differences in the results, based on the fact that the pulse counting method is affected by the dead time, whereas the method based on the continuous signals of fission chambers is not.

As it can be expected, high frequency electronic noise was superimposed on the recorded signals. In order to investigate its effect on the estimated values of the prompt neutron decay constant, smoothed versions of the signals were produced and analyzed off-line as well. The signals were smoothed using a simple moving average algorithm, where each data point was substituted with an unweighted average of 21 consecutive points (lying symmetrically around the original data point). In case of 40 ns and 48 ns time resolutions this resulted in 0.84  $\mu$ s and 1.008  $\mu$ s long averaging windows, which are long enough to suppress most of the high-frequency electronic noise, but sufficiently short not to distort the shape of the pulses very much. On Fig. 4.7 the effect of the smoothing is illustrated on a short signal segment.

We found that suppressing the electronic noise had a negligible effect on the covariance function and the variance-to-mean function obtained from the continuous signals. This is due to the fact that these methods rely on the second order moment of the signals, which inherently suppresses small amplitude uncorrelated signal components such as the electronic noise. On the other hand, the electronic noise pro-

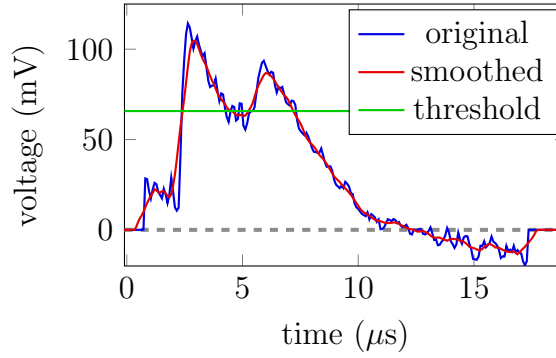


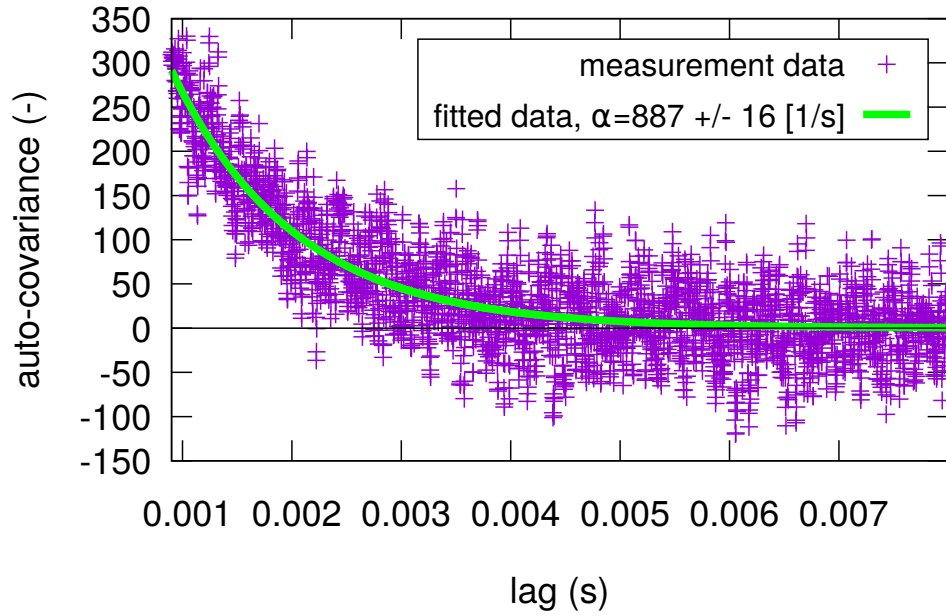
Figure 4.7: Illustration of signal smoothing with a simple moving average algorithm.

duced a considerable number of false counts in the pulse counting approach, which were, however, successfully eliminated by smoothing. This led to the conclusion that the analysis of the time-resolved detector signals was insensitive to the electronic noise; application of the smoothing was required only to get the correct detection rates from pulse counting. Nevertheless, for better visibility, in the remainder of this report, results are presented only for smoothed signals.

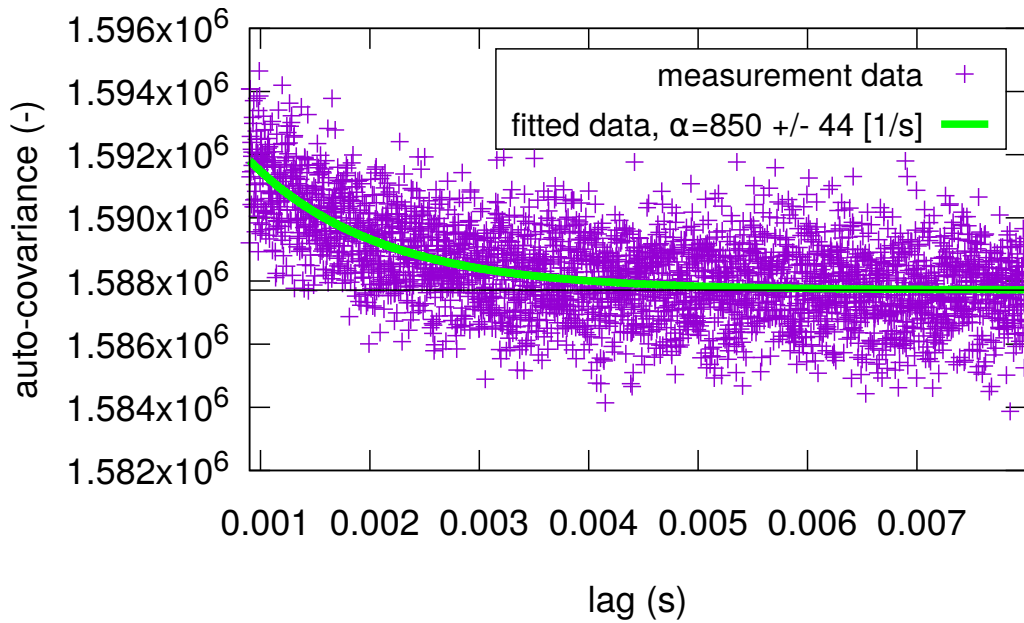
In our evaluated measurements so far, the cases considered consisted of estimation of the Rossi- $\alpha$  with two different approaches for the two subcritical configurations as well as the critical configuration at the lowest power. The time resolution of the data obtained from measurements CR-1, SCR-1 and SCR-2 is 40 ns, 40 ns and 48 ns, respectively. Fig. 4.8 illustrates the results of the data analysis for detector *A* in case of the second subcritical configuration (SCR-2), and Tab. 4.6 lists all estimated  $\alpha$  values obtained from the Rossi- $\alpha$  analysis. Fig. 4.9 displays the relation between the estimated Rossi- $\alpha$  parameters and the reactivity of the system for detectors '*A*' and '*D*'. The results show good agreement between values obtained from the voltage signal analysis and the pulse counting methods in case of the SCR-2 configuration. In case of the SCR-1 configuration, which is closer to the critical state, a more significant difference can be observed between the corresponding  $\alpha$ -values. A similar difference can be observed between the corresponding  $\alpha$ -values of the critical CR-2 configuration. This is suspected to be caused by the higher count rates and dead-time effect in the detectors. Further analysis is required regarding this matter.

Feynman- $\alpha$  evaluations have also been performed both with the new approach using the voltage signals as well as with the traditional way using time stamp data obtained from the recorded voltage signals. The results are shown on Fig. 4.11 for the SCR-2 configuration; similar results were obtained for the other two configurations as well. It is seen that the estimated functions have an unexpected distortion in the form of a peak appearing around  $10^{-4}$  s which, in fact, made it impossible to fit the theoretical function and obtain the prompt decay constant. The exact cause of the peak is yet unknown and is still under investigation, but it is probably caused by the limited bandwidth of the signal recording device and might be in connection with the detector pulse shape.

To bypass this issue, an alternative approach has been followed in which the covariance-to-mean function (to which no theory is available yet) of the signals



(a) Auto-covariance function of the voltage signal data.



(b) Traditional auto-covariance of the time stamp data.

Figure 4.8: Results of the two different approaches for Rossi- $\alpha$  evaluation for detector *A* in case of the SCR-2 configuration.

Table 4.6: Estimated  $\alpha$  values from the Rossi-evaluation for the low-power critical as well as the subcritical configurations.

Configuration	Detector pair	$\alpha_{signal\ analysis}$ [1/s]	$\alpha_{pulse\ analysis}$ [1/s]
CR-2	A-A	$274.4 \pm 1.1$	$241.6 \pm 2.1$
	D-D	$272.1 \pm 1.1$	$238.2 \pm 2.8$
SCR-1	A-A	$664 \pm 11$	$579 \pm 29$
	D-D	$648 \pm 10$	$525 \pm 26$
SCR-2	A-A	$887 \pm 16$	$850 \pm 44$
	B-B	$814 \pm 20$	$777 \pm 60$
	C-C	$961 \pm 15$	$935 \pm 36$
	D-D	$911 \pm 25$	$1011 \pm 84$
	A-B	$1000 \pm 18$	$927 \pm 42$
	C-D	$1010 \pm 18$	$945 \pm 39$

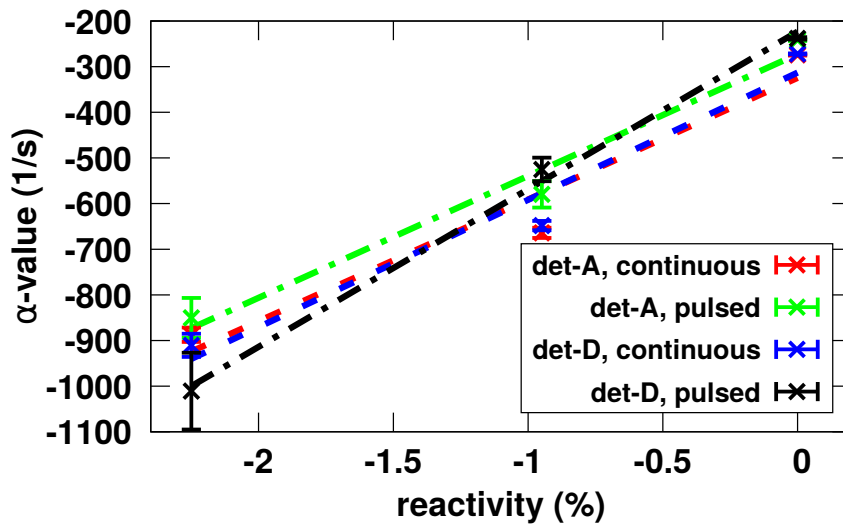


Figure 4.9: Relation between the estimated  $\alpha$ -parameters and the reactivity of the system for different detectors

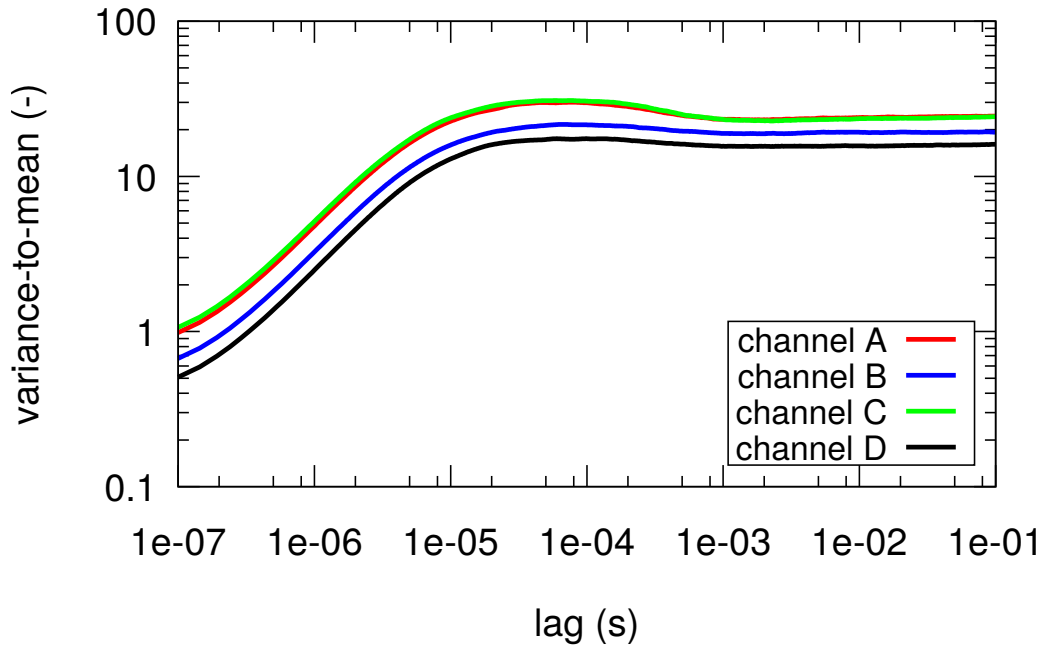
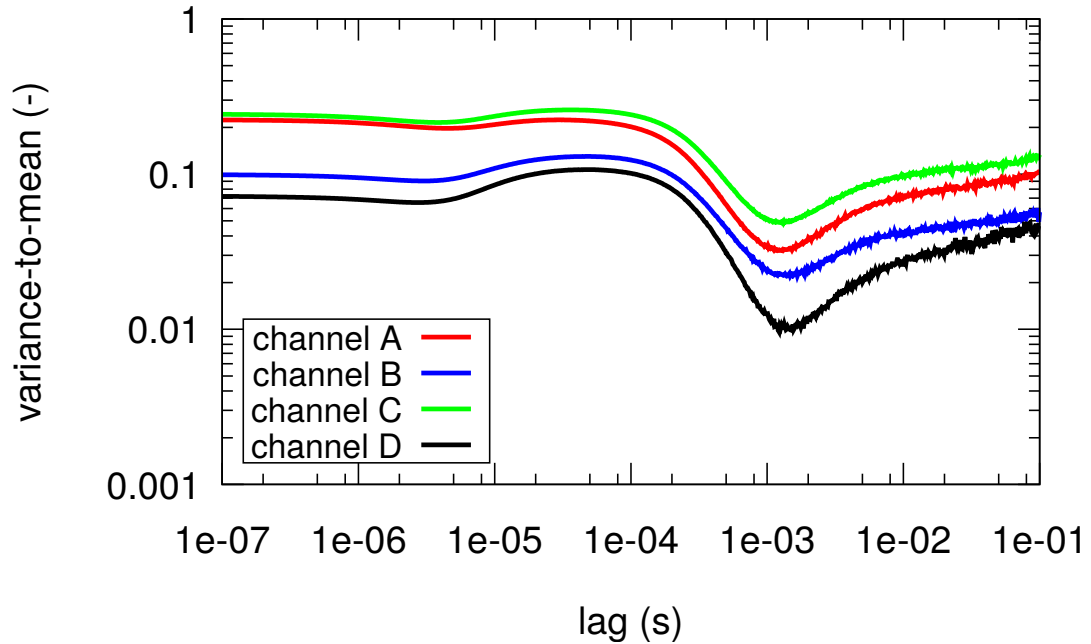
(a) Feynman- $\alpha$  evaluation of the voltage signal data.(b) Feynman- $\alpha$  evaluation of the time stamp data.

Figure 4.10: Results of the two different approaches for Feynman- $\alpha$  evaluation for detector A in case of the SCR-2 configuration.

of two detectors has been estimated. This covariance-to-mean function has been calculated for the detector pairs A–B and C–D in the SCR-2 configuration, but the calculation could not be done for the other configurations, since the signals were not recorded in a synchronized way in these configurations. The estimated covariance-to-mean function for the pair A–B is shown on Fig. 4.11, where apparently no peak is present. The  $\alpha$  values obtained for both pairs A–B and C–D in the SCR-2 subcritical configuration are listed in Tab. 4.7. These values appear to be in relatively good agreement with the corresponding  $\alpha$ -parameters from the Rossi- $\alpha$  method.

Table 4.7: Estimated  $\alpha$  values from the Covariance-to-Mean evaluation for the SCR-2 configuration.

Configuration	Detector pair	$\alpha_{signal\ analysis}$ [1/s]	$\alpha_{pulse\ analysis}$ [1/s]
SCR-2	A-B	$939.3 \pm 7.5$	$953.5 \pm 4.0$
	C-D	$926.3 \pm 7.8$	$930.4 \pm 4.0$

#### 4.5 Conclusions and further plans

The preliminary results reported here suggest that the value of the prompt neutron decay constant  $\alpha$  can be reconstructed from the time-resolved signals of fission chambers. The measurement made it possible to estimate the Rossi- $\alpha$  also with the traditional pulse counting method, and a good agreement between the two methods was found. Covariance-to-mean evaluations have also been performed with promising results. On the other hand, further work is needed to optimize the evaluation methods and to interpret the results.

The work in this field will continue on several lines, and might be included in later Stages. The analysis and interpretation of the already existing data from the measurements, made in critical conditions at KUCA and at the BME Training Reactor, will be completed. Further, the data analysis in order to apply the Feynman- $\alpha$  method with time resolved fission chamber signals will also be made. Finally, new measurements are planned both at the BME Training Reactor and at the KUCA reactor on other configurations, to increase the extent of the validation procedure. One interesting aspect would be to investigate the applicability limits of the fission chamber-based analysis method for higher core power (neutron flux) leading to fully overlapping detector pulses, when the pulse counting method is definitely not applicable. Such an experimental scenario will be possible to investigate up to 100 kW power at the BME Training Reactor.

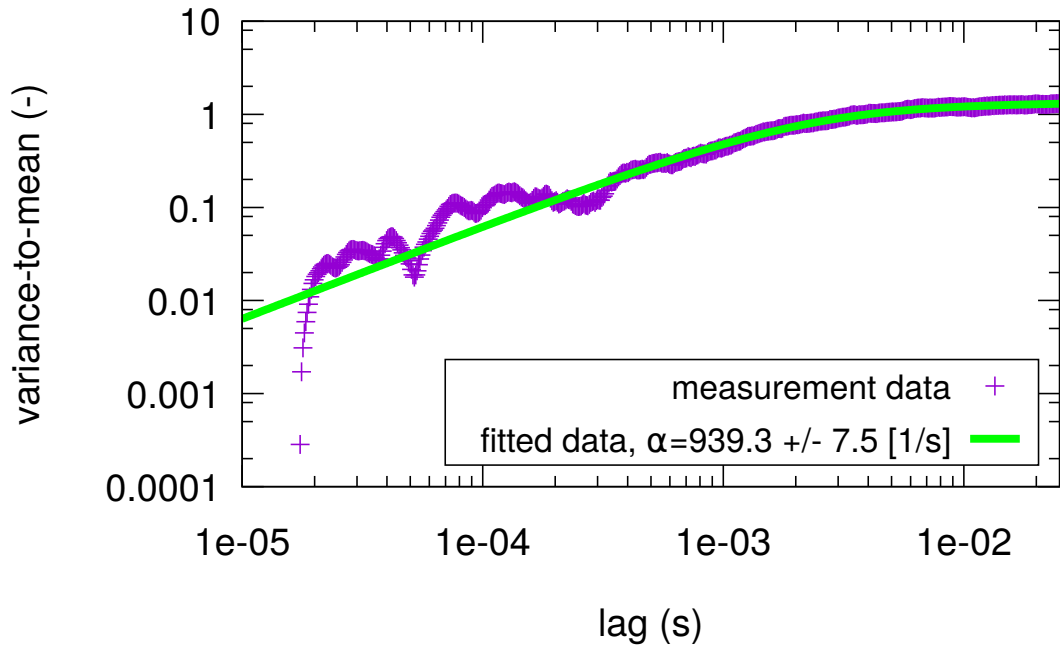
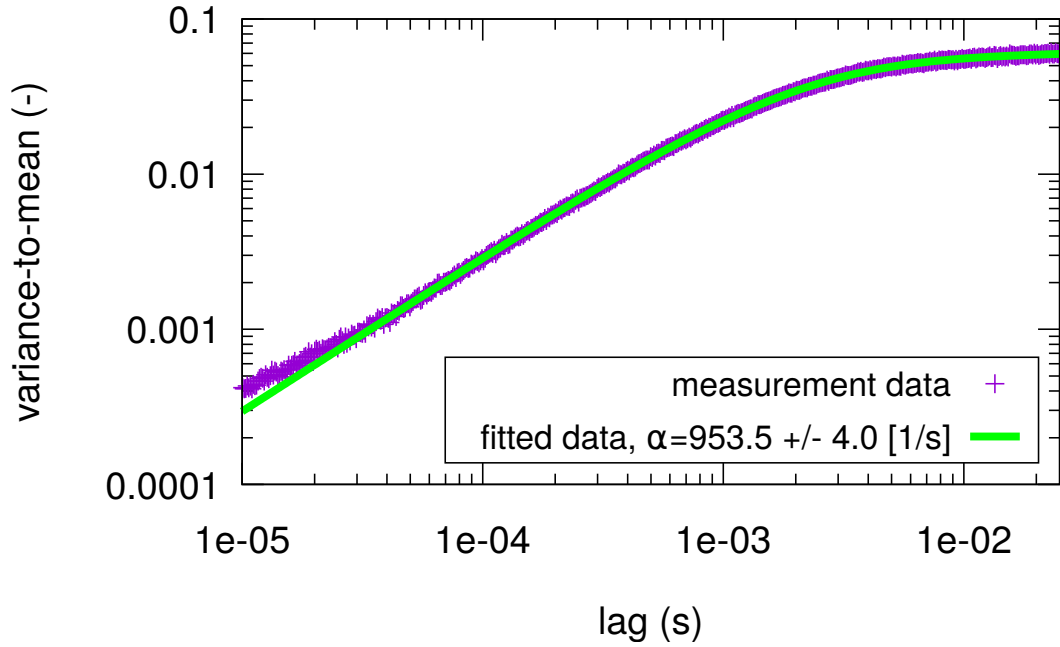
(a) Feynman- $\alpha$  evaluation of the voltage signal data.(b) Feynman- $\alpha$  evaluation of the time stamp data.

Figure 4.11: Results of the two different approaches for Feynman- $\alpha$  evaluation for detector pairs  $A-B$  in case of the SCR-2 configuration.

## 5. FURTHER DEVELOPMENT OF A NEW METHOD TO DETERMINE THE AXIAL VELOCITY PROFILE OF THE VOID IN THE CORE OF A BWR BY USING FOUR PERMANENT IN-CORE LPRMS AND A TIP DETECTOR

### 5.1 Introduction

As already described in the previous Stage, the question of experimental determination of the local void fraction in BWRs has been revived some years ago. The noise community has long been interested in how to extract the local void fraction from in-core neutron noise measurements [39, 40], but no satisfying solution has been found yet.

This question has been taken up also in Stages 13 and 14 of this project [13, 21]. It was concluded that one promising possibility was to determine the local void fraction from the upper break frequency of the auto-spectra (APSD) of the individual LPRM detectors. In essence, the break frequency  $f_{br}$  of the APSD of the neutron noise induced by the passage of the fluctuating two-phase flow structure through the so-called detector field of view  $\lambda(z)$  is given as

$$f_{br} = v(z) \lambda(z) \quad (5.1)$$

where  $z$  indicates the axial elevation in the core. Here,  $\lambda(z)$  is an exponent, describing the so-called detector field-of-view (the spatial decay of the local component of the neutron noise), which can be calculated by reactor physics methods for any given void fraction. Having access to the break frequency and the local void velocity from measurements, the void fraction can be unfolded from the calculated correlation between the void fraction and the range of the local component.

This method thus requires that the local void velocity is known at the individual detector positions. However, in in-core noise measurements only the transit times of the void between two axially displaced neutron detectors can be obtained. Therefore there is a need of a method to reconstruct the local void velocities from the measured transit times.

Determination of the local void velocities is possible if the axial velocity profile is reconstructed from the measured transit times. This in turn requires an assumption on the analytical form of the velocity profile, depending only on a few parameters, which then can be determined from the transit times. The main stumbling block in this procedure is that the simplest physically realistic velocity profile is a third order polynomial, containing 4 parameters, whereas the four fixed in-core LPRMs yield only 3 transit times. The attempt of circumventing this problem by using a TIP detector as a fifth detector, yielding one more transit time, was unsuccessful, as described in Stage 2012-14 [22].

Therefore, in the previous Stage a different strategy was suggested and investigated. We realised that there was no need for a fourth transit time to determine the four parameters of velocity profile, either a polynomial or some other form, if



the axial point of the onset of the boiling is known. The onset point of the boiling can be determined with a TIP detector alone, from the amplitude of its root mean square noise (RMS) or its APSD, or, alternatively, from the coherence between the TIP and the lowermost LPRM, if these are determined as a function of the axial position of the TIP. At the onset of the boiling the void velocity can be assumed to be equal to the inlet coolant velocity, which is known. Thus, knowledge of these two quantities reduces therefore the number of unknowns of the axial velocity profile to be determined from four to three.

Second, there exist non-linear functions with an inflection point, which represent an even higher order non-linearity than a third order polynomial, but which nevertheless can be parametrised with only three parameters instead of four. Examples are certain trigonometric or sigmoid functions. For simplicity these profile types will be referred to as ‘trigonometric’. In this case not even the onset point of the boiling needs to be known; determination of the void profile is then possible based on solely of the three measured transit times with the standard instrumentation, without the need for using a TIP detector at all.

The principles, as well as the applicability of both types of velocity profile forms (trigonometric and polynomial) were investigated in conceptual studies in Stage 2019 [25]. Various types of velocity profiles were assumed, both trigonometric and polynomial, as the “true” profiles as a starting point. From the true profiles, the three transit times between the four detectors were calculated, and then the inversion procedure applied and its accuracy was investigated. When using the polynomial form with 4 parameters, we needed to make some assumptions, such as the position of the onset of the boiling point. The sensitivity of the results on the accuracy of these assumptions was investigated in model calculations. The sensitivity of the reconstruction on the correct assumption on the form of the profile (i.e. starting with a trigonometric as “true” and performing the reconstruction with the polynomial form, and vice versa), as well as taking a true polynomial profile with a given onset point of the boiling and making the reconstruction with a different onset point as an incorrect guess, was also investigated. Finally, an attempt was made to reconstruct the (unknown) velocities at the detector positions from a measurement at Ringhals-1, both with the trigonometric and the polynomial velocity forms.

As reported in the previous Stage, the results of the evaluation of the suggested methods were rather promising. The results were published in the journal *Progress in Nuclear Energy* [41]. Our intention for the present Stage was to test the method on several more measurements. In particular, we planned to use an extensive data base, represented by the noise measurements made in all Swedish power reactors by GSE Power Systems. We came to know from an internal report of SKI [42], the predecessor of SSM, that during a project, supported by SKI, measured noise data of a large number of measurements, taken by GSE Power Systems in several Swedish reactors, mostly BWRs, were transferred to CD, in order to save these data for the possibility of later analysis.

Unfortunately, it turned out that those CDs could not be found at SSM. Therefore, in this Stage, we chose to report on the further developments and investigations of the suggested method. Namely, during the review process of the publication Ref.

[41], the three reviewers questioned some of assumptions of the method, and required clarifications, as well as confirmation of their validity. Addressing these questions and comments required a significant amount of effort, but it was very useful because it widened our own understanding. Hence, in this chapter these improvements and further developments/investigations will be reported.

## 5.2 Summary of previous work

Before turning to the new developments, a very brief summary of the findings of the previous Stage will be given, for easy reference. These contain a review of the qualitative forms of the flow profiles, the analytical forms used to emulate such profiles, and the essence of the unfolding procedure.

### 5.2.1 Qualitative flow profiles

In order to choose a suitable analytical form for the velocity profile, we took an inventory of some characteristic flow velocity profiles. Since no experimental data are available, we had to consider such profiles calculated by two different system codes, TRACE [43, 44, 45] and RAMONA [46, 47].

Fig. 5.1 shows a few profiles from calculations with TRACE, where account was taken for the fact that the boiling does not start at the inlet, rather at a higher elevation (courtesy of Mathieu Hursin, EPFL/PSI, Switzerland). On Fig 5.2, calculations with RAMONA of the steam velocity in Ringhals 1 in a few selected channels are shown. In this latter, the discontinuity at around the core height of 2.5 m is due to the fact that the fuel assemblies, in which the calculations were made, contain partial length fuel rods. At this elevation, there is an abrupt change in the void/fuel ratio, hence the sudden change in the void velocity. The effects of partial length fuel rods were not taken into account in the analysis presented in the previous Stage; the RAMONA profiles were shown only for a qualitative illustration of flow velocity profiles in BWRs. Application of the method developed and investigated in the previous Stage will constitute one of the novel items in this Chapter.

Another hint on the possible profiles arises from results of simulations of a bubbly flow in a heated channel, which were performed by an in-house Monte Carlo code. This code was developed earlier in Stage 14 [21], and used in previous work. Some profiles, resulting from these simulations, are shown in Fig. 5.3.

A common feature of these profiles is that the velocity increases monotonically in the channel from the inlet, first at least quadratically, then the increase slows down, either leading to an inflection point, or to a linear increase towards the core exit. These type of profiles were approximated by two different functional forms.

### 5.2.2 Possible analytical forms

As described in the previous Stage, two forms were investigated. One of these, called the polynomial form, is based on the third order polynomial also used in previous work, but now written in a slightly different form as

$$v(z) = \Delta(z - h) \left[ v_0 + b(z - h) + c(z - h)^2 + d(z - h)^3 \right] \quad (5.2)$$

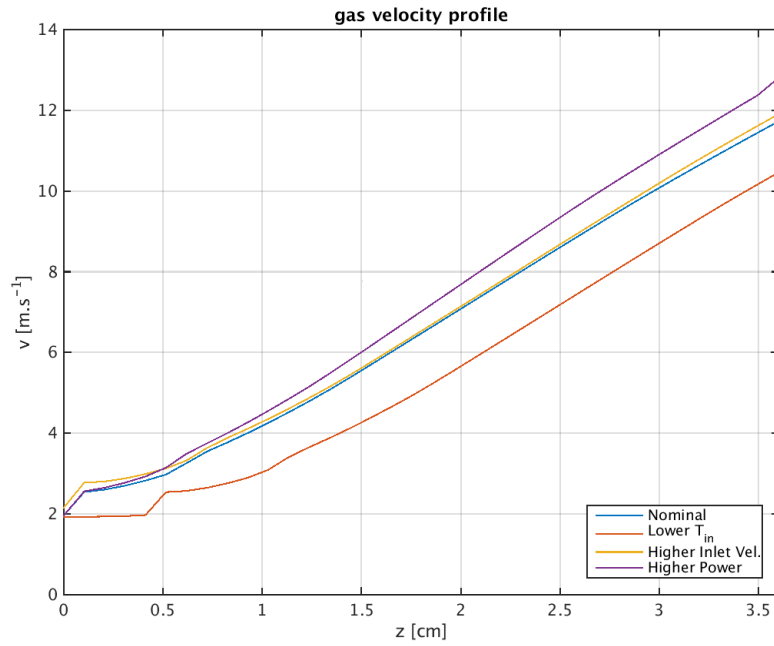


Figure 5.1: Void velocity profiles simulated by TRACE

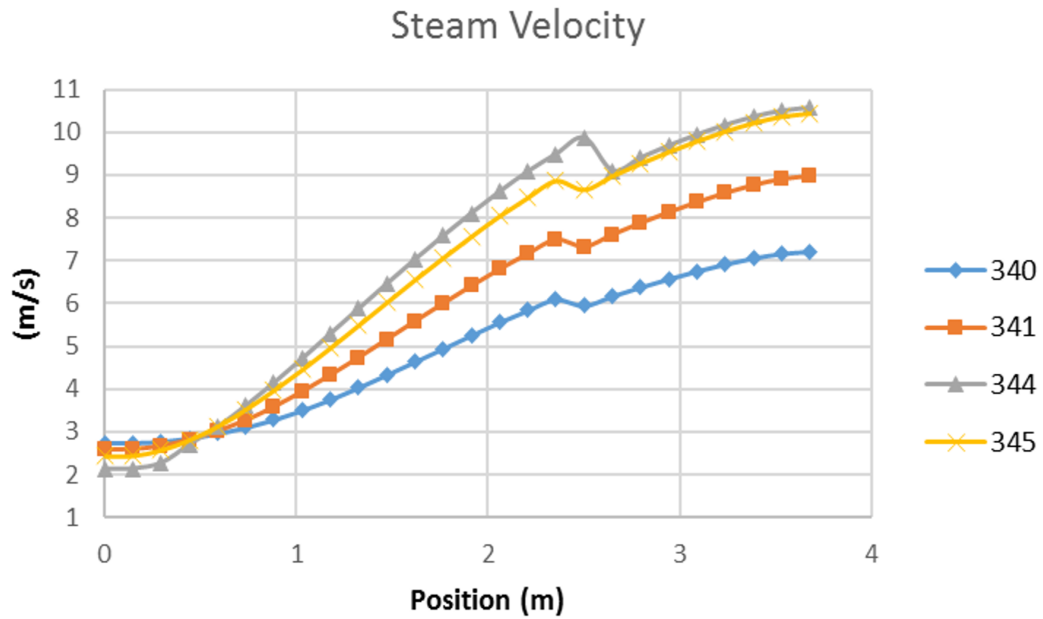


Figure 5.2: Void velocity profiles simulated by RAMONA in channels 340, 341, 344 and 345

where  $h$  is the onset point of the boiling,  $\Delta(z)$  is the unit step function, and  $v_0$  is the inlet coolant velocity. In this form, the profile contains not only four, but five unknowns. However, as described in the Introduction,  $v_0$  can be assumed to be equal to the inlet coolant velocity and hence known, and the boiling onset point  $h$  can be

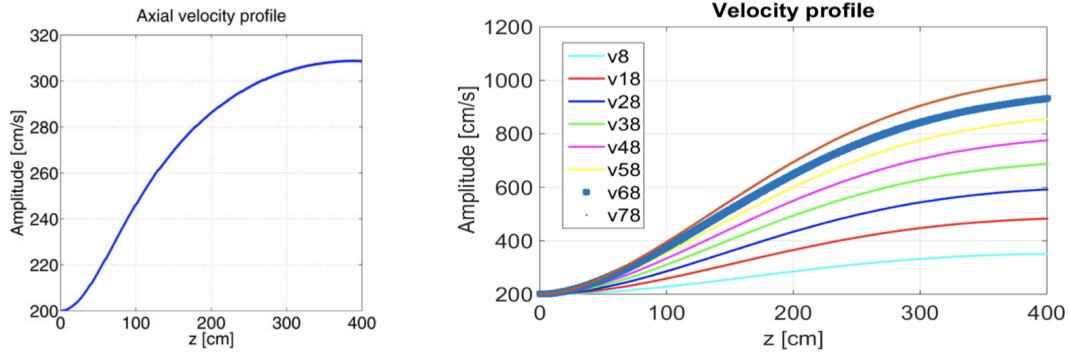


Figure 5.3: Void velocity profiles simulated by a Monte-Carlo model of bubbly two-phase flow

determined from TIP measurements. In that case there are only three unknowns, which can be determined from the three transit times. Even if the boiling onset point is not known, it is not difficult to make a qualified guess, such as lying at, or close to, halfway between the core inlet and the lowermost detector. It was investigated in the previous Stage, that using such a guess still leads to quite accurate results even if the boiling onset point is guessed incorrectly.

The second type of void velocity profiles arises from the recognition that there exist non-linear functions other than a third-order polynomial which have an inflection point, and which contain only three free adjustable parameters. These include trigonometric functions, such as  $a \cdot \text{atan}(b(z - c))$ , where  $a, b$  and  $c$  are constants, or the co-called “sigmoid” function, used in the training of ANNs. We called such profiles as “trigonometric”. For such profiles the onset point of the boiling does not need to be known. Of course, the price one has to pay for the convenience of only needing to fit three parameters instead of four is that the structure of the profile is more “rigid” than that of the more general polynomial form, hence its flexibility of modelling and reconstructing a wide range of velocity profiles is reduced as compared to the polynomial fitting.

Using some very simple considerations connecting a cosine-shaped flux profile with heat generation and void creation, described in the previous report [25], we arrived at the simple form

$$v(z) = \Delta(z - h) \left\{ a_1 + c_1 \sin \left[ B \left( z - \frac{H}{2} \right) \right] \right\}. \quad (5.3)$$

This form contains the three unknowns  $a_1, c_1$  and  $B$ ;  $H$  is the height of the core, which is known. Apart from having only three parameters, this form has the further advantage that, unlike the polynomial velocity profile, the  $1/v(z)$  of Eq. (5.3) can be integrated analytically. In other words, the transit time  $t_i$  between detectors  $i$  and  $i + 1$ ,

$$t_i(a_1, c_1, B) = \int_{z_i}^{z_{i+1}} \frac{dz}{v(z)} \quad (5.4)$$

is an analytic function of the parameters  $a_1, c_1$  and  $B$ . However, it turned out that this did not constitute any advantages, as described in the next Section.

### 5.2.3 The unfolding procedure

First we tried to use the velocity profile given in Eq. (5.3). Our expectation was that in possession of the analytical expressions for  $t_i(a_1, c_1, B)$ ,  $i = 1, 2, 3$ , and having access to given values of the three measured transit times  $\tau_i$ ,  $i = 1, 2, 3$ , the unknown parameters  $a_1, c_1, B$  can be determined as the roots of the non-linear equation system

$$t_i(a_1, c_1, B) = \tau_i, \quad i = 1, 2, 3 \quad (5.5)$$

For the numerical solution of this non-linear equation system, the numerical root finding routine `NSolve` of Mathematica 12.0.0.0 was used [48]. However, the root finding did not converge, even if quite accurate starting values were specified. It appears that the `NSolve` routine is primarily designed for treating polynomial equations, rather than transcendental ones.

Therefore, another path was followed to unfold the parameters of the void profile from the transit times. Instead of using `Nsolve`, a kind of fitting procedure was selected by searching for the minimum of the penalty function

$$\sum_i^3 [t_i(a_1, c_1, B) - \tau_i]^2 \quad (5.6)$$

as functions of  $a_1, c_1$  and  $B$ . First the `FindMinimum` routine of Mathematica was used. This procedure worked well and was able to reproduce the input parameters of the velocity profile. Initially the analytical form was used for the  $t_i(a_1, c_1, B)$ . However, it turned out that defining these latter as numerical integrals with free parameters  $a_1, c_1, B$  worked much faster and with better precision, showing also that for the unfolding, it is not necessary that the transit times are given in an analytical form. Consequently, the modified polynomial form of  $v(z)$  in Eq. (5.2) can also be used, despite that  $v^{-1}(z)$  is not integrable analytically. In this latter case, the transit times  $t_i(b, c, d)$  are numerically calculated functions of the parameters  $b, c$  and  $d$ , as defined in Eq. (5.2).

The unfolding procedure was tested using both the trigonometric velocity profile given in (5.3), as well as with the polynomial profile of Eq. (5.2). These extended numerical tests were made by Matlab. The minimum of the penalty function (5.6) was found by own MATLAB scripts. In addition, unlike for the case with Mathematica, for the trigonometrical profile, using the parameter values obtained from the minimisation process as starting values to the routine `fsolve` helped to successfully solve also the nonlinear system of equations (5.5), to get the velocity profile.

## 5.3 Improvements and further developments

In this Section improvements and further developments of the method, as well as some further investigations and clarifications of the assumption used will be described. These came about during the revision process of the publication [41].

### 5.3.1 Void velocity vs perturbation velocity

Some of the reviewers questioned whether the experimentally determined transit time from the cross correlation of neutron detector signals really corresponds to

the void velocity profile and not to some average mass flow profile. This question is motivated by the fact that the two phase flow changes axially from the inlet to outlet from bubbly to slug, churn-turbulent and annular flow, and the void fraction also rises from zero at the inlet to about 70% at the outlet. These are important questions, which need to be addressed.

Therefore, to clarify the situation, we elaborated on the usage of the word “void velocity”, as follows. Indeed, in the neutron noise community it is tacitly assumed that the transit time deduced from the neutron noise measurements corresponds to the transit time of the void (steam). However, the neutron noise is induced by the temporal fluctuations of the reactor material around its mean value. In a binary or dichotomic medium (fluid-void), it is represented by the fluctuations of the minority component. At low void fraction, such as a sparse bubbly flow, the neutron noise is indeed generated by the fluctuations represented by the void, and hence the transit time obtained by the noise measurement corresponds to the transit time of the void. At high void fractions, the fluid becomes the minority component, hence the neutron noise is generated by the water droplets/mist, and/or the propagating surface waves of the water in an annular flow regime. Therefore, in the upper part of the core, i.e. between the uppermost two detectors, it is more correct to talk about the transit time of the *perturbation* instead.

Consequently, one could question whether the velocities determined from the in-core neutron noise are indeed suitable for achieving the final goal, namely the determination of the local void content from noise measurements. The answer is affirmative, due to the fact that for this latter goal, we suggest to use the break frequency method. It is a great advantage of this method that the break frequency, being itself a noise quantity, depends on the transit time of the *perturbation*, and on the detector field of view. Hence, it is completely independent of whether the fluctuations of the void or the fluid generate the detected neutron noise. This means that the range  $\lambda$  of the local component will be determined correctly by using the experimentally determined break frequency and void (perturbation) velocity. Hence, the break frequency method will supply the void fraction correctly, since this latter is extracted from the dependence of  $\lambda$  on the void fraction. Because of this fact, and because full realistic calculations of the detector field of view are underway [49], the break frequency method appears suitable and effective for determining the void fraction in operating BWRs.

The above also means that it would be more correct to refer to “perturbation velocity” rather than “void velocity” in this method. However, this would be cumbersome and even confusing, and for practical reasons, we will use the terminology “void velocity” or “steam velocity” throughout, on the understanding that in the upper part of the core, it actually means the velocity of the perturbation, which may differ from that of the void (steam).

### 5.3.2 Accuracy and consistency of the determination of the transit times

There were requests on estimating the accuracy of the experimental determination of the transit times - even the need of a sensitivity and uncertainty analysis was put forward. This latter though fell outside the scope of the paper. However,

one reviewer suggested a consistency analysis, called the “transit time conservation”. This question meant checking whether the sum of the transit times  $\tau_{1,2} + \tau_{2,3}$  was equal to the transit time  $\tau_{1,3}$ , the latter being extracted from the cross-correlation between detectors 1 and 3, or whether one had  $\tau_{1,2} + \tau_{2,3} + \tau_{3,4} = \tau_{1,4}$  etc.

This is an interesting question which, to the best of our knowledge, has not been investigated before. It does not have a direct practical use, since the transit times are additive, and therefore  $\tau_{1,3}$  does not carry any new and independent information in addition to  $\tau_{1,2}$  and  $\tau_{2,3}$ . Moreover, the determination of the transit times is most accurate between the detectors lying closest to each other (where one has the largest coherence), which is another reason why the transit times between non-adjacent detectors were never investigated. Hence such an investigation is only useful to check the consistency of the measurements through the “transit time conservation”.

Nevertheless, the question is interesting for itself, hence we made an investigation of the consistency of the transit times. Since determination of the transit times is made on the slope of the linear phase of the cross-correlation, the best results are obtained with measurements in which a clear linear slope of the phase could be observed over a broad frequency region. Since in the Ringhals measurements which were used in the previous Stages, the phase behaviour was not always optimal, for purposes of demonstration we selected some classical measurements. These were performed by the Studsvik Noise Group, the predecessor of GSE System Engineering, in the now closed Barsebäck-1. The original purpose of those measurements was to diagnose detector tube vibrations through the distortion of the linear phase between detectors in the same instrument tube [5]. In the cases when there were no instrument tube vibrations, the phase of the CPSD showed a nice linear dependence on frequency up to about 10 Hz. Because of their good quality phase curves, these measurements were cited frequently in the literature [5, 50].

However, in all previous works, only the phases of the CPSDs between two adjacent detectors were calculated, hence the consistency of the transit times was not investigated. Luckily, those original measurement data are still available in Chalmers, and thus it was possible to perform a study of the consistency of the transit times, by calculating the CPSDs and plotting their phases also for the non-adjacent detectors.

Figs 5.4 and 5.5 show the phase of the CPSD for all 6 possible combinations of the four LPRMs in the instrument tube 18, which was found to be completely free from vibrations. In the top legend of these figures, the traditional numbering convention is used for the detectors, in that LPRM1 is the top and LPRM4 is the bottom detector. Hence the top figure corresponds to the phase between the two uppermost detectors; the middle figure to the phase between the two innermost detectors, and the bottom curve to the two lowermost detectors. The red straight line is fitted to the segment of the phase curve which shows visually a nice linear behaviour. The transit time  $\tau$  was determined from the slope of the fitted curve as

$$\tau = \frac{\varphi(f)}{2\pi f} \quad (5.7)$$

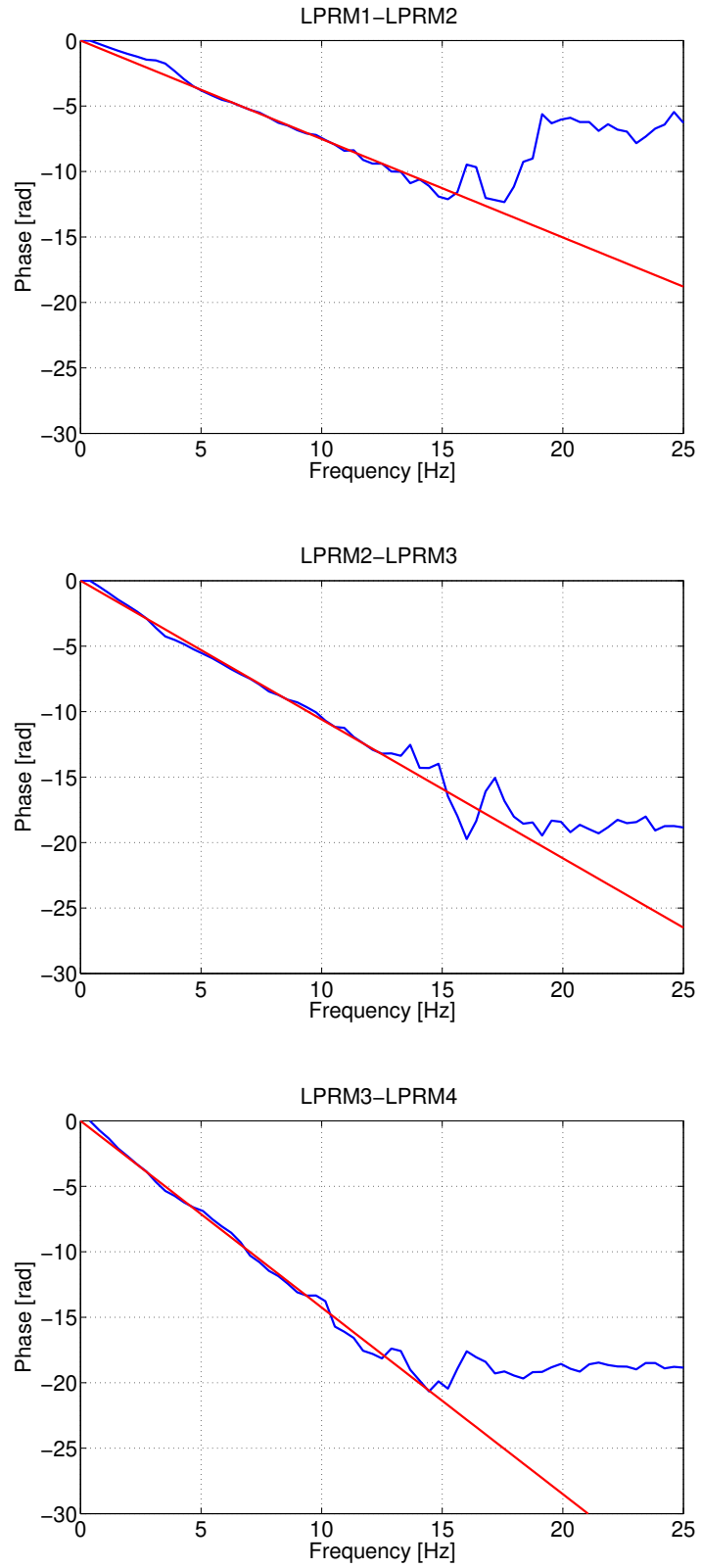


Figure 5.4: Phase of the CPSD for the detector pairs LPRM1-LPRM2 (top), LPRM2-LPRM3 (middle) and LPRM3-LPRM4 (bottom).



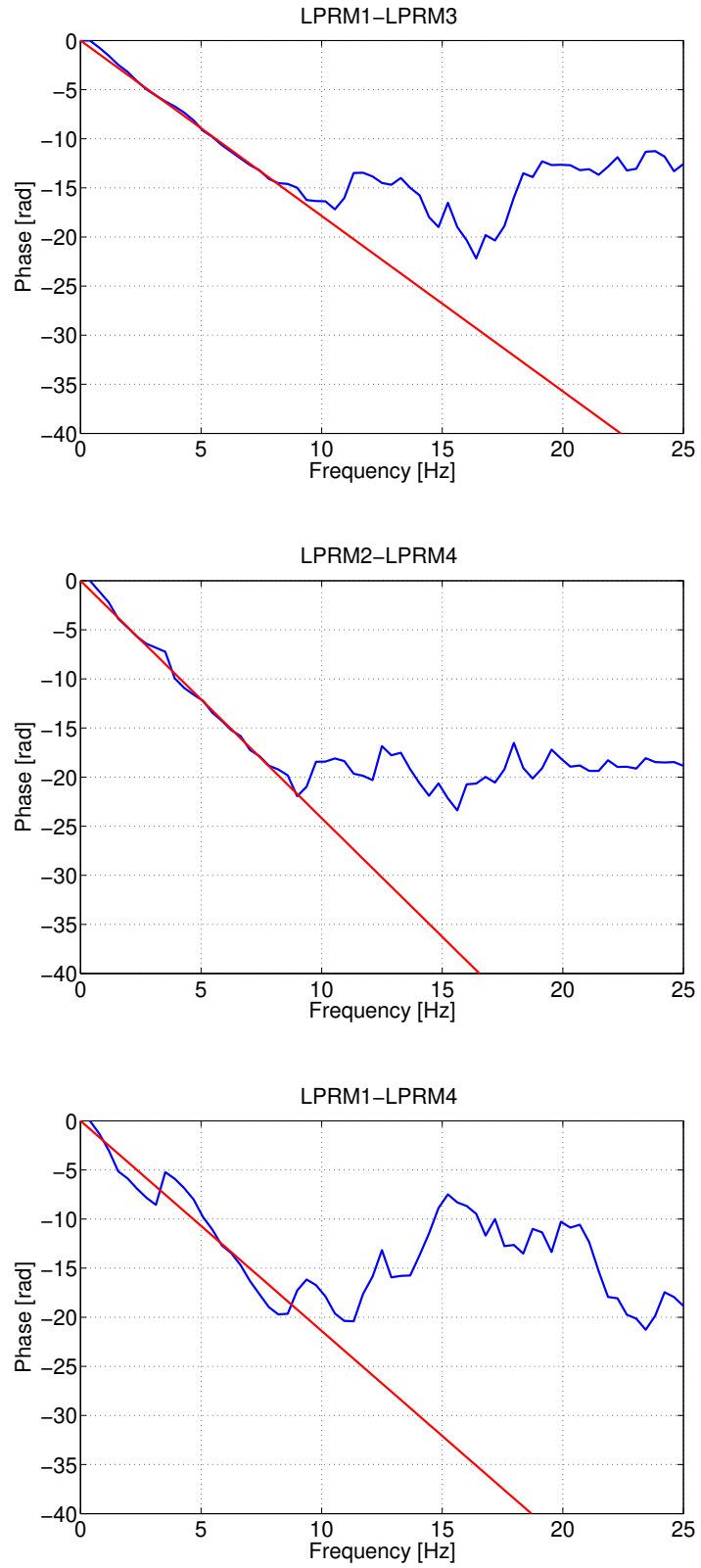


Figure 5.5: Phase of the CPSD for the detector pairs LPRM1-LPRM3 (top), LPRM2-LPRM4 (middle) and LPRM1-LPRM4 (bottom).

Fig. 5.4 shows the phases between the adjacent detectors 1-2, 2-3 and 3-4. Basically, these are the same as the ones found in the literature, except for the use of different block size in the data processing, and a different style of plotting (in contrast to the usual presentation in the literature, we are not restricting the plot range to between  $\pm\pi$ ). This is because showing the plots without the restriction (“folding back” the phase when it reaches  $-\pi$  to  $+\pi$ ) indicates qualitatively the goodness of the fit much better.

It is seen that the phase between the adjacent pairs of detectors shows a clear linear behaviour up to 15 Hz. One can also see the decreasing of the slope, and hence the transit time, from the bottom to the top, corresponding to the increasing steam velocity upwards in the core, which is consistent with the expectations.

The phases of the non-adjacent detector pairs 1-3, 2-4 and 1-4 are shown in Fig. 5.5. It is seen that the frequency range of the linear part of the slope has decreased significantly, below 10 Hz. The goodness of the fit for the phase of the pairs 1-3 and 2-4 is still good, but for the pair 1-4, i.e. for the top and bottom detector, lying from each other at the largest distance, it is seemingly not satisfactory. This is underlined by the fact that the coherence between detectors 1 and 4 (not shown here) is much lower than for the adjacent detector pairs, but also lower than for the other two pairs in the same figure. The poor fit is also easily seen visually from the fact that because of the positions of the detectors, in this figure too, the top figure should display the shallowest slope, and the bottom figure should show a much larger slope than any of the two other. But the figure shows that this is not the case. On the other hand it is also seen that the curve fitting is very poor for the pair 1-4, and the result depends relatively heavily on what frequency region of the phase the linear fitting is made. Choosing a shorter frequency range for the fitting would have resulted in a higher slope. All in all, there is quite some arbitrariness, and hence increased uncertainty, in the determination of the transit time between the far-away detectors 1 and 4.

For presenting the quantitative results for the transit times, in the notations we will revert to the convention used in the previous report, in that the numbering starts from the bottom of the core and increases upwards. Since in the last report, only the transit times between the adjacent detectors were considered, it sufficed to use single indices, such that  $\tau_1$  stood for the transit time of the lowermost two detectors,  $\tau_2$  for the transit time between the two middle detectors etc. Since we now consider transit times also between the non-adjacent detectors, double indices will be necessary. With the notations of numbering from the bottom,  $\tau_{1,2}$  will stand for the transit time between the lowermost and next lowermost detector,  $\tau_{2,3}$  for the transit time between the second detector from the bottom to the third from the bottom,  $\tau_{1,3}$  for the transit time between the lowermost detector to the third from the bottom (second from the top) etc. The corresponding transit times are shown in Table 5.1.

In possession of these transit times, the consistence check yields the following

Table 5.1: **Transit times (in seconds) between the various combinations of detector pairs.**

$\tau_{1,2}$	$\tau_{2,3}$	$\tau_{3,4}$	$\tau_{1,3}$	$\tau_{2,4}$	$\tau_{1,4}$
0.2269	0.1687	0.1197	0.3848	0.2842	0.346

results:

$$\tau_{1,2} + \tau_{2,3} = 0.396; \quad \tau_{1,3} = 0.385; \quad (5.8)$$

$$\tau_{2,3} + \tau_{3,4} = 0.288; \quad \tau_{2,4} = 0.284; \quad (5.9)$$

$$\tau_{1,2} + \tau_{2,3} + \tau_{3,4} = 0.515; \quad \tau_{1,4} = 0.346 \quad (5.10)$$

As Eqs. (5.8) and (5.9) show, the additivity of the transit times is well fulfilled for the lower three and the upper three detectors. However, as it is seen from (5.10), the additivity of all three transit times between the three adjacent detector pairs does not add up to the measured transit time between the first and the fourth detector. As discussed earlier, the reason for this is the poor coherence between the signal of detectors 1 and 4. This is due to both of a substantial amount of new steam being generated above the lowermost detector, which only affects the uppermost detector, as well as a large change in the two phase flow regime.

One can also note that the phase between detector 1 and 4 shows an increased influence of the global (reactivity) component as compared to the local component. As was already noticed in the first publications on the existence of the local component of the neutron noise in BWRs [51, 40], a pure local component, mediated by the transport of the two-phase flow, leads to a linear dependence of the phase on frequency. Without propagation, a global (reactivity) effect yields zero phase between axially placed detectors. A joint presence of the global and the local component, when none of them dominates, leads to an oscillation of the phase around the linear shape. This is clearly seen on the bottom plot of Fig. 5.5. In the correlation between detector 1 and 4, the weight of the local component has decreased as compared to the global component, due to the few bubbles or other local two-phase flow fluctuations affecting both detectors. This leads to the oscillation of the phase, which contributes to the poor estimation of the transit time between the two detectors lying farthest away from each other.

### 5.3.3 Uncertainty investigation

The reviewers also suggested a thorough uncertainty and sensitivity analysis of both the transit time determination from the in-core noise measurements, as well as the unfolding method. Such an ambitious study lay also outside the objectives of the paper, but a limited study of the uncertainty of the transit time determination was possible to perform. Namely, from previous measurements, we had the possibility to determine the transit times from four measurements in identical operation conditions, and hence to investigate the standard deviation in the transit times for these four cases.

The data used for this analysis were taken from measurements made in Ringhals-1 [22]. These measurements were originally not made with the purpose of performing an uncertainty analysis. Rather, they were part of an effort in which we tried to generate a fourth transit time, by also using a TIP detector in parallel with the four standard in-core LPRMs. In this particular measurement campaign, four identical measurements were taken, while a TIP detector was placed at the four LPRM positions, respectively. Since the position of the TIP does not influence the thermal hydraulic conditions, this meant that each of the three transit times between the four LPRMs were measured four times under identical conditions. The results of these four measurements can therefore be used for a rough estimate of the uncertainty of the transit time estimation.

The three transit times  $\tau_1 - \tau_3$  for the four measurements, together with the mean values and the relative standard deviations are given below in Table 5.2. It is seen that the uncertainty of the transit time estimation is about 1%.

Table 5.2: **Transit times from Ringhals-1 (from [22]). All times are in seconds**

Measurement number	$\tau_1$	$\tau_2$	$\tau_3$
1	0.2712	0.2111	0.1253
2	0.2684	0.2089	0.1272
3	0.2740	0.2114	0.1289
4	0.2765	0.2051	0.1291
Mean	0.2725	0.2091	0.1276
Relative standard deviation	0.0128	0.0139	0.0138

The result is rather satisfactory, but it has to be added that it is based only one singular case, consisting of only four measurements in identical operating positions. To have a more reliable estimate of the uncertainty of the determination of the transit time and that of the velocity reconstruction method, more investigations and more measurement data are necessary.

#### 5.3.4 Test with velocity profiles obtained from RAMONA

One comment of the reviewers concerned the case of BWRs with partial length fuel rods. As Fig. 5.2 shows, displaying the calculated velocity profiles in the neighbouring channels 340, 341, 344 and 345, the presence of such rods leads to a discontinuous change of the velocity in all channels, which cannot be reproduced by smooth polynomials. The claim was that for such cases the determination of the local velocities, and hence the determination of the local void fraction, is not possible with the method suggested by us.

At the same time one can note that the velocity profile is not the primary goal of the method; it is only a tool in order to determine the values of the void velocity at the four fixed detector positions. Hence, whereas reconstructing the velocity profile in its whole is obviously not possible, this does not exclude the possibility that the velocities at the individual detector positions, or at least a majority of them, can be determined. Therefore, we decided to test the performance of the unfolding

procedure by using the velocity profiles generated by the RAMONA calculations, shown in Fig. 5.2. One advantage of this exercise was that these profiles can be considered as rather realistic, and characteristic for modern operating BWRs.

For the test, first the transit times between the detector positions had to be determined. Since the RAMONA calculations give the velocity in a number of discrete points (26 positions), for the accurate determination of the transit time, first a piece-wise continuous function was fitted to the calculated profiles. From the core inlet up to the lower end of the discontinuity, as well as from the top end of the discontinuity to the core outlet, a polynomial fit was made. The discontinuity, which occurs between two adjacent RAMONA points, was represented by a linear fit. The result of this fitting is shown in Fig. 5.6.

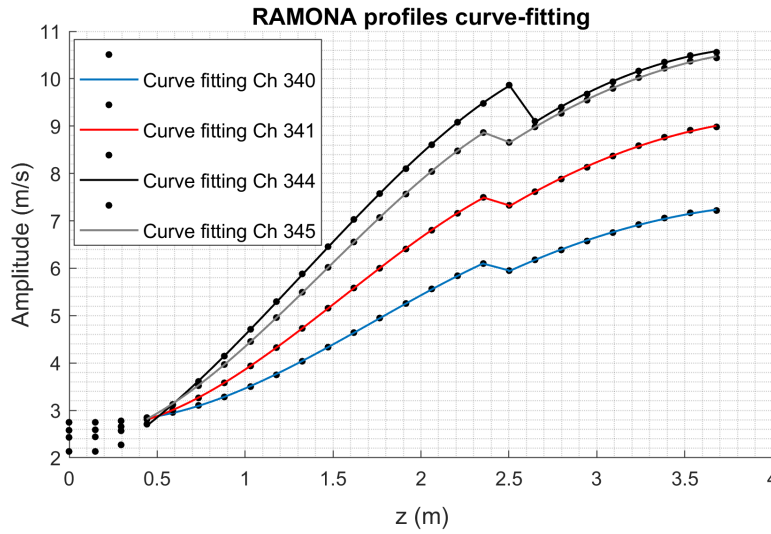


Figure 5.6: Fitting a piecewise continuous function to the discrete velocity points provided by RAMONA calculations. Dots: values given by RAMONA. Continuous lines: results of the fitting.

Thereafter, the transit times were calculated by an integration of the inverse velocity from the fitted curves, and then they were used in the unfolding procedure, described in Section 5.2.3. Due to its larger flexibility, a polynomial fit was used for the unfolding. The onset point of the boiling, and the steam velocity at this, was taken from the RAMONA data. The results of the reconstructed profiles are shown in Fig. 5.7, and the reconstructed velocities at the detector positions are listed in Table 5.3.

Fig. 5.7 shows that, for obvious reasons, the reconstructed profiles cannot display any discontinuity. However, they reconstruct the RAMONA velocity profiles quite accurately up to the discontinuity, after which there is a significant deviation between the true and the reconstructed values. The reconstructed velocity in this section, i.e. in the uppermost part of the core, overestimates the true velocity. Accordingly, the steam velocity values are reproduced quite accurately in the lower three detectors, whereas there is an error between 5 - 10 % in the uppermost detector (Table 5.3). Regarding this latter detector, one has to add that it is quite close to

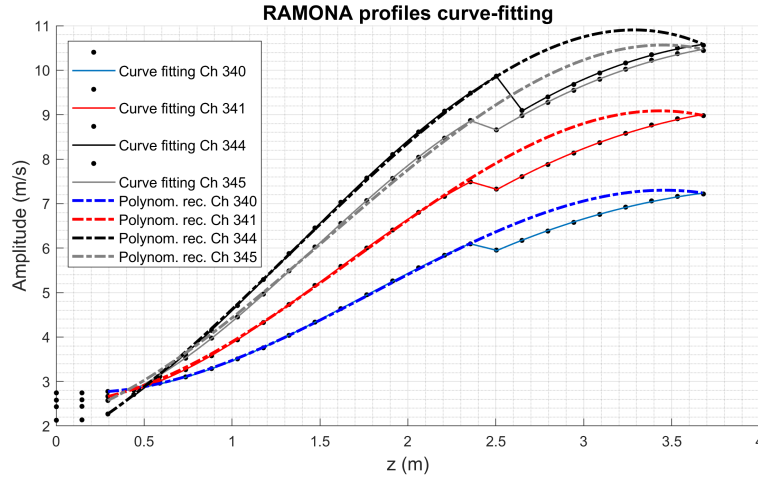


Figure 5.7: Results of the reconstruction of the velocity profiles of RAMONA from the transit times given by the RAMONA profiles.

Table 5.3: **True and reconstructed steam velocities at the detector positions from the RAMONA calculations. Velocities are in  $[m/s]$**

Channel	$v_1$	$v_2$	$v_3$	$v_4$
340 true	3.0130	4.3102	5.9338	6.7269
340 reconstructed	3.0259	4.3000	5.9255	7.1153
341 true	3.1292	5.1182	7.2838	8.3300
341 reconstructed	3.1751	5.1000	7.3264	8.8727
344 true	3.3651	6.3977	9.2320	9.8958
344 reconstructed	3.4050	6.3800	9.1922	10.8081
345 true	3.3249	5.9716	8.6179	9.7551
345 reconstructed	3.4335	5.9500	8.5606	10.3114]

the discontinuity, which means an abrupt change in the velocities of all phases (fluid and steam). In such a case the concept of “local velocity” and “local void fraction” becomes problematic, so reproducing the local void fraction in that position is not a prime priority.

In view of the above, it is quite encouraging that despite the discontinuous character of the velocity profile, the true velocity values were correctly reproduced at 3 of the 4 detectors, and with an overestimation of the true velocity by only 5 - 10% in the uppermost detector. It can be added that, as is seen in Eq. (5.1), an overestimation of the velocity leads to an underestimation of the detector field of view  $\lambda$ . Due to the inverse relationship between the field of view and the void fraction, this also means an overestimation of the void content. This way, one can claim that in cores containing partial length fuel with characteristic length up to the uppermost detector, the reconstruction procedure yields a correct value for three lower detectors, and supplies an upper limit on the void fraction at the position of the uppermost detector.

## 5.4 Conclusions

Addressing the questions raised by the reviewers concerning various aspects of the method led to a better understanding of the associated problems, but also, through the additional investigations, it increased our confidence in the applicability and a better estimate of the expected performance of the method. Naturally, further work is required in several areas, and there is a need for a wider verification of the method, which in turn requires access to realistic void velocity profiles and further in-core noise measurements. The efforts will be continued to obtain such data either from Swedish power plants, or from abroad. Also, to reach the final goal of the project, i.e. to determine the void fraction from the in-core neutron noise measurements, the calculation of the detector field-of-view (the range of the local component) should be achieved for realistic cases.

## 6. PROPOSAL FOR 2021-22

1. Analysis of vibrations of thimble tubes with axially dependent in-core measurements in various radial positions.
2. Evaluation of new ex-core measurements for beam, reactivity, shell and tilting mode vibrations in R3 or R4.
3. Preliminary evaluation of the feasibility of a conceptual design, through simulations and pilot measurements, of a fibre-based detector for the measurement of the gradient of the neutron flux.
4. Investigation of the possibility of detecting subcooled boiling in the upper part of a PWR through evaluation of in-core measurements made by movable detectors.



## **7. ACKNOWLEDGEMENT**

This one-year contract was performed by funding from Ringhals Vattenfall AB, contract No. 4501737229-003. Contact person from Ringhals was Dr. Henrik Nylén.

## REFERENCES

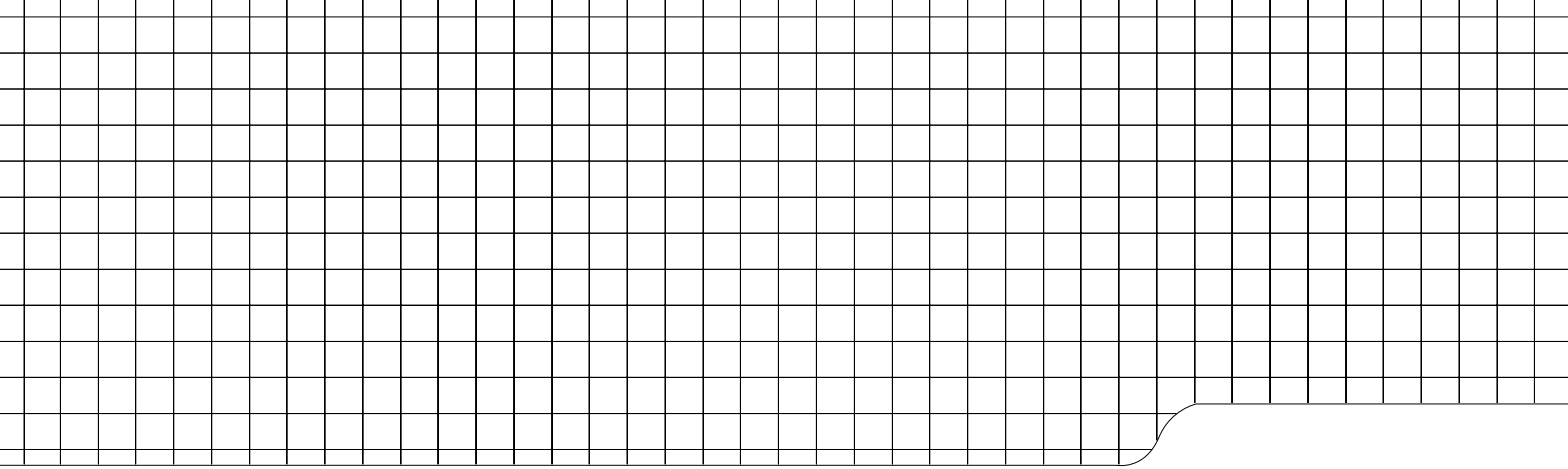
- [1] J. Guitton and C. Puyal, “New trends in vibration and acoustic monitoring in nuclear components in EDF,” *Progress in Nuclear Energy*, vol. 21, pp. 807–811, 1988.
- [2] B. Michel and C. Puyal, “Operational and economical experience with vibration and loose parts monitoring systems on primary circuits of PWRs,” *Progress in Nuclear Energy*, vol. 21, pp. 469–473, 1988.
- [3] A. Trenty, C. Puyal, C. Vincent, M. H. Inchauspe, R. Baeyens, C. Messainguiral-Bruynooghe, and G. Lagarde, “Thimble vibration analysis and monitoring on 1300 and 900 MW reactors using accelerometers and in-core neutron noise (in French),” *Progress in Nuclear Energy*, vol. 21, pp. 97–106, 1988.
- [4] I. Pázsit, L. A. Torres, C. Montalvo, Y. Kitamura, L. Nagy, and H. Nylén, “*Ringhals Diagnostics and Monitoring, Annual Research Report 2018-19*,” CTH-NT-339/RR-22, Chalmers University of Technology, Göteborg, Sweden, June 2019.
- [5] I. Pázsit and O. Glöckler, “BWR Instrument Tube Vibrations - Interpretation of Measurements and Simulation,” *Annals of Nuclear Energy*, vol. 21, no. 12, pp. 759–786, 1994.
- [6] C. Demazière, C. Sunde, V. Arzhanov, and I. Pázsit, “*Final Report on the Research Project Ringhals Diagnostics and Monitoring, Stage 8*,” CTH-RF-177/RR-10, Chalmers University of Technology, Göteborg, Sweden, December 2003.
- [7] C. Demazière, C. Sunde, and I. Pázsit, “*Final Report on the Research Project Ringhals Diagnostics and Monitoring, Stage 9*,” CTH-RF-187/RR-11, Chalmers University of Technology, Göteborg, Sweden, January 2005.
- [8] C. Sunde, J. Wright, C. Demazière, and I. Pázsit, “*Final Report on the Research Project Ringhals Diagnostics and Monitoring, Stage 10*,” CTH-RF-194/RR-12, Chalmers University of Technology, Göteborg, Sweden, November 2005.
- [9] C. Sunde, C. Demazière, and I. Pázsit, “*Final Report on the Research Project Ringhals Diagnostics and Monitoring, Stage 11*,” CTH-NT-206/RR-13, Chalmers University of Technology, Göteborg, Sweden, February 2007.
- [10] I. Pázsit, C. Demazière, C. Sunde, P. Bernitt, and A. Hernández-Solís, “*Final Report on the Research Project Ringhals Diagnostics and Monitoring, Stage 12*,” CTH-NT-220/RR-14, Chalmers University of Technology, Göteborg, Sweden, August 2008.

- [11] I. Pázsit and V. Dykin, “Investigation of the space-dependent noise induced by propagating perturbations,” *Annals of Nuclear Energy*, vol. 37, no. 10, pp. 1329–1340, 2010.
- [12] C. Demazière, V. Arzhanov, J. K.-H. Karlsson, and I. Pázsit, “*Final Report on the Research Project Ringhals Diagnostics and Monitoring, Stage 4*,” CTH-RF-145/RR-6, Chalmers University of Technology, Göteborg, Sweden, September 1999.
- [13] I. Pázsit, C. Montalvo Martín, V. Dykin, and T. Tambouratzis, “*Final Report on the Research Project Ringhals Diagnostics and Monitoring, Stage 13*,” CTH-NT-230/RR-15, Chalmers University of Technology, Göteborg, Sweden, March 2010.
- [14] A. Rácz and I. Pázsit, “Diagnostics of detector tube impacting with wavelet techniques,” *Annals of Nuclear Energy*, vol. 25, no. 6, pp. 387–400, 1998.
- [15] V. Arzhanov and I. Pázsit, *Detecting Impacting of BWR Instrument Tubes by Wavelet Analysis*, pp. 157–174. Springer Berlin Heidelberg, 2002.
- [16] C. Sunde and I. Pázsit, “Investigation of detector tube impacting in the Ringhals-1 BWR,” *International Journal of Nuclear Energy Science and Technology*, vol. 2, no. 3, pp. 189–208, 2006.
- [17] I. Pázsit (Ed.), “*Final Report on the Research Project Ringhals Diagnostics and Monitoring, Stage 1*,” CTH-RF-122/RR-3, Chalmers University of Technology, Göteborg, Sweden, September 1996.
- [18] I. Pázsit, J. Karlsson, and N. Garis, “*Final Report on the Research Project Ringhals Diagnostics and Monitoring, Stage 2*,” CTH-RF-132/RR-4, Chalmers University of Technology, Göteborg, Sweden, October 1997.
- [19] J. K.-H. Karlsson and I. Pázsit, “*Final Report on the Research Project Ringhals Diagnostics and Monitoring, Stage 3: Analysis of core barrel vibrations in Ringhals 2, 3 and 4 for several fuel cycles*,” CTH-RF-135/RR-5, Chalmers University of Technology, Göteborg, Sweden, October 1998.
- [20] M. Pázsit and I. Pázsit, “*Final Report on the Analysis of Core Barrel Vibrations in Ringhals PWRs R2, R3 and R4 from Measurements Made in 2005*,” Internal report, Chalmers University of Technology, Göteborg, Sweden, 2006.
- [21] I. Pázsit, C. Montalvo Martín, V. Dykin, and H. Nylén, “*Final Report on the Research Project Ringhals Diagnostics and Monitoring, Stage 14*,” CTH-NT-253/RR-16, Chalmers University of Technology, Göteborg, Sweden, December 2011.
- [22] V. Dykin, C. Montalvo Martín, H. Nylén, and I. Pázsit, “*Ringhals Diagnostics and Monitoring, Final Research Report 2012 - 2014*,” CTH-NT-304/RR-19, Chalmers University of Technology, Göteborg, Sweden, December 2014.

- [23] V. Dykin, C. Montalvo, N. Tran, H. Nylén, and I. Pázsit, “*Ringhals Diagnostics and Monitoring, Annual Research Report 2015*,” CTH-NT-319/RR-20, Chalmers University of Technology, Göteborg, Sweden, December 2015.
- [24] I. Pázsit, C. Montalvo, N. Tran, H. Nylén, and O. Olvera Guerrero, “*Ringhals Diagnostics and Monitoring, Annual Research Report 2016-17*,” CTH-NT-333/RR-21, Chalmers University of Technology, Göteborg, Sweden, December 2017.
- [25] I. Pázsit, L. A. Torres, C. Montalvo, L. Nagy, M. Szieberth, G. Klujber, T. Misawa, Y. Kitamura, and H. Nylén, “*Ringhals Diagnostics and Monitoring, Annual Research Report 2019-20*,” CTH-NT-342/RR-23, Chalmers University of Technology, Göteborg, Sweden, June 2020.
- [26] M. Nilsson, “*Brusmätning för att söka lågfrekventa störningar i R3, Annual Research Report 2015*,” Ringhals internal report UH-rapport 2099930 / 2.0, Ringhals AB, Göteborg, Sweden, October 2010.
- [27] B. Severinsson, “*“Brusmätningar för analys av hårdhöljesvibrationer på Ringhals 3. Utförda mellan 2013-02-26 och 2013-07-05*,” Ringhals internal report UH-rapport 2245846 / 2.0, Ringhals AB, Göteborg, Sweden, July 2013.
- [28] B. Severinsson, “*Brusmätning för analys av Hårdhöljesvibrationer på utförda under 2013*,” Ringhals internal report UH-rapport 2233461 / 2.0, Ringhals AB, Göteborg, Sweden, July 2013.
- [29] L. Pál, I. Pázsit, and Zs. Elter, “Comments on the stochastic characteristics of fission chamber signals,” *Nuclear Instruments and Methods in Physics Research Section A: Accelerators, Spectrometers, Detectors and Associated Equipment*, vol. 763, no. 0, pp. 44–52, 2014.
- [30] I. Pázsit and L. Pál, *Neutron Fluctuations: a Treatise on the Physics of Branching Processes*. New York: Elsevier, 2008.
- [31] L. Pál and I. Pázsit, “Campbell-type theory of fission chamber signals generated by neutron chains in a multiplying medium,” *Nuclear Instruments and Methods in Physics Research Section A: Accelerators, Spectrometers, Detectors and Associated Equipment*, vol. **794**, no. 1, pp. 90–101, 2015.
- [32] Y. Kitamura, I. Pázsit, and T. Misawa, “Determination of prompt neutron decay constant by time-domain fluctuation analyses of detector current signals,” *Annals of Nuclear Energy*, vol. 120, pp. 691–706, 2018.
- [33] B. Diven, H. Martin, R. Taschek, and J. Terrell, “Multiplicities of fission neutrons,” *Physical Review*, vol. 101, no. 3, p. 1012, 1956.
- [34] P. Cheol Ho ed., “Experimental Benchmarks for Accelerator-Driven System (ADS) at Kyoto University Critical Assembly,” Technical report, Research Reactor Institute, Kyoto University, 2012. KURRI-TR-444.

- [35] G. Klujber, I. Barth, and M. Szieberth, “Construction of a measurement system for the data acquisition of fission chambers in the current mode. In Hungarian (*Mérőrendszer kiépítése hasadási kamrák árammódú adatfelvételéhez*),” Technical report, Budapest University of Technology and Economics, Institute of Nuclear Techniques, 2019. BME-NTI-887/2019.
- [36] StemLabs, *Red Pitaya STEMLab Board Specifications*, 2018. <https://www.redpitaya.com/f130/red-pitaya-stemlab-board/>.
- [37] Red Pitaya StemLab, *Red Pitaya Documentation*, 2017. Revision b1890399; <https://redpitaya.readthedocs.io/en/latest/>.
- [38] G. Klujber and M. Szieberth, “Development of FPGA based time-stamp mode data acquisition system,” Technical report, Budapest University of Technology and Economics, Institute of Nuclear Techniques, 2017. BME-NTI-821/2017.
- [39] G. Kosály, L. Maróti, and L. Meskó, “A simple space dependent theory of the neutron noise in a boiling water reactor,” *Annals of Nuclear Energy*, vol. 2, no. 2, pp. 315–321, 1975.
- [40] G. Kosály, “Noise investigations in boiling-water and pressurized-water reactors,” *Prog. nucl. Energy*, vol. 5, pp. 145–199, 1980.
- [41] I. Pázsit, L. A. Torres, M. Hursin, H. Nylén, V. Dykin, and C. Montalvo, “Development of a new method to determine the axial void velocity profile in BWRs from measurements of the in-core neutron noise,” *Progress in Nuclear Energy*, vol. 138, p. 103805, 2021.
- [42] B. G. Bergdahl, “Brusdata-bibliotek - Data från mätningar och experiment under åren 1985-1995 konverterade från band till CD,” SSM report, GSE Power Systems AB, 2002. SKI Rapport 02:6.
- [43] USNRC, “TRACE V5.0 Theory Manual, Field Equations, Solution Methods and Physical Models,” Draft Report, Office of Nuclear Regulatory Research, U.S. Nuclear Regulatory Commission, Washington, DC. Available on NRC’s online document retrieval system ADAMS since February. 2009 with Reference No. “ML071000097”.8, 2008.
- [44] USNRC, “TRACE V5.0 Users Guide – Volume 1: Input Specification,” Draft Report Available on NRC’s online document retrieval system ADAMS since March 2009 with Reference No. “ML071000103”, 2008.
- [45] USNRC, “TRACE V5.0 Users Guide – Volume 2: Modeling Guidelines,” Draft Report, Office of Nuclear Regulatory Research, U.S. Nuclear Regulatory Commission, Washington, DC. Available on NRC’s online document retrieval system ADAMS since March 2009 with Reference No. “ML071720510”.., 2008.
- [46] W. Wulff, “A Description and Assessment of RAMONA-3B Mod. 0 Cycle 4: A Computer Code with Three - Dimensional Neutron Kinetics for BWR System Transients,” NUREG Report, BNL-NUREG 51748, 1984.

- [47] RAMONA, “RAMONA-5, User Manual,” tech. rep., Studsvik Scandpower AS, 2001.
- [48] “Wolfram Research, Inc., Mathematica, Version 12.0.0.0.” Champaign, IL., 2019.
- [49] T. Yamamoto, “Implementation of a frequency-domain neutron noise analysis method in a production-level continuous energy Monte Carlo code: Verification and application in a BWR,” *Annals of Nuclear Energy*, vol. 115, pp. 494–501, 2018.
- [50] I. Pázsit and C. Demazière, *Noise Techniques in Nuclear Systems*, vol. 2 of *Handbook of Nuclear Engineering*, pp. 1631 – 1737. Springer Science, 2010.
- [51] D. Wach and G. Kosály, “Investigation of the joint effect of local and global driving sources in incore-neutron noise measurements,” *Atomkernenergie*, vol. 23, pp. 244–250, 1974.



CHALMERS UNIVERSITY OF TECHNOLOGY  
SE 412 96 Gothenburg, Sweden  
Phone: + 46 - (0)31 772 10 00  
Web: [www.chalmers.se](http://www.chalmers.se)